PhotoniX

REVIEW Open Access

# MXene sensors based on optical and electrical sensing signals: from biological, chemical, and physical sensing to emerging intelligent and bionic devices

Leiming Wu[1,2*], Xixi Yuan[3], Yuxuan Tang[4], S. Wageh[5], Omar A. Al-Hartomy[5], Abdullah G. Al-Sehemi[6], Jun Yang[1*], Yuanjiang Xiang[7*], Han Zhang[4*] and Yuwen Qin[1,2*]

*Correspondence: leiming_wu@gdut.edu.cn; yangj@gdut.edu.cn; xiangyuanjiang@126.com; hzhang@szu.edu.cn; qinyw@gdut.edu.cn

[1] Guangdong Provincial Key Laboratory of Information Photonics Technology, School of Information Engineering, Guangdong University of Technology, Guangzhou 510006, China
[4] Guangdong Laboratory of Artificial Intelligence and Digital Economy (SZ), College of Physics and Optoelectronic Engineering, Shenzhen Key Laboratory of Micro-Nano Photonic Information Technology, Shenzhen University, Shenzhen 518060, China
[7] School of Physics and Electronics, Hunan University, Changsha 410082, China
Full list of author information is available at the end of the article

## Abstract

Sensing devices are key nodes for information detection, processing, and conversion and are widely applied in different fields such as industrial production, environmental monitoring, and defense. However, increasing demand of these devices has complicated the application scenarios and diversified the detection targets thereby promoting the continuous development of sensing materials and detection methods. In recent years, $Ti_{n+1}C_nT_x$ ($n = 1, 2, 3$) MXenes with outstanding optical, electrical, thermal, and mechanical properties have been developed as ideal candidates of sensing materials to apply in physical, chemical, and biological sensing fields. In this review, depending on optical and electrical sensing signals, we systematically summarize the application of $Ti_{n+1}C_nT_x$ in nine categories of sensors such as strain, gas, and fluorescence sensors. The excellent sensing properties of $Ti_{n+1}C_nT_x$ allow its further development in emerging intelligent and bionic devices, including smart flexible devices, bionic E-skin, neural network coding and learning, bionic soft robot, as well as intelligent artificial eardrum, which are all discussed briefly in this review. Finally, we present a positive outlook on the potential future challenges and perspectives of MXene-based sensors. MXenes have shown a vigorous development momentum in sensing applications and can drive the development of an increasing number of new technologies.

**Keywords:** $Ti_{n+1}C_nT_x$ ($n = 1, 2, 3$) MXenes, Sensing applications, Intelligent devices

## Introduction

In the information age, sensing is a key technology for information collection, detection, and analysis that is widely used in defense [1], disaster relief [2], medical diagnosis [3], environmental monitoring [4], ocean exploration [5], industrial production [6], food safety [7], and so on. Conventional sensors can be used to detect certain biological interactions, chemical reactions, or physical variables. These sensors can detect changes in the detection target and convert them into electrical, optical, thermal, or other easily detected signals for transmission, processing, and storage. An ideal sensor should

have the following characteristics: high sensitivity, outstanding selectivity, low detection limit, good stability/durability, and fast response time. However, the complexity of the detection environment, the diversity of detection targets, and the requirements for high sensitivity, fast response, and durability have promoted the renewal and development of sensing materials.

In recent years, $Ti_{n+1}C_nT_x$ ($n = 1, 2, 3$) MXenes have been developed as one of the most ideal candidates for sensing owing to their large specific surface areas, excellent mechanical stability, outstanding electrical conductivity, and good hydrophilicity [8, 9]. MXenes have an octahedral structure composing an ordered combination of transition metal atoms and C/N atoms, where the C/N atoms are located at the center of the octahedron formed by the transition metal atoms [10]. $Ti_3C_2T_x$, one of the most representative MXenes, comprises two layers of carbon atoms sandwiched between three layers of titanium atoms, forming a sandwich structure [11–13]. Compared with other two-dimensional (2D) materials, MXenes offer the following advantages in sensing applications: 1) the large specific surface area [8, 14] can provide adequate surface area for loading the target. Moreover, etched MXene materials exhibit an accordion-like structure, and intercalation with urea, hydrazine hydrate, or metal ion salts can further expand the interlayer spacing and increase the space for biological and chemical reactions [15]. 2) The abundant surface functional groups endow MXenes with good hydrophilicity, enabling achievement of selective detection of specific targets through modification [16]. 3) $Ti_3C_2T_x$ has metal-like properties with electrical conductivity as high as 4600 S $cm^{-1}$ [17]. 4) MXenes have stable structures, and modified MXenes have strong oxidation resistance; they can withstand various conditions, such as strong acidity, strong alkalinity, high humidity, high salinity, and high temperatures [18, 19].

There are numerous MXene-based sensors, which can be divided into two types, optical and electrical, depending on the sensing signal. In this review, we present and discuss the synthesis routes, important properties, sensing applications, and prospects of $Ti_{n+1}C_nT_x$ ($n = 1, 2, 3$) MXenes. $Ti_3C_2T_x$ is the earliest MXene material discovered and successfully fabricated, which represents the rise of MXenes. Among all MXene materials, $Ti_3C_2T_x$ is the most extensively studied, including preparation methods, physical properties, application fields, etc. Therefore, this review only summarizes the sensing applications of $Ti_3C_2T_x$ MXene and its allotrope $Ti_2CT_x$.

First, several mainstream approaches for synthesizing $Ti_{n+1}C_nT_x$ ($n = 1, 2, 3$) MXenes are discussed [13, 20], such as hydrofluoric acid (HF) etching, LiF-HCl etching, and alkaline etching. Second, we discuss the excellent physical, chemical, and biological properties of MXenes, such as good chemical stability, outstanding electrical conductivity, and abundant surface functions. Third, nine types of optical and electrical sensors, based on $Ti_{n+1}C_nT_x$ ($n = 1, 2, 3$) nanosheets (NSs) and quantum dots (QDs), in the fields of biology, chemistry, and physics are presented (Fig. 1) [11, 21–26], namely surface plasmon resonance (SPR), gas, fluorescence, surface-enhanced Raman scattering (SERS), colorimetric, electrochemical, temperature, humidity, and pressure/strain sensors. Among these MXene-based sensors, SPR, colorimetric, SERS, and fluorescence sensors use optical signals as detection methods; thus, they are classified as optical sensing technologies. Gas, pressure/strain, temperature, humidity, and electrochemical sensors use electrical analysis signals, and hence, they are classified as electrical sensing technologies. In

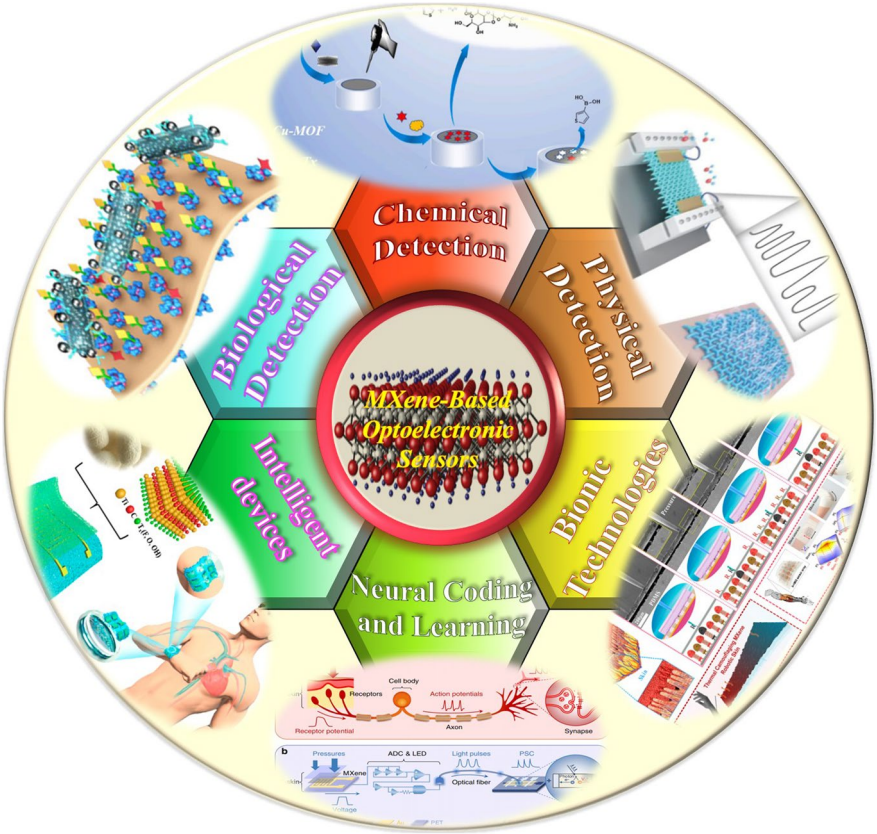


**Fig. 1** Schematic diagram of MXene sensing application areas: from biological, chemical, and physical detection to intelligent and bionic devices [11, 21–26]. Copyright 2021, American Chemical Society. Copyright 2020, American Chemical Society. Copyright 2016, Wiley–VCH. Copyright 2019, Wiley–VCH. Copyright 2020, Springer Nature. Copyright 2022, Elsevier. Copyright 2019, Elsevier

addition to their applications in conventional fields, MXene-based sensors can also be used in frontier technological fields, such as intelligent sensing, bionic robots, neural network coding, and intelligent artificial eardrum. The discussion presented in this section is a gist of this review, and it is discussed in detail in the subsequent sections. Lastly, this review proposes some potential future applications of MXenes and their modifications such as human–machine interfaces, smart sensing, and sensing applications of high-entropy MXenes. All in all, MXene is currently a new type of sensing material that has attracted extensive attention due to its excellent physical and chemical properties. Here, we provide a comprehensive review of MXene sensors based on optical and electrical principles, and believe that this review can provide guidance for the development of MXene materials in the field of sensing technology.

## Fabrication and characterization of 2D $Ti_{n+1}C_nT_x$

MXene, an emerging type of 2D material, is fabricated using the $M_{n+1}AX_n$ ($n = 1, 2, 3$) phase as a precursor to selectively remove 'A' by etching while retaining the 'M' and 'X' layers (Fig. 2). Typically, 'A' is an element of group IIIA or IVA, which is mainly Al or Si. 'M' is usually a transition metal element, and 'X' is C or N. The MXene NSs obtained after MAX phase etching exhibit a large number of surface functional groups (–O, –OH,

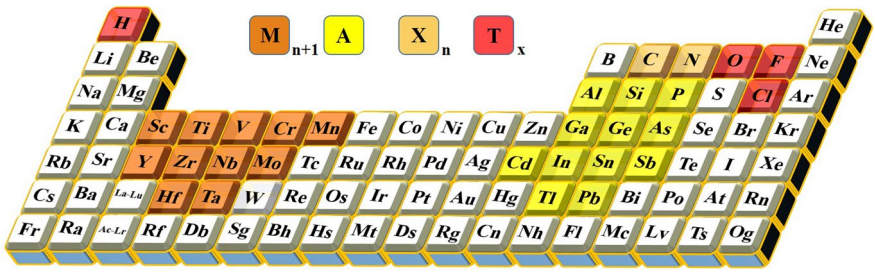


**Fig. 2** The chemical elements contained in the $M_{n+1}AX_n$ ($n = 1, 2, 3$) phases [30]

and –F), which are represented by $T_x$. $Ti_3C_2T_x$ is the most representative candidate among MXenes, it was successfully fabricated using chemical etching in 2011 [13]. They extracted Al from the MAX phase of $Ti_3AlC_2$ and achieved 2D $Ti_3C_2T_x$ layers. In etching, approximately 10 g of $Ti_3AlC_2$ powder is added to a 50% concentrated HF solution (100 mL), followed by etching at room temperature for 2 h. The resulting suspension was washed and centrifuged several times with deionized water. The fabrication process of 2D $Ti_3C_2T_x$ is presented in Fig. 3(a) [27]. After the $Ti_3AlC_2$ powders were etched, exfoliated $Ti_3C_2T_x$ flakes were obtained through sonication. Figure 3(b) shows the SEM image of $Ti_3AlC_2$ powders before HF etching, which is the typical MAX phase [28]. After HF etching, the morphology of the as-prepared $Ti_3C_2T_x$ with Al removed is shown in Fig. 3(c) [28], which indicates an accordion-like structure of $Ti_3C_2T_x$. After sonication, the $Ti_3C_2T_x$ flakes fall off from the accordion-like structure, forming an independent 2D atomic layer (Fig. 3(d) and (e)) [29]. The etching of $Ti_{n+1}AlC_n$ by the HF solution is represented using the following chemical reactions [28]:

$$Ti_{n+1}A1C_n + 3HF = A1F_3 + 1.5H_2Ti_{n+1}C_n \tag{1}$$

$$Ti_{n+1}C_n + 2H_2O = Ti_{n+1}C_n(OH)_2 + H_2 \tag{2}$$

$$Ti_{n+1}C_n + 2HF = Ti_{n+1}C_nF_2 + H_2 \tag{3}$$

The 2D $Ti_{n+1}C_nT_x$ ($n = 1, 2, 3$) obtained by HF etching had surface groups (–O, –OH, and –F) attached to the outermost Ti atoms. The HRTEM image showing the atomic arrangement of bilayer $Ti_3C_2T_x$ and its corresponding atomistic model are presented in Fig. 3(f) [13], which clearly shows the existence of surface groups. The unit cell parameters of $Ti_3AlC_2$ and $Ti_3C_2T_x$ obtained by density functional theory (DFT) calculations are listed in Table 1. The interlayer spacing and equiangular lattice spacing of $Ti_2CT_x$ were approximately 9.82 Å (Fig. 3(g)) [31] and 2.54 Å (Fig. 3(h)) [32], respectively, which matches well with the results obtained by density functional theory (DFT) calculations (Table 1) [13]. Moreover, there is another form of $Ti_2CT_x$ (T = –O, –OH, and –F) in $Ti_{n+1}C_nT_x$, and its fabrication method differs, mainly in terms of the HF concentration and the reaction time. To fabricate $Ti_2CT_x$, Al is removed from the $Ti_2AlC$ powders using a 10% concentrated HF solution; the reaction lasts 10 h, and the reactant is washed several times.

High-yield production methods of high-quality $Ti_{n+1}C_nT_x$ are influenced by the synthesis routes used. Direct concentrated HF etching is an efficient method for

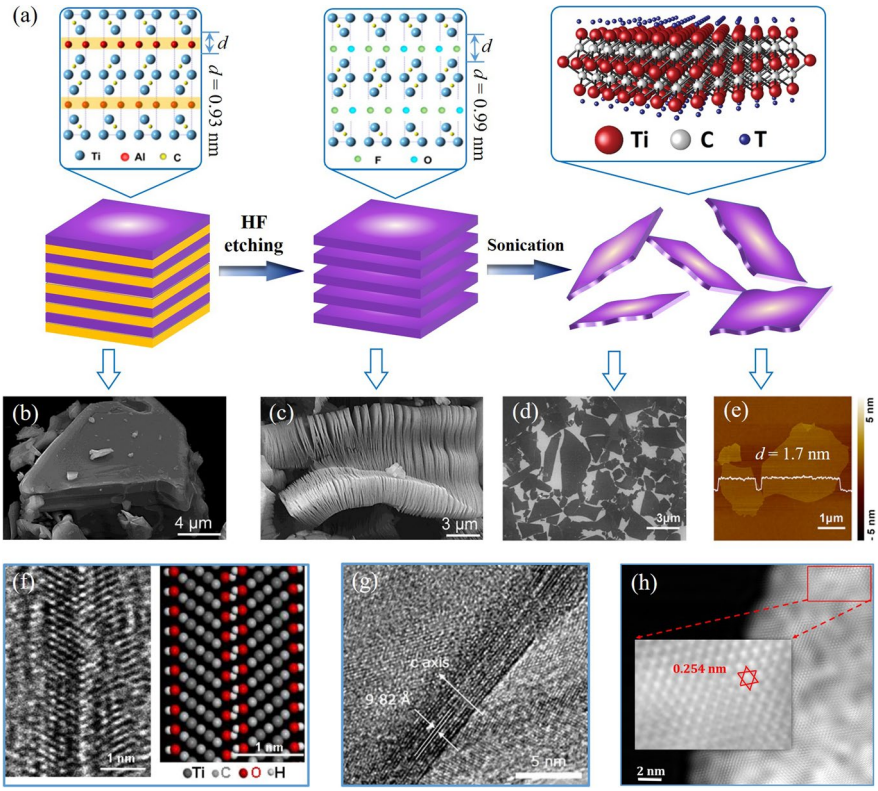


**Fig. 3** **a** Flow chart of etching $Ti_3AlC_2$ powders to obtain exfoliated 2D $Ti_3C_2T_x$ layers [27]. Copyright 2017, Elsevier. **b** Typical SEM image of Ti3AlC2 powders before HF etching [28]. **c** The SEM image obtained after the removal of 'Al' by HF etching [28]. Copyright 2019, American Chemical Society. **d** SEM and **e** TEM images of the exfoliated 2D Ti3C2Tx flakes after sonication [29]. Copyright 2020, American Chemical Society. f HRTEM image of bilayer Ti3C2Tx and its corresponding atomistic model [13]. Copyright 2011, Wiley–VCH. **g** HRTEM image showing the exfoliated 2D Ti3C2Tx after sonication, and the interlayer spacing is characterized to be 9.82 Å [31]. Copyright 2018, Wiley–VCH. h HRTEM image of Ti3C2Tx with an equiangular lattice spacing of ~2.54 Å, which matches well with the result obtained by DFT calculation (Table 1) [32]. Copyright 2018, Wiley–VCH

**Table 1** Unit cell parameters of $Ti_3AlC_2$ and $Ti_3C_2T_x$ obtained by the DFT calculations [13]

| | Unit Cell Parameters (Å) | | Volume change |
|---|---|---|---|
| **Formula** | **a = b** | **c** | |
| $Ti_3AlC_2$ (Exp.) | 3.080 | 18.415 | - |
| $Ti_3AlC_2$ | 3.058 | 18.554 | - |
| $Ti_3C_2$ | 3.048 | 15.006 | -19% |
| $Ti_3C_2(OH)_2$ | 3.059 | 19.494 | +5% |
| $Ti_3C_2F_2$ | 3.019 | 21.541 | +16% |

fabricating 2D $Ti_{n+1}C_nT_x$; however, it causes harm to humans and the environment. Therefore, other alternative low-risk and environmentally friendly etching routes have been developed (Fig. 4(a)) to avoid the direct use of concentrated HF [33], such as in-situ HF etching [34–36], alkaline etching [37–39], and Lewis acid molten salt etching [40, 41]. These approaches can effectively avoid or reduce the direct use of

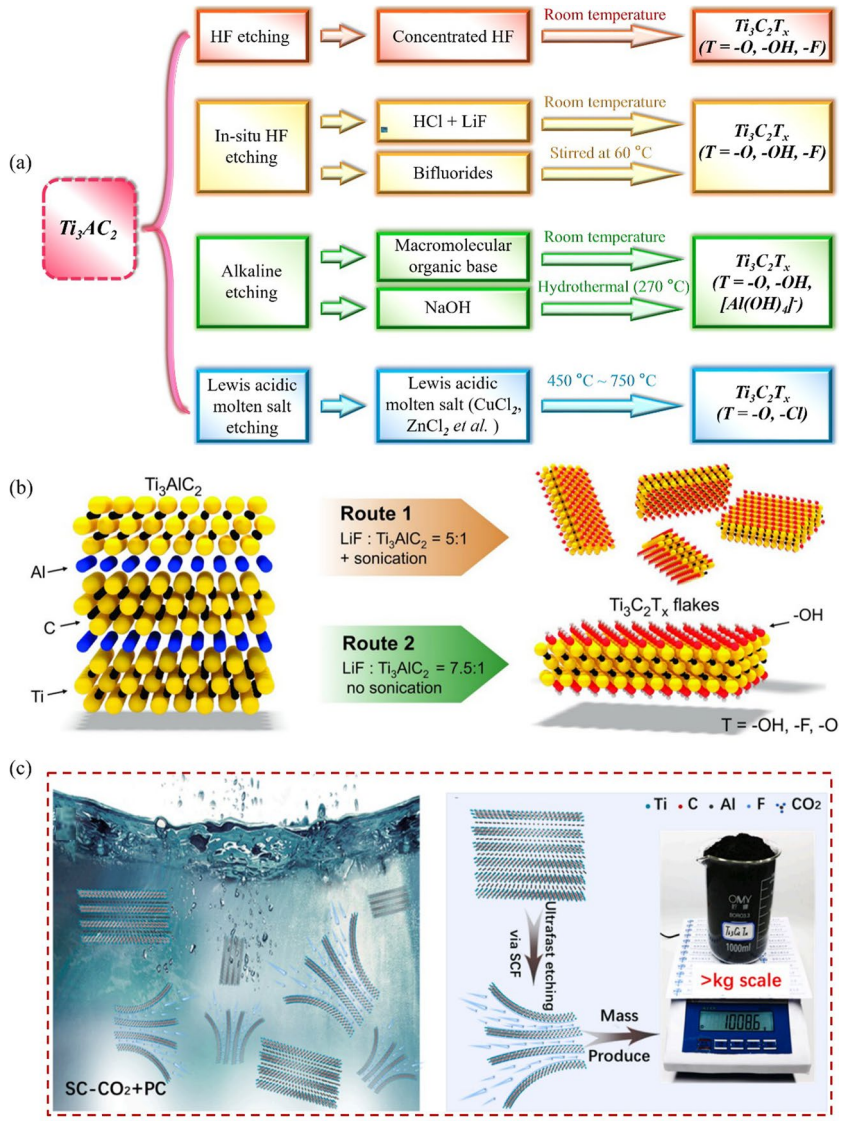


**Fig. 4** (**a**) Recent developments in methods of synthesizing Ti3C2Tx [33]. (**b**) Synthesis of Ti3C2Tx flakes by in-situ HF etching [36]. Copyright 2011, Wiley-VCH. (**c**) The supercritical exfoliation method for high-yield manufacture of MXenes [48]. Copyright 2023, Elsevier

HF, while successfully yielding $Ti_{n+1}C_nT_x$. Among these methods, using a mixture of HCl and LiF for in situ HF etching is the most widely used method, which was proposed by Ghidiu et al. [35] $Ti_3C_2T_x$ was synthesized by immersing $Ti_3AlC_2$ in a LiF–HCl solution, with a LiF to $Ti_3AlC_2$ molar ratio of 5:1. The preparation of MXenes by HF etching requires an additional step of inserting organic molecules, such as amines [42, 43] and dimethyl sulphoxide (DMSO) [44], while for LiF–HCl etching, $Ti_{n+1}C_nT_x$ can be layered immediately by ultrasonic treatment in water [35, 36]. Lipatov et al. modified the route proposed by Ghidiu and proposed increasing the molar ratio of LiF to $Ti_3AlC_2$ to 7.5:1, thus eliminating the ultrasonic layering step (Fig. 4(b)) [36]. Schematics of the LiF–HCl etching method is presented in Table 2. In addition to LiF, other fluoride salts, such as KF, NaF, $FeF_3$, $CaF_2$, and CsF, can also be used for

**Table 2** Routes based on LiF-HCl etching [36]

| Routes | Molar ratio $Ti_3AlC_2$: LiF: HCl | Etching time | Sonication |
|---|---|---|---|
| Route proposed by Ghidiu et al. | 1: 5:11.7 | 24 h | Yes, 1 h |
| Route proposed by Lipatov et al. | 1: 7.5: 23.4 | 24 h | No |

mixing with HCl as the etchant [45, 46]. Xu et al. systematically discussed and summarized the synthesis routes and delamination strategies of MXenes, and prospected a promising large-scale preparation scheme, providing important insights for preparing MXenes [47].

The F-containing acid etching method with strong environmental hazards and low yield are important factors restricting the development of MXenes. How to develop an environmentally friendly etching method and increase the yield of MXenes is a challenge for researchers. Recently, Yang et al. [48] proposed a supercritical exfoliation method to achieve high-yield manufacture of $Ti_3C_2T_x$ MXene in a short period of time (Fig. 4(c)). They put the MAX materials in a supercritical carbon dioxide (SC-$CO_2$) environment, and the intense thermal motion between supercritical $CO_2$ molecules will promote the in-situ generated HF of $NH_4HF_2$ to penetrate into the MAX phase faster and quickly remove the by-products of etching. Finally, they successfully mass-produced 5 kinds of MXene materials.

## Properties of $Ti_{n+1}C_nT_x$ MXenes in sensing technology

$Ti_{n+1}C_nT_x$ MXenes possess good electrical conductivity, excellent hydrophilicity, high specific surface area, and abundant surface functional groups, which make them ideal candidates for sensing technologies. Furthermore, modification of MXenes or modifying with other materials can significantly improve or change their properties, making them multifunctional and enabling a wide range of sensing applications.

### Computational properties

Generally, the theoretical calculation researches of MXenes are based on the density functional theory (DFT). Using this calculation method, the structural stability and physical properties of MXenes can be predicted, which has important guiding significance for the experimental researches. In 2011, $Ti_3C_2$, the first MXene material [13], was successfully experimentally fabricated by Naguib et al. Using the DFT calculation, it was determined that the bandgap structure of a single $Ti_3C_2$ layer resembles that of a typical semimetal with a finite density of states. Moreover, the unit cell parameters of $Ti_3AC_2$, $Ti_3C_2$, $Ti_3C_2(OH)_2$, and $Ti_3C_2F_2$ were also calculated in Table 1. The surface of MXene materials obtained by etching usually carries a large number of functional groups. Berdiyorov used DFT to analyze $Ti_3C_2$ carrying different functional groups, showing that different functional groups have a great influence on its refractive index, absorption and dielectric function [49]. For several allotropes of $Ti_{n+1}C_nT_x$, DFT calculation results indicate that they have good mechanical properties, and a smaller value of n results in stronger and stiffer MXenes [50].

For the $Ti_3C_2T_x$ MXene-based composites, Jiang et al. studied the electronic properties of MXene and graphene heterojunction by DFT calculation, and theoretically demonstrated that $Ti_3C_2(OH)_2$ has the strongest interaction with graphene [51] and demonstrated that has the strongest interaction with graphene. Electron transfers from $Ti_3C_2(OH)_2$ to graphene, which leads to a shift in the Dirac point of the graphene bands in the graphene-MXene heterostructures. In addition, the influence of the impurity ions on the structure of $Ti_3C_2$ MXene can also be calculated by theoretical method. Shi et al. used the x-ray atomic pair distribution function to analyze the effect of intercalated $Na^+$ and $K^+$ on the structure of $Ti_3C_2$ MXene, indicating that $Na^+$ and $K^+$ increase the layer spacing of $Ti_3C_2$ MXene, but shrinks the in-plane *a* and *b* lattice parameters [10]. In summary, through theoretical calculations, it is found that various properties of $Ti_3C_2$ MXene materials can be modulated by changing functional groups, doping ions, and combining other materials, which makes it applicable in a wide range of fields.

#### Stability of MXenes

Lattice energy is an important basis for evaluating the stability of crystal materials; greater lattice energy implies more unstable crystal structures. Using first-principles calculations, Shein et al. determined that MXenes have negative lattice energy, which indicates that MXenes can exist stably at room temperature [19]. The pH of the colloidal solution of MXenes synthesized by etching was close to neutral after repeated centrifugal cleaning with deionized water. At this time, the zeta potential of MXene NSs was as high as − 80 mV, indicating a strong electrostatic repulsion force between the negatively charged few-layer/single-layer MXene NSs. Therefore, 2D MXene NSs can form a stable colloidal solution in water [52]. However, the antioxidant capacity of MXenes in aqueous solutions is weak [53]. The chemical stability of MXenes is affected by the water and oxygen dissolved in water, and exposure to light can accelerate the oxidation of colloidal MXene solutions, forming metal oxide nanocrystals (such as $TiO_2$) [54, 55]. Li et al. [56] studied the thermal stability of MXenes and found that –F/–OH-terminated MXenes remained stable up to 800 °C in an Ar atmosphere; however, at 200 °C in an oxygen atmosphere, they were partially oxidized. Refrigeration and storage in a low-temperature and oxygen-free dark environment can significantly improve the stability of MXenes [53]. To improve the chemical stability of MXenes, Liu et al. [18] synthesized an aramid nanofiber@MXene coaxial fiber with excellent antioxidant properties that could withstand extreme conditions, such as strong acidity, strong alkalinity, high humidity, high salinity, and high temperature. The electrical resistance and electromagnetic shielding properties of the aramid nanofiber@MXene coaxial fiber remained mostly stable under these extreme environmental conditions, proving their good environmental stability.

#### Optical properties of MXenes

MXenes have abundant surface functional groups, and different of functional groups change the electronic properties of the material, thereby affecting its optical properties [57, 58]. The optical properties of MXenes can be adjusted by controlling the types and ratios of surface functional groups. The UV–Vis light absorption of MXenes is closely related to their thickness, size, and method used for modification. In the range of 300–500 nm, the light transmittance of 5 nm $Ti_3C_2T_x$ MXene films reached 91.2%; as

the film thickness increased to 70 nm, light transmittance decreased to 43.8% [59, 60]. Related studies have shown that the absorbance decreases as the lateral size of MXene flakes decreases [61]. Interestingly, the transmittance of MXene films can be optimized by changing the inserted ion species [59]. When hydrazine, urea, and DMSO are inserted, the transmittance of $Ti_3C_2T_x$ films decreases, while it increases when $NMe_4OH$ is inserted. Additionally, MXenes are also an excellent nonlinear material with tunable optical nonlinearity, and they are widely used for developing all-optical devices [32, 62–64].

#### Hydrophilicity of MXenes

The abundant functional groups on the surfaces of MXenes endow them good hydrophilicity. Depending on the type of functional groups, the water contact angle ranges from 21.5° to 35° [16, 44]. Wang et al. [65] mixed MXene and polyvinyl alcohol (PVA) to prepare a PVA/MXene nanofiber film (water contact angle = 35.7°–24.5°), which exhibited excellent hydrophilicity compared with the unmodified MXene. Furthermore, the alkaline treatment of MXene increased the oxygen–fluorine ratio ([O]/[F]) in the functional groups, especially hydroxyl groups, which greatly improved the hydrophilicity of MXenes [66, 67].

#### Conductivity of MXenes

The electrical conductivity of MXenes can be optimized by changing their elemental composition or surface functional groups. Studies have shown that $Ti_{n+1}C_n$ MXenes without surface functional groups have metallic conductivity, which decreases with an increase in the value of n [68]. Shahzad et al. investigated the electrical conductivity of functional group-terminated MXenes and reported that $Ti_3C_2T_x$ MXenes have metal-like properties, with electrical conductivities as high as 4600 S $cm^{-1}$ [17]. Differences in the preparation process result in different proportions of various functional groups, which leads to differences in the conductivity. Ling et al. [69] demonstrated that the conductivity of pure $Ti_3C_2T_x$ MXene is 2400 S $cm^{-1}$ and that for the $Ti_3C_2T_x$/PVA composite is 220 S $cm^{-1}$. Recently, Liu et al. [18] reported an aramid nanofiber@MXene coaxial fiber with a highly oriented and low-defect structure, which exhibited a high conductivity of 3000 S $cm^{-1}$.

#### Mechanical properties of MXenes

Both molecular dynamics and DFT calculation results indicate that $Ti_{n+1}C_nT_x$ MXenes have good mechanical properties; a smaller value of n results in stronger and stiffer MXenes [50, 70]. Ling et al. [69] investigated the mechanical properties of MXenes and found that the $Ti_3C_2T_x$ film (thickness = ~3.3 μm) has a tensile strength of 22 ± 2 MPa and Young's modulus of 3.5 ± 0.01 GPa. When the MXene film was rolled into a hollow cylinder, it could support 4000 times its own weight. Mixing MXene with PVA in a composite film increased the tensile strength of the film by 34%, and its hollow cylinder could support approximately 15,000 times its own weight. Furthermore, some composites of MXene exhibit excellent mechanical flexibility (e.g., tensile elongation = ~1000%). For example, the composite of MXene and hydrogel can be stretched in knots at high strains and recovered in compression at 90% large strains [71].

### Thermal effect of MXenes

MXenes are excellent thermo-sensitive materials, and their heating process generates photo-thermal and electro-thermal effects [72–74]. Li et al. [72] fabricated an MXene aerogel fiber via dynamic sol–gel spinning, which exhibited strong electrothermal and photothermal effects. With an increase in input voltage, the temperature of the aerogel fibers gradually increased, and only 0.5 V input voltage was required to generate a thermal effect on the surface. When the input voltage reached 4.5 V, the surface temperature of the aerogel fibers was > 178 °C. Aerogel fibers have a high light absorption capacity, and the absorption rate in the near-infrared region is close to 100%. Under low-temperature conditions, the temperature of MXene aerogel fibers can increase to 40 °C after irradiation in sunlight for 2 min, indicating that the aerogel fibers also have a light-to-heat conversion effect and thermal insulation function at extremely low temperatures.

## $Ti_{n+1}C_nT_x$ MXene-based sensing technologies

### SPR sensors

SPR sensing is an advanced detection technique that does not require fluorescent or enzymatic labels, and it can offer label-free and rapid real-time detection. Conventional SPR sensors are not sufficiently sensitive to trace small molecules [75], such as explosive materials, insecticides, and hormones. In the past decade, several 2D materials have been developed, and the research on SPR sensors based on enhanced 2D materials has attracted considerable attention [76–78]. Graphene is the foremost 2D material used to enhance the sensitivity of SPR sensors; the metasurface of graphene–gold has been reported to greatly enhance the electric field at the sensing interface, thereby improving the sensing sensitivity [79, 80]. Herein, we summarize the application of a graphene-like material, namely $Ti_{n+1}C_nT_x$ MXene, in SPR sensing. At present, the application of $Ti_{n+1}C_nT_x$ MXenes in SPR sensing mainly relies on two platforms, namely prism- [26, 81, 82] and fiber-type sensing structures [83]. Typically, Au thin films are used in both these structures to excite the SPR signal owing to their strong oxidation resistance. The application of MXene in SPR sensing technology utilizes its light absorption properties. Due to light absorption, MXene materials generate a large number of photogenerated carriers, and combining them with SPR sensors can greatly enhance the electric field strength at the sensing interface, thereby improving the sensing sensitivity.

Figure 5(a) shows a prism-type SPR sensor covered with $Ti_3C_2T_x$ MXene. MXene-Au metasurface greatly improves the sensitivity of the SPR sensor [81]. Although the refractive index (RI) of the analyte changes only slightly, it can be effectively tracked and detected by the SPR signal (Fig. 5(b)) [81]. Theoretical calculations and analyses show that the optimal number of MXene layers is 4, which can improve the sensitivity by 16.8% (Fig. 5(c)) [81]. SPR technology can also be applied in bio-sensing by multiple modifications of $Ti_3C_2T_x$ MXenes. Wu et al. [26] designed an ultrasensitive MXene-based SPR biosensor to achieve effective detection of carcinoembryonic antigen (CEA) with a low detection limit (0.07 fM). They used the $Ti_3C_2T_x$ film as the carrier and decorated it with Au nanoparticles (AuNPs) to construct $Ti_3C_2T_x$–AuNPs nanocomposites. Then, AuNPs were modified with staphylococcal protein A (SPA) to immobilize monoclonal anti-CEA antibodies (Fig. 5(d)). By using the sensing platform of $Ti_3C_2$–MXene/

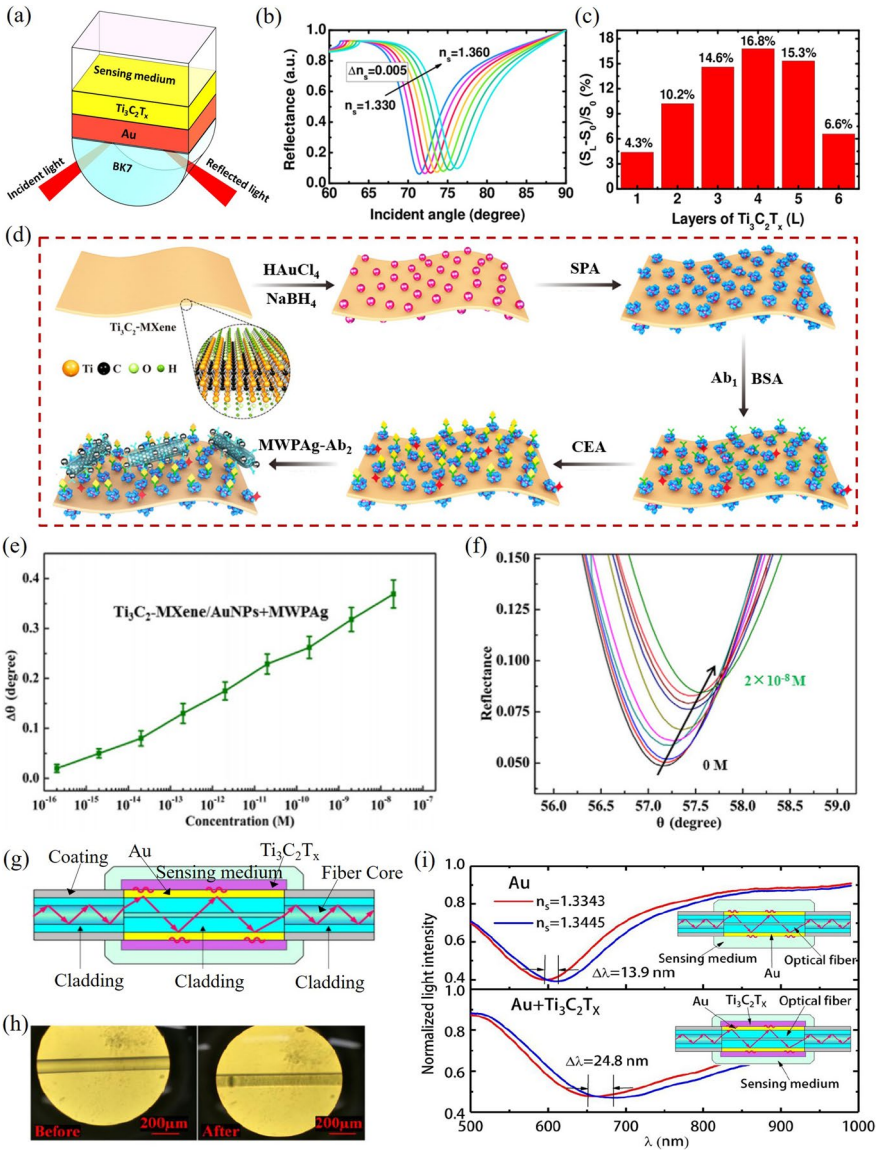


**Fig. 5** **a** Kretchmann configuration-based SPR sensor covered with $Ti_3C_2T_x$ MXene [81]. **b** Sensitive detection of diverse sensing analytes by SPR signals enhanced with $Ti_3C_2T_x$ MXene [81]. **c** Sensitivity enhancement by different number of $Ti_3C_2T_x$ layers [81]. Copyright 2018, Elsevier. **d** Applications of MXene/AuNPs + MWPAg hybrid structure in SPR bio-sensing for detecting CEA [26]. **e** Resonance angle shift for different concentration of CEA [26]. **f** Variation of SPR signal when the concentration of CEA changes from $2 \times 10^{-16}$ to $2 \times 10^{-8}$ M [26]. Copyright 2019, Elsevier. g Structure diagram of the MXene/Au-based fiber SPR sensor [83]. **h** Micrograph images of the fiber SPR sensor before and after Ti3C2Tx MXene self-installation [83]. **i** Enhancement of the resonance wavelength shift for the fiber SPR sensor by coated $Ti_3C_2T_x$ MXene [83]. Copyright 2020, American Chemical Society

AuNPs/SPA, CEA was selected and effectively sensed, as shown in Fig. 5(e) and (f). Different from the prism-type sensing structure, the optical fiber-type SPR sensor can detect spectral information, and the biological or chemical reaction processes are judged by the detected spectral shift. Using optical fiber as the sensing carrier, Chen et al. [83] uniformly coated $Ti_3C_2T_x$ MXene NSs on Au-coated optical fibers to design a highly sensitive RI sensor. The structure of the $Ti_3C_2T_x$ MXene/Au-based fiber SPR sensor is

shown in Fig. 5(g), and the microscopic images are shown in Fig. 5(h). The comparison results indicate that coating with $Ti_3C_2T_x$ MXene can increase the shift of the resonance wavelength, thereby improving the sensitivity (Fig. 5(i)).

#### Gas sensors

Large surface area of 2D materials allows more reactions on their surface, making them important candidates for gas sensing [29, 84, 85]. MXene and its modifications are emerging 2D materials with excellent metallic conductivity, functionalized surfaces, and large surface-to-volume ratios [86], and they are widely used in gas sensors. In this section, we discuss and overview the application of $Ti_3C_2T_x$ MXenes and their modified materials in gas sensing. Figure 6(a) shows a $Ti_3C_2T_x$ MXene-based gas sensor designed by Kim et al. [87] The detection limit of the $Ti_3C_2T_x$ gas sensor for volatile organic compounds was as low as 50–100 ppb at room temperature. It also showed good selective detection of ethanol gas (Fig. 6(b)) [87]. To improve the gas response, Chen et al. proposed a gas sensing material composed of a combination of $Ti_3C_2T_x$ MXene and $WSe_2$ in a nanohybrid structure [88]. Through electrostatic interactions, $WSe_2$ was compounded on the surface of the $Ti_3C_2T_x$ MXene, fabricating the $Ti_3C_2T_x/WSe_2$ nanohybrid (Fig. 6(c)). Compared with $Ti_3C_2T_x$, the $Ti_3C_2T_x/WSe_2$ nanohybrid provided a large number of heterointerfaces, which significantly increased the adsorbed oxygen species, thereby trapping more electrons. When the $Ti_3C_2T_x/WSe_2$ nanohybrid was exposed to volatile organic compounds, the adsorbed active oxygen species on the surface reacted with ethanol to form carbon dioxide and water (Fig. 6(d)). The $Ti_3C_2T_x/WSe_2$ nanohybrid possessed more abundant adsorbed oxygen species, and thus, it had a stronger gas response to volatile organic compounds (Fig. 6(e)). The modification of $Ti_3C_2T_x$ MXene with polyaniline also increased the catalytic sensitivity, enabling the selective detection of ethanol with stronger gas response [89].

Modified $Ti_3C_2T_x$ MXenes enable the selective detection of ethanol gas, and they can be modified by other methods to achieve selective gas detection. Zhou et al. reported a gas sensing material of $Ti_3C_2T_x$-derived nitrogen-functionalized heterophase $TiO_2$ homojunctions (N-MXenes), which could achieve selective detection of ammonia ($NH_3$) [90]. Figure 6(f) shows the fabrication method of N-MXenes. $Ti_3C_2T_x$ was subjected to a urea-involved solvothermal reaction at 180 °C for 18 h, and then, the Ti atoms of $Ti_3C_2T_x$ MXene were oxidized to $TiO_2$. With the increase in oxidation time, the outer surface of MXene was covered by $TiO_2$ nanoparticles, and finally, N–MXene was

(See figure on next page.)

**Fig. 6** **a** Schematic illustration of the $Ti_3C_2T_x$ MXene-based gas sensor [87]. **b** Selective detection of ethanol by $Ti_3C_2T_x$ gas sensor [87]. Copyright 2018, American Chemical Society. c Fabrication of $Ti_3C_2T_x/WSe_2$ hybrids [88]. **d** Mechanism of sensing enhancement for the $Ti_3C_2T_x/WSe_2$ hybrid [88]. **e** Comparison of the detection ability of $Ti_3C_2T_x$ and $Ti_3C_2T_x/WSe_2$ hybrid for various volatile organic compounds at 40 ppm [88]. Copyright 2020, Springer Nature. f $Ti_3C_2T_x$ treated by urea-involved solvothermal reactions to obtain the nitrogen-functionalized heterophase $TiO_2$ homojunctions (N-MXene) [90]. g Selectivity detection of $NH_3$ by modified the N-MXene [90]. Copyright 2021, American Chemical Society. **h** Alkaline MXene to enhance gas response to ammonia $NH_3$ [67]. Copyright 2019, American Chemical Society. **i** MXene/rGO hybrid structure to selected detection of $NH_3$ [29]. Copyright 2020, American Chemical Society. **j** Selective detection of the $Ti_3C_2T_x$ MXene/PANI/BC composite aerogel-based gas sensor with high gas response [91]. Copyright 2021, American Chemical Society

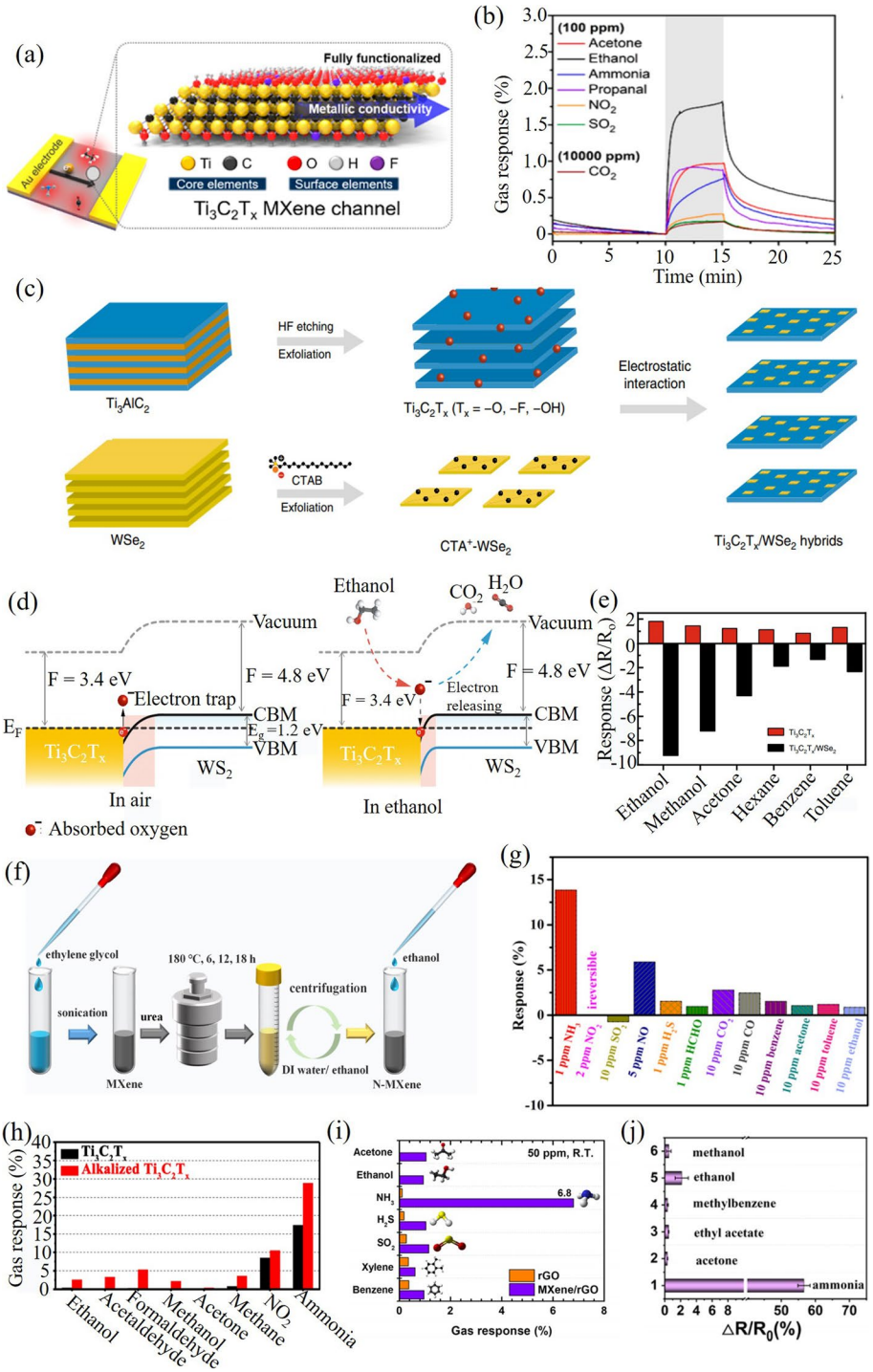


**Fig. 6** (See legend on previous page.)

formed. Thereafter, the as-prepared N–MXene was sprayed onto an interdigital electrode device to fabricate the N–MXene-based gas sensor. The detection results indicated that the N–MXene-based gas sensor had selective detection ability for $NH_3$ (Fig. 6(g)), and the detection limit was 200 ppb. Wang et al. grew ZnO nanorods on the surface

of $Ti_3C_2T_x$ (MXene/ZnO nanorod hybrids) to fabricate a novel light-activated $NO_2$ gas sensor, which has a high sensitivity, and the detection limit was 0.2 ppb [92]. To enhance the gas response of the $Ti_3C_2T_x$-based sensor, researchers have proposed many effective schemes in recent years, such as alkalized $Ti_3C_2T_x$ MXene (Fig. 6(h)) [67], MXene/rGO (reduced graphene oxide) hybrid fiber (Fig. 6(i)) [29], and $Ti_3C_2T_x$ MXene/PANI/BC composite aerogels (Fig. 6(j)) [91]. Table 3 summarizes the recent applications of MXenes and their modified composites in gas sensing.

#### Fluorescence sensors

$Ti_3C_2T_x$ MXenes, including NSs and QDs, are important in fluorescence sensors due to their unique optical properties. MXene NSs exhibit high fluorescence quenching ability, while MXene QDs have a strong fluorescence effect. $Ti_3C_2T_x$ NSs can be used as a fluorescent sensing platform for biological testing, such as HPV-18 DNA detection (Fig. 7(a)) [106]. The fluorescent probe (P) single-stranded DNA (ssDNA) of HPV-18 exhibits strong fluorescence (Fig. 7(b)); it was mixed with a certain amount of $Ti_3C_2T_x$ NSs; thereafter, the probe ssDNA was adsorbed on the surface of an MXene; the fluorescence was greatly quenched. Thereafter, the target (T) ssDNA was injected into the $Ti_3C_2T_x$ MXene solution modified with the probe ssDNA; the target ssDNA was then combined with the probe ssDNA to form double-stranded DNA (dsDNA). At this time, the dsDNA was detached from the MXene surface, and the fluorescence was restored. To improve sensitivity, exonuclease III (Exo III) was used as a sensitizer to amplify changes in the fluorescence signals. By comparison, after adding Exo III, changes in the fluorescence signals were greatly enhanced (Fig. 7(b)). Based on the advantages of the quenching and recovery of fluorescence during DNA adsorption and detachment, a pathway for detection of HPV-18 virus was proposed (Fig. 7(c)). Changes of fluorescence intensity were measured when the concentration of target ssDNA was in the range 0–50 nM. The results showed that layered $Ti_3C_2T_x$ is a suitable sensing platform for HPV virus detection, with a low detection limit of 100 pM.

When the lateral dimensions of $Ti_3C_2T_x$ MXenes were decreased to several nanometers, they transformed into QDs (Fig. 7(d)) [107] with photoluminescent properties [107, 111]. $Ti_3C_2T_x$ MXene QDs have excellent fluorescence properties, and their fluorescence characteristics vary under different excitation wavelengths, which are suitable for fluorescence sensing of biological macromolecules such as metal ions, small organic molecules, and enzymes [108, 112, 113]. Desai et al. fabricated ultra-small $Ti_3C_2T_x$ MXene QDs and used them for metal ion detection [108]. The fluorescence signal excited by $Ti_3C_2T_x$ MXene QDs was highly sensitive and could selectively detect $Ag^+$ and $Mn^{2+}$ ions (Fig. 7(e)), with the detection limits for $Ag^+$ and $Mn^{2+}$ ions being 9.7 and 102 nM, respectively. Chen et al. co-hydrothermally synthesized $Ti_3C_2T_x$ MXene QDs with polyethyleneimine (PEI) to synthesize surface-functionalized $Ti_3C_2T_x$ QDs [109]. The fluorescence effect of $Ti_3C_2T_x$ QDs exhibited sensitive pH-responsivity. By linking it with a pH-insensitive dye $[Ru(dpp)_3]Cl_2$, a pH-responsive proportional fluorescent probe was constructed, which was used for intracellular pH determination (Fig. 7(f)). Guan et al. functionalized $Ti_3C_2T_x$ MXene QDs with nitrogen (N) and phosphorus (P) to fabricate the N, P–$Ti_3C_2T_x$ QDs [110]. The fluorescence of this new material exhibited selective detection of $Cu^{2+}$ ions, and the detection limit was as low as 2 μM (Fig. 7(g)). Moreover, the effective detection of

**Table 3** Summary of the $Ti_{n+1}C_nT_x$ ($n = 1, 2, 3$) MXene-based gas sensors

| Materials | Gas | Concentration (ppm) | Gas response (%) | Detection limit | References |
|---|---|---|---|---|---|
| $Ti_3C_2T_x$ | acetone | 100 | 0.97 | 50 ppb | [87] |
| | ethanol | 100 | 1.7 | 100 ppb | |
| | ammonia | 100 | 0.8 | 100 ppb | |
| | propanal | 100 | 0.88 | - | |
| $Ti_3C_2T_x$ | acetone | 100 | 7.5 | 9.27 ppm | [12] |
| | ethanol | 100 | 11.5 | - | |
| | methanol | 100 | 14.3 | - | |
| | ammonia | 100 | 21 | - | |
| 3D $Ti_3C_2T_x$ Mxene framework | acetone | 10 | 1.44 | 50 ppb | [93] |
| | ethanol | 10 | 1.74 | 50 ppb | |
| | methanol | 10 | 2.18 | 50 ppb | |
| | ammonia | 10 | 0.74 | - | |
| | thichloromethane | 10000 | 0.11 | - | |
| | water vapor | 10000 | 0.53 | - | |
| | $NO_2$ | 10 | 0.94 | - | |
| $Ti_3C_2T_x$ derived from graphite | ethanol | 100 | 0.125 | - | [94] |
| | acetone | 100 | 0.195 | - | |
| | ammonia | 5 | 0.55 | - | |
| $Ti_3C_2T_x$ derived from lampblack | ethanol | 100 | 0.1 | - | |
| | acetone | 100 | 0.15 | - | |
| | ammonia | 5 | 0.38 | - | |
| $Ti_3C_2T_x$ derived from TiC | ethanol | 100 | 0.158 | - | |
| | acetone | 100 | 0.23 | - | |
| | ammonia | 5 | 0.62 | - | |
| $Ti_3C_2T_x$ /polyaniline/bacterial cellulose | methanol | 1000 | 1.3 | - | [91] |
| | ethanol | 1000 | 6.3 | - | |
| | methylbenzene | 1000 | 0.8 | - | |
| | ethyl acetate | 1000 | 1.2 | - | |
| | acetone | 1000 | 0.92 | - | |
| | ammonia | 7.5 | 56.63 | 2.5 ppm | |
| Polyaniline/ $Ti_3C_2T_x$ | ethanol | 200 | 41 | 50 ppm | [89] |
| | methanol | 200 | 19 | - | |
| | ammonia | 200 | 19.8 | - | |
| | acetone | 200 | 20.5 | - | |
| $Ti_3C_2T_x/WSe_2$ | ethanol | 40 | -9.3 | 1 ppm | [88] |
| | methanol | 40 | -7.3 | - | |
| | acetone | 40 | -4.3 | - | |
| | hexane | 40 | -1.9 | - | |
| | benzene | 40 | -1.4 | - | |
| | toluene | 40 | -2.4 | - | |
| Polymeric $Ti_3C_2T_x$ | ammonia | 100 | 36.6 | 10 ppm | [95] |
| | toluene | 100 | 1.2 | - | |
| | ethanol | 100 | 4.6 | - | |
| | methanol | 100 | 14 | - | |
| | acetone | 100 | 3.4 | - | |

**Table 3** (continued)

| Materials | Gas | Concentration (ppm) | Gas response (%) | Detection limit | References |
|---|---|---|---|---|---|
| N-MXene | $NH_3$ | 1 | 13.9 | 0.2 ppm | [90] |
| | $SO_2$ | 10 | -0.78 | - | |
| | NO | 5 | 5.86 | - | |
| | $H_2S$ | 1 | 1.49 | - | |
| | HCHO | 1 | 0.95 | - | |
| | $CO_2$ | 10 | 2.76 | - | |
| | CO | 10 | 2.43 | - | |
| | benzene | 10 | 1.5 | - | |
| | acetone | 10 | 1.05 | - | |
| | toluene | 10 | 1.14 | - | |
| | ethanol | 10 | 0.87 | - | |
| MXene/rGO | acetone | 50 | 1.04 | - | [29] |
| | ethanol | 50 | 0.95 | - | |
| | $NH_3$ | 50 | 6.8 | 10 ppm | |
| | $H_2S$ | 50 | 1 | - | |
| | $SO_2$ | 50 | 1.13 | - | |
| | Xylene | 50 | 0.59 | - | |
| | benzene | 50 | 0.96 | - | |
| $TiO_2$/ $Ti_3C_2T_x$ | $NH_3$ | 10 | 3.1 | 0.5 ppm | [96] |
| | $H_2S$ | 10 | 0.29 | - | |
| | CO | 10 | 0.46 | - | |
| | $CH_4$ | 10 | 0.35 | - | |
| | HCHO | 10 | 0.2 | - | |
| | $CO_2$ | 10 | 0.81 | - | |
| Alkalized $Ti_3C_2T_x$ | ethanol | 100 | 2.47 | - | [67] |
| | acetaldehyde | 100 | 3.14 | - | |
| | formaldehyde | 100 | 5.25 | - | |
| | methanol | 100 | 2.15 | - | |
| | acetone | 100 | 0.43 | - | |
| | Methane | 100 | 3.54 | - | |
| | $NO_2$ | 100 | 10.41 | - | |
| | ammonia | 100 | 28.87 | 10 ppm | |
| single-layer $Ti_3C_2T_x$ MXene | $CH_4$ | 500 | 0.5 | - | [97] |
| | $H_2S$ | 500 | 0.16 | - | |
| | $H_2O$ | 500 | 0.39 | - | |
| | ethanol | 500 | 1.5 | - | |
| | methanol | 500 | 0.18 | - | |
| | acetone | 500 | 0.3 | - | |
| | $NH_3$ | 500 | 6.13 | 10 ppm | |
| | NO | 500 | 0.38 | - | |
| $W_{18}O_{49}$/$Ti_3C_2T_x$-2% | ethanol | 20 | 1.67 | - | [98] |
| | acetone | 20 | 11.6 | 170 ppb | |
| | formaldehyde | 20 | 1.2 | - | |
| | ammonia | 20 | 2 | - | |

**Table 3** (continued)

| Materials | Gas | Concentration (ppm) | Gas response (%) | Detection limit | References |
|---|---|---|---|---|---|
| $TiO_2$/ $Ti_3C_2T_x$-8 h | toluene | 5 | 0.40 | - | [99] |
| | ethanol | 5 | 0.32 | - | |
| | propanal | 5 | 0.42 | - | |
| | acetone | 5 | 0.52 | - | |
| | ammonia | 5 | 2.10 | - | |
| | $NO_2$ | 5 | 16.02 | 125 ppb | |
| $TiO_2$/ $Ti_2CT_x$ | $(CH_3)_2CO$ | 10 | 0.42 | - | [100] |
| | $NH_3$ | 10 | 1.93 | 0.1 ppm | |
| | HCHO | 10 | 0.52 | - | |
| | $C_2H_5OH$ | 10 | 0.35 | - | |
| | $H_2S$ | 10 | 0.25 | - | |
| | $C_6H_5CH_3$ | 10 | 0.24 | - | |
| | $NO_2$ | 10 | 0.36 | - | |
| Fluoroalkylsilane modified $Ti_2CT_x$ | acetone | 30 | 3.37 | - | [101] |
| | ethanol | 30 | 5.58 | - | |
| | 2-propanol | 30 | 2.73 | - | |
| | toluene | 30 | 0.74 | - | |
| | benzene | 30 | 0.61 | - | |
| | $NO_2$ | 30 | 1.16 | - | |
| MXene/ZnO nanorod hybrids | $NO_2$ | 50 | 80 | 0.2 ppb | [92] |
| $Ti_2CT_x$ MXene | $CH_4$ | 10000 | 68 | - | [102] |
| $Ti_3C_2T_x/WS_2$ | $NO_2$ | 20 | 55 | 10 ppb | [103] |
| MXene/$Co_3O_4$ composite | formaldehyde | 10 | 9.6 | 0.01 ppm | [104] |
| 3D crumpled MXene sphere/ ZnO | $NO_2$ | 100 | 41.93 | - | [105] |

many analytes has been achieved through special modifications of $Ti_3C_2T_x$ MXene QDs such as $CsPbBr_3$–$Ti_3C_2T_x$ MXene QD heterojunction [114], glutathione-functionalized $Ti_3C_2T_x$ QDs [115], and N-$Ti_3C_2T_x$ QDs/$Fe^{3+}$ [116]. Overall, $Ti_3C_2T_x$ can not only act as quenchers but also as fluorophores in different morphologies. MXene NSs act as quenchers, while MXene QDs act as fluorophores. The applications of $Ti_3C_2T_x$ NSs and $Ti_3C_2T_x$ QDs in fluorescence sensors are summarized in Table 4.

### SERS sensors

SERS possesses the advantages of photostability, non-destructiveness, fingerprint spectrum, and ultra-sensitivity at the single-molecule level [136, 137], and thus, it has been successfully applied in various fields such as biomedicine [138, 139], environmental monitoring [140, 141], and food safety [142, 143]. In general, SERS requires noble metal nanoparticles as substrates to exert a strong SPR effect [144, 145]. However, the application of noble metal-based SERS sensors is limited by the easy aggregation and oxidation of metal nanoparticles, along with the weak ability to adsorb molecules. To solve the problem of aggregation of metal nanoparticles and further enhance the intensity of

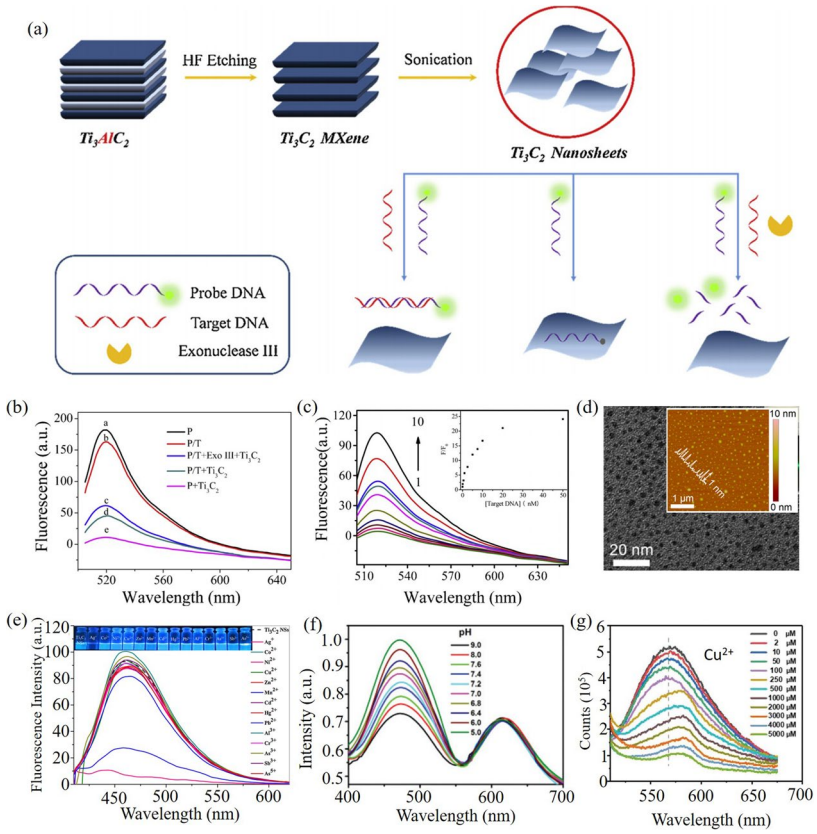


**Fig. 7** **a** $Ti_2CT_x$ served as bio-sensing material for detecting HPV-18 type DNA [106]. **b** Fluorescence spectra of the $Ti_3C_2T_x$ NSs-based fluorescence sensor under different conditions [106]. **c** Variation of the fluorescence spectra at different concentrations of target DNA [106]. Copyright 2019, Elsevier. **d** TEM and AFM images of $Ti_2CT_x$ MXene quantum dots (QDs) [107]. Copyright 2017, American Chemical Society. **e** Fluorescence spectra of $Ti_3C_2T_x$ MXene QDs after adding different metal ions [108]. Copyright 2019, Elsevier. **f** Fluorescence spectra of the PEI- $Ti_3C_2T_x$ QDs at different pH buffer solutions [109]. Copyright 2018, Royal Society of Chemistry. **g** Fluorescence spectra of the N, P-$Ti_3C_2T_x$ QDs with different concentrations of $Cu^{2+}$ ranging from 0 to 5000 μM [110]. Copyright 2019, Royal Society of Chemistry

Raman signals, researchers have proposed using MXenes as the substrates of SERS sensors. MXenes have the advantages of excellent hydrophilicity, large specific surface areas, and strong electrical conductivity, which make them suitable as substrates for SERS sensors [146]. In SERS sensors, metal nanoparticles can be used as amplifiers for Raman signal changes, and they are uniformly modified on the surfaces of MXenes. Recently, Wu et al. reported a highly sensitive Au nanoparticle dimer/$Ti_3C_2T_x$-based SERS sensor for detecting mycotoxin B1 (AFB1) [147]. First, Au nanoparticles were assembled using 1,2-bis(4-pyridyl) ethylene (BPE) to form Au nanoparticle dimers. Second, a nanogap smaller than 2 nm, called "hot spot," was formed in the Au nanoparticle dimer, which considerably enhanced the SERS signal. Thereafter, aptamer-modified Au nanoparticle dimers were linked with $Ti_3C_2T_x$ MXene NSs via hydrogen bonding and chelation. Finally, with the interaction of AFB1 with the structure of Au nanoparticle dimer/$Ti_3C_2T_x$ MXene, the AFB1 adhered to the aptamer-modified Au nanoparticle dimer, which had detached from the MXene surface (Fig. 8(a)); this strongly enhanced the SERS signal.

**Table 4** Summary of fluorescence sensors based on $Ti_3C_2T_x$ NSs and QDs

| Materials | Analytes | Linear range | Detection limit | References |
|---|---|---|---|---|
| $Ti_3C_2T_x$ NSs | HPV-18 DNA | 0.5–50 nM | 100 pM | [106] |
| Rhodamine B-labeled phospholipid $Ti_3C_2T_x$ NSs | phospholipase D | 0–1000 U $L^{-1}$ | 0.1 U $L^{-1}$ | [113] |
| DNA-functionalized $Ti_3C_2T_x$ NSs | mucin 1 | 0 — 60 nM | 6 nM | [117] |
| | microRNA-21 | 0 — 25 nM | 0.8 nM | |
| $Ti_3C_2T_x$ NSs combined with red-emitting carbon dots | glucose | 0.1 — 20 mM | 50 μM | [118] |
| (Cy3-CD63 aptamer)/ $Ti_3C_2T_x$ NSs | exosome | $10^4$ — $10^9$ particles $mL^{-1}$ | $1.4 \times 10^3$ particles $mL^{-1}$ | [119] |
| NaYF4:Yb, Tm/Er UCNPs and $Ti_3C_2T_x$ NSs | miRNA-21 | 5 fM–100 pM | 0.62 fM | [120] |
| | miRNA-10b | 5 fM–100 pM | 0.85 fM | |
| Cu nanoclusters x functionalized $Ti_3C_2T_x$ NSs | glutathione | 5.0 – 100 μM | 3 μM | [121] |
| TAT peptide-functionalized $Ti_3C_2T_x$ NSs | lncRNA PCA3 | 0 – 0.2 nM | 2.6 pM | [122] |
| Chimeric peptide-functionalized $Ti_3C_2T_x$ NSs | protein phosphatase 2C | 15 — 200 nM | 2.3 nM | [123] |
| $Ti_3C_2T_x$ NSs | Vibrio parahaemolyticus | $10^2$ — $10^6$ cfu/mL | 30 cfu/mL | [124] |
| Exo III-assisted recycling $Ti_3C_2T_x$ NSs | $Hg^{2+}$ | 0.05–50 nM | 0.0425 nM | [125] |
| $Ti_3C_2T_x$ NSs | thrombin | 20–200 pM | 5.27 pM | [126] |
| Dimethylformamide — $Ti_3C_2T_x$ MXene QDs | $Fe^{3+}$ | 0 – 830 μM | 2 μM | [127] |
| N, P — $Ti_3C_2T_x$ QDs | $Cu^{2+}$ | 0 – 5000 μM | 2 μM | [110] |
| $Ti_3C_2T_x$ QDs | alkaline phosphatase | 0 – 50 U $L^{-1}$ | 0.02 U $L^{-1}$ | [128] |
| $CsPbBr_3$ — $Ti_3C_2T_x$ MXene QDs Heterojunction | $Cd^{2+}$ | $9.9 \times 10^{-5}$ –$5.9 \times 10^{-4}$ M | – | [114] |
| Glutathione functionalized $Ti_3C_2T_x$ QDs | uric acid | 1.2 –75 mM | 125 nM | [115] |
| N — $Ti_3C_2T_x$ QDs/$Fe^{3+}$ | glutathione | 0.5 – 100 μM | 0.17 μM | [116] |
| PEI — $Ti_3C_2T_x$ QDs | pH values | 6 – 8 | – | [109] |
| ε-poly-L-lysine functionalized $Ti_3C_2T_x$ QDs | cytochrome c | 0.2 – 40 μM | 20.5 nM | [129] |
| Nitrogen-doped $Ti_3C_2T_x$ QDs | $H_2O_2$ | 2 — 50 μM | 0.57 μM | [130] |
| | Xanthine | 1 — 50 μM | 0.34 μM | |
| $Ti_3C_2T_x$ QDs | curcumin | 0.05–10 μM | 20 nM | [131] |
| | $ClO^-$ | 25–150 μM and 150–275 μM | 5 μM | |
| Uric acid@$Ti_3C_2T_x$ QDs | 2,4,6-trinitrophenol | 0.01–40 μM | 9.58 nM | [132] |
| $Ti_3C_2T_x$ QDs | $Fe^{3+}$ | 0–1000 μM | 310 nM | [133] |
| Nitrogen-doped $Ti_3C_2T_x$ QDs | $Cu^{2+}$ | 0–2000 μM | — | [134] |
| $Ti_3C_2T_x$ MXene QDs | $Ag^+$ | 0.1–40 μM | 9.7 nM | [108] |
| | $Mn^{2+}$ | 0.5 – 60 μM | 102 nM | |
| N, P-doped $Ti_3C_2T_X$ QDs | $NO_2^-$ | 1.5 – 80 μM | 0.25 μM | [135] |

Figure 8(b) shows the SERS intensity enhanced by the $Ti_3C_2T_x$ MXene NSs with the Au nanoparticle dimer/$Ti_3C_2T_x$ MXene structure. Equal volumes of Au NP dimer and $Ti_3C_2T_x$ MXene NSs were mixed and the intensity of the SERS signal gradually increased with the increase in $Ti_3C_2T_x$ concentration; it was the strongest at the

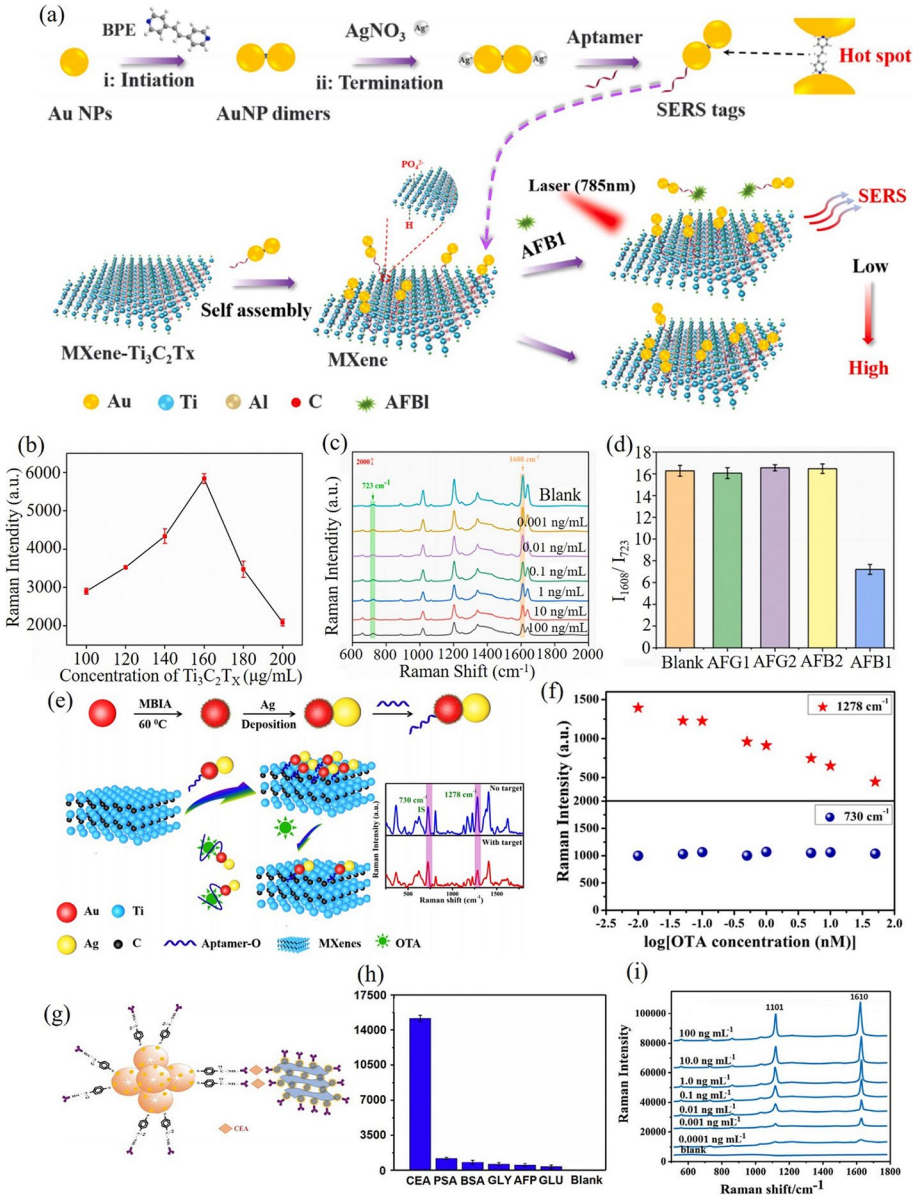


**Fig. 8** **a** Fabrication of Au nanoparticle dimers/$Ti_3C_2T_x$ MXenes assemblies-based SERS sensor for the detection of AFB1 [147]. **b** Raman intensities of Au nanoparticle dimers/$Ti_3C_2T_x$ MXenes assemblies at different concentrations of $Ti_3C_2T_x$ NSs [147]. **c** SERS spectra of the Au nanoparticle dimers/MXenes assemblies-based SERS sensor with different concentrations of mycotoxin B1 [147]. **d** Selective detection of AFB1 for the Au nanoparticle dimers/$Ti_3C_2T_x$ MXene-based SERS sensor [147]. Copyright 2022, Elsevier. **e** Au — Ag Janus nanoparticles/ $Ti_3C_2T_x$ NSs-based SERS sensor for the detection of ochratoxin A [145]. **f** SERS signals of Au — Ag Janus nanoparticles at 1278 $cm^{-1}$ and $Ti_3C_2T_x$ NSs at 730 $cm^{-1}$ with different concentrations of ochratoxin A [145]. Copyright 2019, American Chemical Society. **g** The sandwich SERS sensor [148]. **h** Selective detection of carcinoembryonic antigen by the sandwich type SERS sensor [148]. **i** SERS spectra of the sandwich type SERS sensor at different concentrations of carcinoembryonic antigen [148]. Copyright 2020, Elsevier

optimal concentration of 160 μg·mL$^{-1}$. Using the Au nanoparticle dimer/$Ti_3C_2T_x$ MXene-based SERS sensor, AFB1 was effectively detected in the concentration range of 0.001–100 ng·mL$^{-1}$, and the detection limit was 0.6 pg·mL$^{-1}$ (Fig. 8(c)). The SERS sensor also exhibited selective detection of AFB1 (Fig. 8(d)). Compared with the ratiometric intensities of Blank, AFG1, AFG2, and AFB2, the detection result of AFB1 was distinctive, indicating its excellent selective detection. Zheng et al. used $Ti_3C_2T_x$ MXenes as substrates and linked aptamer-modified Au–Ag Janus nanoparticles on it to achieve highly sensitive detection of ochratoxin A (Fig. 8(e)) [145]. The SERS signals of Au–Ag Janus nanoparticles at 1278 cm$^{-1}$ and $Ti_3C_2T_x$ NSs at 730 cm$^{-1}$ with different concentrations of ochratoxin A are presented in Fig. 8(f), indicating that the SERS intensity at 1278 cm$^{-1}$ was sensitive to the change of ochratoxin A concentration, while the SERS intensity at 730 cm$^{-1}$ remained almost unchanged. By analyzing the variation in the ratiometric peak intensity ($I_{1278}/I_{730}$), the concentration change (0.01–50 nM) of ochratoxin A was effectively detected, and the detection limit was 1.28 pM. Medetalibeyoglu et al. presented a sandwich-type SERS sensor using $MoS_2$ nanoflowers@Au nanoparticles and $Fe_3O_4$@Au nanoparticle-functionalized $Ti_3C_2T_x$ NSs as CEASERS tags and SERS substrates, respectively, for the detection of carcinoembryonic antigen (Fig. 8(g)) [148]. The sandwich-type SERS sensor exhibited selective detection of carcinoembryonic antigen (Fig. 8(h)). The SERS signal achieved effective tracking and detection when the concentration of carcinoembryonic antigen changed from 0.0001 to 100.0 ng mL$^{-1}$; the detection limit was calculated to be 0.033 pg mL$^{-1}$ (Fig. 8(i)). In addition to the aforementioned sensors, other MXene-based SERS sensors with high performance have been reported in recent years, and the main performance indicators are presented in Table 5.

### Colorimetric sensors

Colorimetric sensing technology is an important analysis method that is widely used, due to its advantages of high sensitivity, low cost, short color development time, obvious phenomenon, visualization, convenience and quickness. $Ti_3C_2T_x$-based colorimetric sensing technology, a visualized and ultrasensitive assay, has garnered extensive attention in recent years. This sensing technology mainly includes two types of detection methods, namely retouch-free and retouched. The difference between these two methods is that the retouch-free assay enables direct interaction between the sensing material and the analyte, while the retouched assay requires probe or dye modification of the sensing material to detect specific targets. For the retouch-free assay, Wang et al. reported a colorimetric sensing strategy based on $Ti_3C_2T_x$ MXene NS-mediated

**Table 5** MXene-based SERS sensors

| Materials | Analytes | Linear range | Detection limit | References |
|---|---|---|---|---|
| $Fe_3O_4$ NPs@Au NPs $Ti_3C_2T_X$ MXene | carcinoembryonic antigen | 0.0001 — 100.0 ng mL$^{-1}$ | 0.033 pg mL$^{-1}$ | [148] |
| Au — Ag Janus nanoparticles/$Ti_3C_2T_x$ assemblies | ochratoxin A | 0.01 — 50 nM | 1.28 pM | [145] |
| Au nanoparticle dimers/$Ti_3C_2T_x$ assemblies | mycotoxin B1 | 0.001 — 100 ng·mL$^{-1}$ | 0.6 pg·mL$^{-1}$ | [147] |
| $Ti_3C_2T_x$ -Ag nanocomplex | biomolecules | $5 \times 10^{-6} - 5 \times 10^{-8}$ M | $10^{-8}$ M | [149] |
| $Ti_3C_2T_x$ | dye molecule rhodamine | $10^{-3}$–$10^{-6}$ M | $10^{-6}$ M | [150] |

in situ reduction for ultrasensitive detection of $Ag^+$ (Fig. 9(a)) [151]. First, the stability of the $Ti_3C_2T_x$ MXene NS was improved by carboxy-rich poly(acrylic acid) (PAA). Due to the good adsorption capacity and reducibility of $Ti_3C_2T_x$ MXene for $Ag^+$ ions, no additional stabilizers or reducing agents were required for the selective detection of $Ag^+$. As the $Ag^+$ ions were reduced in situ to nanoparticles by $Ti_3C_2T_x$ MXene, the color of the solution gradually deepened to tan. The UV–Vis absorption spectra of $Ag^+$ ions, $Ti_3C_2T_x$–PAA, and Ag nanoparticle@$Ti_3C_2T_x$–PAA are shown in Fig. 9(b). The localized SPR of in situ Ag nanoparticles was excited, which considerably influenced the properties of the sensing material. Moreover, $Ti_3C_2T_x$–PAA could realize the retouch-free and visual detections of $Ag^+$ by the in situ reduction method. Figure 9(c) presents the UV–vis absorption spectra of $Ti_3C_2T_x$–PAA (12 μg/mL) reacted with different concentrations of $Ag^+$ (0–500 μM). The absorption spectrum at 450 nm of the nanoplasmonic platform based on Ag nanoparticle@$Ti_3C_2T_x$–PAA exhibited sensitivity to $Ag^+$, and the detection limit was 0.615 μM.

For the retouched assay, special probes (e.g. DNA) need to be modified on the MXene surface to achieve highly sensitive detection of specific targets. Tao et al. designed a colorimetric sensor based on MXene-probe DNA–Ag/Pt nanohybrids, where MXene was used as the supporting substrate; its surface was modified with the special probe DNA (Fig. 9(d)) [152]. $Ti_3C_2T_x$ MXene was reported to possess intrinsic peroxidase-like activity [153]; however, its catalytic ability was still weaker than those of other metal or metal oxide nanozymes. Therefore, exploring combinations of MXene with noble metal nanomaterials as enzyme mimics can help improve the catalytic performance. To achieve effective linking between MXene and noble metals, an intermediate medium (i.e., DNA) is required. Controlling changes in the sequence and structure of template DNA enables precise deposition of the specific type of metal nanoparticles to form DNA metallization structures [154–156]. Furthermore, single-stranded DNA can be efficiently adsorbed onto $Ti_3C_2T_x$ MXenes by chelating phosphate groups in the DNA with titanium ions on $Ti_3C_2T_x$ NSs [119]. DNA metallization on $Ti_3C_2T_x$ is an ideal strategy for the efficient preparation of MXene–metal nanohybrids, which can serve as effective enzyme mimics for sensitive colorimetric detection. Figure 9(d) shows the manufacturing strategy of MXene-probe DNA-Ag/Pt nanohybrid-based colorimetric sensing platform for hepatitis B virus DNA detection. The MXene-probe DNA–Ag/Pt nanohybrid was sensitive to the target hepatitis B virus DNA; the changes were visible to the naked eye (Fig. 9(e)) [152], and the detection limit was as low as 0.5 pM.

QDs, another form of MXenes with diameters of 2–5 nm (Fig. 9(f)) [135], are also a promising sensing material. $Ti_3C_2T_x$ MXene QDs can be used in fluorescence sensing technology due to their good fluorescence effect and are ideal candidates for colorimetric sensing with high sensitivity. Bai et al. modified N,P-doped $Ti_3C_2T_x$ QDs (N,P$vTi_3C_2T_x$ QDs) with the 1,10-phenanthroline-Fe (II) complex (Phen-$Fe^{2+}$) to fabricate an orange-colored colorimetric sensing platform. After reacting with nitrite ($NO_2^-$), the color of orange suspension gradually lightened and finally became colorless with the increase in $NO_2^-$ concentration [135]. Suspensions of different colors have different absorption spectra; therefore, changes in $NO_2^-$ concentration could be clearly visualized by plotting the absorbance ratio curve (Fig. 9(g)) [135]. The detection limit of the N,P-doped

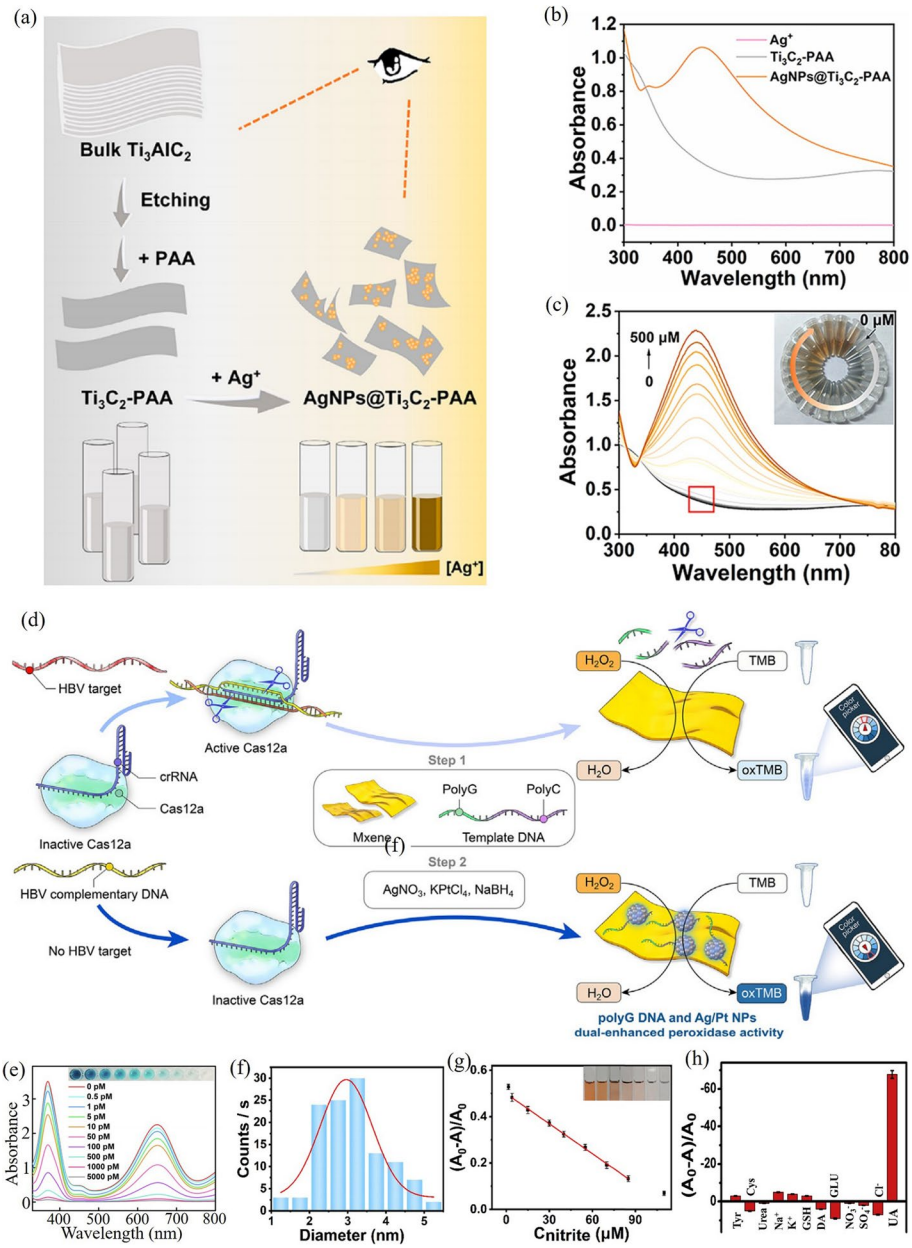


**Fig. 9** **a** Fabrication and modification of $Ti_3C_2T_x$ NSs for the detection of $Ag^+$ ions [151]. **b** UV — vis absorption spectra of $Ag^+$ ions, $Ti_3C_2T_x$ — PAA, and Ag nanoparticles@$Ti_3C_2T_x$ — PAA [151]. **c** UV — vis absorption spectra of $Ti_3C_2T_x$ — PAA reacted with different concentrations of $Ag^+$ [151]. Copyright 2020, American Chemical Society. **d** Fabrication of the $Ti_3C_2T_x$ NSs-based colorimetric sensor for hepatitis B virus DNA sensing [152]. **e** Absorption spectra of the $Ti_3C_2T_x$ NSs-based colorimetric sensor at different concentrations of target hepatitis B virus DNA [152]. Copyright 2022, Academic Press Inc. **f** The size of $Ti_3C_2T_x$ MXene QDs [135]. **g** Absorbance ratio of the N, P — $Ti_3C_2T_x$ QDs — based colorimetric sensor at different concentrations of $NO_{2-}$ (4 – 85 μM) [135]. Copyright 2022, Elsevier. **h** Absorbance ratio of the glutathione (GSH) functionalized $Ti_3C_2T_X$ QDs — based colorimetric sensor for the selective detection of uric acid [115]. Copyright 2020, Elsevier

$Ti_3C_2T_x$ MXene QD/Phen-$Fe^{2+}$-based colorimetric sensing platform toward $NO_2^-$ was 0.71 μM. Furthermore, changes in the probes of the $Ti_3C_2T_x$ MXene QDs enabled the detection of other specific analytes. For example, glutathione-functionalized $Ti_3C_2T_x$

QDs have a highly sensitive and precise selective detection ability for uric acid, with a detection limit of 200 nM (Fig. 9(h)) [115]. MXene-based colorimetric sensors have also received considerable research attention; Table 6 summarizes the related studies conducted so far.

#### Electrochemical sensors

Electrochemical sensing is a technology that converts chemical signals into electrical signals for sensing detection. It takes the electrode as the conversion element or fixed carrier, and realizes the qualitative or quantitative analysis of the target by transforming the chemical changes at the electrode interface into electrical signal parameters such as potential, conductivity, and current. In a loop circuit where the external voltage is applied, the specific recognition between the probe and the analyte near the electrode leads to charge transfer in the circuit, resulting in an electric current. The current is transmitted through the conductive system of the electrodes to the signal analysis system for amplification, forming an identifiable electrical signal. Finally, changes in the electrical signal are analyzed to track different concentrations of the analyte [161, 162]. Electrochemical sensors usually employ a three-electrode system, comprising a working electrode (WE), a counter electrode (CE), and a reference electrode (RE) (Fig. 10(a)). Modifying special materials on the surface of WE is one of the effective approaches for enhancing the sensitivity and selectivity of an electrochemical sensor. After modification, these electrode modification materials should exhibit high electron mobility, excellent biocompatibility, good hydrophilicity, and selective recognition ability. MXenes [163–165] and their modifications (Fig. 10(b)) [166–169] exhibit these characteristics, which can greatly improve the sensing performance, making them ideal materials for designing high-performance electrochemical sensors. Moreover, the electrochemical signals generated by MXene and its modifications can detect multiple targets simultaneously. For example, the accordion-like alk-$Ti_3C_2$ (Fig. 10(c)) modified electrode could detect multiple target heavy metal ions simultaneously with high sensitivity (Fig. 10(d)), with detection limits of 0.041 mM, 0.098 mM, 0.130 mM, and 0.032 mM, for $Pb^{2+}$, $Cd^{2+}$, $Hg^{2+}$, and $Cu^{2+}$, respectively [170].

**Table 6** Reports on $Ti_3C_2T_x$ MXene-based colorimetric sensors in recent years

| Materials | Analytes | Linear range | Detection limit | References |
|---|---|---|---|---|
| $Ti_3C_2T_X$ MXene — poly(acrylic acid) | $Ag^+$ | 2 — 200 μM | 0.615 μM | [151] |
| $Ti_3C_2T_x$ Mxene — probe DNA — Ag/Pt nanohybrids | Hepatitis B virus DNA | 0.5 — 1000 pM | 0.5 pM | [152] |
| $Ti_3C_2T_x$@ssDNA | Thrombin | $10^{-11}$ – $10^{-8}$ M | $10^{-11}$ M | [153] |
| MXene@NiFe-LDH Nanocatalyst | Glutathione | 0.9 – 30 μM | 84 nM | [157] |
| $Ti_3C_2T_X$ MXene NSs | $H_2O_2$ | 5.0 μM – 0.5 mM | 1 μM | [158] |
| $Ti_3C_2T_X$/CuS nanocomposites | Cholesterol | 10 – 100 μM | 1.9 μM | [159] |
| Prussian blue — $Ti_3C_2T_X$ | $H_2O_2$ | 2 – 100 μM | 0.4667 μM | [160] |
| | Dopamine | 5 — 120 μM | 3.36 μM | |
| | Glucose | 10 — 350 μM | 6.52 μM | |
| GSH — $Ti_3C_2T_X$ MXene QDs | Uric acid | 1.2 — 100 mM | 200 nM | [115] |
| N, P-doped $Ti_3C_2T_X$ MXene QDs/ Phen-$Fe^{2+}$ | $NO_2^-$ | 4 – 85 μM | 0.71 μM | [135] |

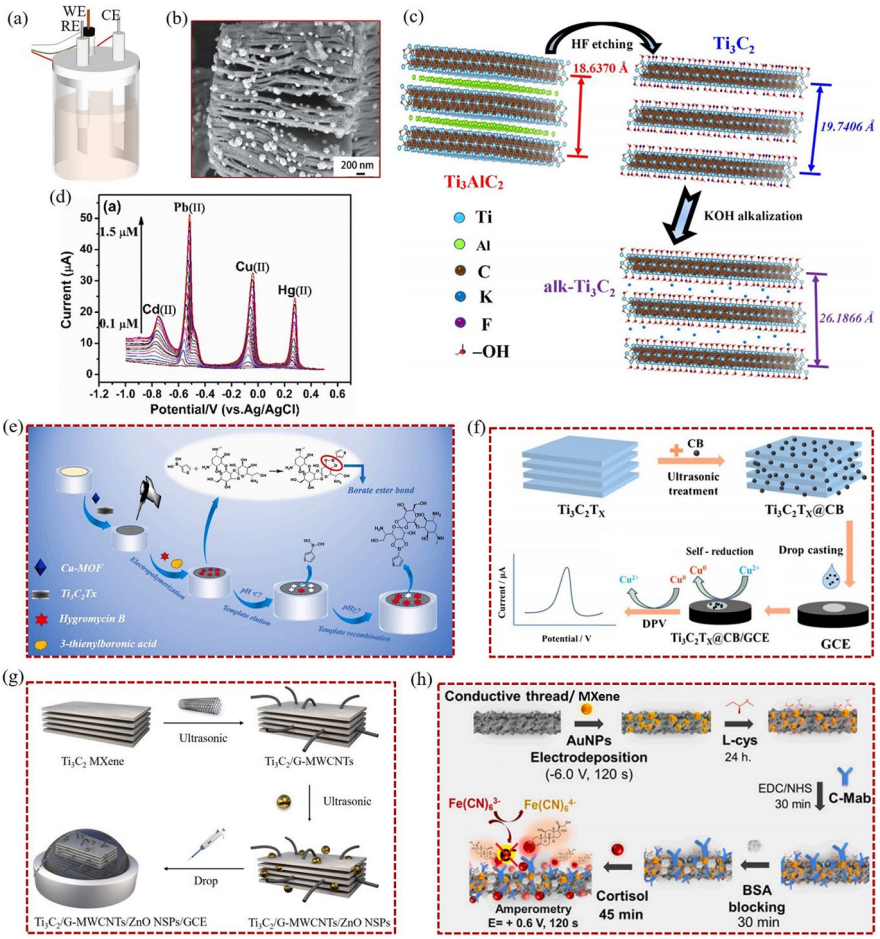


**Fig. 10** **a** Schematic of the three-electrode system. **b** SEM image of modified MXene [166]. Copyright 2021, Springer Berlin Heidelberg. **c** Alkaline treatment of MXene [170]. **d** Simultaneous detection of multiple targets by the alk- $Ti_3C_2T_x$ MXene-based electrochemical sensor [170]. Copyright 2017, Elsevier. **e** Schematic diagram of the detection of hygromycin B in food by the Cu-MOF@MXene-based electrochemical sensor [25]. Copyright 2022, Elsevier. **f** Schematic illustration of the fabrication of MXene@carbon black and its detection of $Cu^{2+}$ by electrochemical sensing technology [171]. Copyright 2021, Springer Vienna. **g** Fabrication of MXene/MWCNTs/ZnO-based glassy carbon electrode for dopamine detection [172]. Copyright 2022, Elsevier. **h** Preparation of L-cys/AuNPs/ $Ti_3C_2T_x$ composite-based electrochemical sensors for cortisol detection [173]. Copyright 2022, Elsevier

MXenes are promising candidates for electrochemical sensors and have been extensively investigated in recent years [15, 162, 174]. The application of MXenes in electrochemical sensing technology has been well summarized in relevant reviews [162, 175]. Therefore, herein, we only present a supplementary summary of a few representative recent reports. MXene-based electrochemical sensors are widely used in food safety, water source monitoring, medical diagnosis, and health monitoring due to their high sensitivity and stability. For food safety monitoring, Wang et al. reported a molecularly imprinted electrochemical sensor modified with Cu–MOF and MXene for the detection of hygromycin B (Fig. 10(e)) [25]. Cu–MOF, a material with large specific surface area, was compounded with $Ti_3C_2T_x$ MXenes, which greatly improved the performance of the molecularly imprinted electrochemical sensor. The sensor exhibited excellent selectivity

and high sensitivity to hygromycin B in food, and the detection limit was 1.92 nM. For water source monitoring, Xia et al. combined $Ti_3C_2T_x$ MXene with carbon black as an electrode material to achieve effective detection of $Cu^{2+}$ (Fig. 10(f)) [171]. $Cu^{2+}$ is a relatively common heavy metal ion in water sources, and its excessive intake can damage human body functions. Therefore, the development of reliable $Cu^{2+}$ detection methods is crucial for risk assessment. In this MXene@carbon black-based electrochemical sensor, carbon black could prevent the aggregation of MXene NSs and enhance the electron transfer rate. The detection limit for $Cu^{2+}$ was 4.6 nM in a wide linear range of 0.01–15.0 μM. For medical diagnosis, Ni et al. fabricated a composite containing MXene, multi-walled carbon nanotubes (MWCNTs), and ZnO nanospheres, which were modified on a glassy carbon electrode to enable highly sensitive (S = 16 A/M) detection of dopamine (Fig. 10(g)) [172]. Effective monitoring of dopamine concentrations in humans can enable the diagnosis of many diseases, such as Parkinson's disease, schizophrenia, and Alzheimer's disease. The MXene/MWCNT/ZnO-based electrochemical sensor exhibited precise dopamine capture capability with a detection limit of 3.2 nM in the linear range of 0.01–30 μM. For health monitoring, Laochai et al. modified anti-cortisol on a L-cys/AuNP/$Ti_3C_2T_x$ composite to design an electrochemical sensor for detecting cortisol in sweat (Fig. 10(h)) [173]. Cortisol is a steroid hormone produced by the adrenal glands, and it affects various physiological processes in the human body; thus, detecting cortisol in sweat can enable effective monitoring of human health. Utilizing the L-cys/AuNP/$Ti_3C_2T_x$ composite-based electrochemical sensor, cortisol in sweat was detected with high sensitivity, and the detection limit was 0.54 ng $mL^{-1}$. In addition to the aforementioned MXene-based electrochemical sensors, there have been several exciting related reports, some of which are summarized in Table 7.

#### Temperature sensors

Temperature measurement is crucial for human life and production. Strict temperature control is required for medical diagnosis, scientific research, or industrial production. As an emerging 2D transition metal carbide material, MXenes have attracted attention due to their excellent thermoelectric properties, high electrical conductivity, and good water dispersibility [74, 201]. $Ti_{n+1}C_nT_x$ MXenes and their related composites exhibit excellent electro-thermal and photo-thermal conversion behavior, which is conducive to designing temperature sensors [17, 73, 202]. Xuan et al. irradiated a low-concentration MXene solution with an 808 nm laser and found that the temperature increased from room temperature to > 60° within 300 s, whereas for pure water, the temperature change was negligible [38]. Luo et al. decorated $Ti_3C_2T_x$ MXene on textile to fabricate a temperature sensor, and tested its photo-thermal behavior using a xenon lamp (Fig. 11(a)) [202]. The MXene exhibited a strong photo-thermal effect. Under the irradiation of the xenon lamp, the temperature increased rapidly and reached a saturation temperature of ~ 59 °C after 300 s. When the xenon lamp was turned on and off, the temperature curve showed periodic changes, and the changing trend was consistent, indicating that the photothermal conversion of MXene exhibited good repeatability (Fig. 11(b)) [202]. During the heating and cooling process, the temperature of MXene changed, and its relative resistance also changed (Fig. 11(c)) [202]. Therefore, changes in temperature can be monitored by measuring the relative resistance of MXene.

**Table 7** Partial electrochemical sensors based on MXene

| Materials | Method | Target | Detection limit | Linear range | Refs |
|---|---|---|---|---|---|
| Platinum nanoparticles/ $Ti_3C_2T_x$ | Cyclic voltammetry | Bisphenol A | 32 nM | 50 nM – 5 μM | [176] |
| Au NPs/ $Ti_3C_2T_x$-PDDA | Amperometry | Nitrite | 0.059 μM | 0.1–2490 μM and 2490–13,500 μM | [177] |
| ZnO/$Ti_3C_2T_x$/ Nafion/Au | Cyclic voltammetry | Dopamine | 0.076 μM | 0.1 – 1200 μM | [178] |
| $Ti_3C_2T_x$ /GCE | Differential pulse voltammetry | $BrO_3^-$ | 41 nM | 50 nM – 5 M | [179] |
| Prussian blue@ $Ti_3C_2T_x$ | Differential pulse voltammetry | Malathion | $1.3 \times 10^{-16}$ M | 0.0001 — 1.0 nM | [160] |
| $Ti_3C_2$-MXene/BP | Linear Sweep Voltammetry | Naphthalene Acetic acid | 1.6 nM | 0.02 – 40 μM | [180] |
| $Ti_3C_2$ /MWCNTs | Differential pulse voltammetry | Hydroquinone | 6.6 nM | 2 – 150 μM | [181] |
| | | Catechol | 3.9 nM | | |
| MXene/SPE | Differential pulse voltammetry | Acetaminophen | 0.048 μM | 0.25 – 2000 μM | [174] |
| | | Isoniazid | 0.064 mM | 0.1 – 4.6 mM | |
| Bismuth/MXene | Stripping voltammetry | $Pb^{2+}$ | 10.8 nM | 0 –0.6 μM | [182] |
| Nano-Composite | | $Cd^{2+}$ | 12.4 nM | | |
| GC/$Ti_3C_2$ — HF/TBA/ GOx/GTA | Cyclic voltammograms | Glucose | 23.0 μM | 50 — 250 μM | [183] |
| $Ti_3C_2T_x$ /Pt nanoparticles | Cyclic voltammetry | $H_2O_2$ | 0.448 μM | 490 μM — 53.6 mM | [184] |
| $Ti_3C_2T_x$@CB/GCE | Differential pulse voltammetry | $Cu^{2+}$ | 4.6 nM | 0.01–15.0 μM | [171] |
| Alk-$Ti_3C_2$/GCE | Square wave anodic stripping voltammetry | Cd(II) | 0.098 μM | 0.1–1.5 μM | [170] |
| | | Pb(II) | 0.041 μM | | |
| | | Cu(II) | 0.032 μM | | |
| | | Hg(II) | 0.13 μM | | |
| Au- $Ti_3C_2T_x$ | Sandwich-type electrochemical immunoassay | CYFRA21-1 | 0.1 pg·mL$^{-1}$ | 0.5– $1.0 \times 10^4$ pg·mL$^{-1}$ | [166] |
| $Ti_3C_2T_x$-$Fe_2O_3$ composite | Cyclic voltammetry | $H_2O_2$ | 7.46 nM | 10 nM – 1 μM | [185] |
| $Ti_3C_2$/G-MWCNTs/ ZnO/GCE | Differential pulse voltammetry | Dopamine | 3.2 nM | 0.01–30 μM | [172] |
| Au@Carbon QDs-MXene | Differential pulse voltammetry | Nitrite | 0.078 μM | 1 – 3200 μM | [186] |
| Cu-MOF/$Ti_3C_2T_x$ | Cyclic voltammetry | Hygromycin B | $1.92 \times 10^{-9}$ M | $5 \times 10^{-9}$ – $5 \times 10^{-6}$ M | [25] |
| Glucose Oxidase/ PEDOT:4-Sulfocalix [4]arene/MXene Composite | Cyclic voltammetry | Glucose | 0.0225 mM | 0.5 – 8 mM | [187] |
| rGO/MXene-Pd/rGO | Differential pulse voltammetry | Luteolin | $2.0 \times 10^{-10}$ M | $6 \times 10^{-10}$ – $8 \times 10^{-7}$ M and $1 \times 10^{-6}$ – $1 \times 10^{-5}$ M | [188] |
| Ce-MOF/$Ti_3C_2T_x$ | Differential pulse voltammetry | L-Tryptophan | 0.19 μM | 0.2 – 139 μM | [189] |
| N-$Ti_3C_2$/PC composite | Differential pulse voltammetry | Acetaminophen | 0.050 μM | 1–150 μM | [190] |
| | | 4-aminophenol | 0.059 μM | | |
| CNT/$Cu_2O$ NPs/ $Ti_3C_2T_x$ | Differential pulse voltammetry | Diethylstilbestrol | 6 nM | 0.01 – 70 μM | [191] |
| Ni embedded $Ti_3C_2T_x$ composites | Differential pulse voltammetry | Methylmalonic acid | 0.12 pM | 0.001 – 0.017 μM | [192] |

**Table 7** (continued)

| Materials | Method | Target | Detection limit | Linear range | Refs |
|---|---|---|---|---|---|
| L-cys/AuNPs/MXene | Cyclic voltammetry | Antigen–antibody | 0.54 ng $mL^{-1}$ | 5–180 ng $mL^{-1}$ | [173] |
| $Ti_3C_2T_x$ MXene/graphene composite | Differential pulse voltammetry | *p*-nitrophenol | 0.16 μM | 1 – 175 μM | [193] |
| $Ti_3C_2T_x$-$TiO_2$/$NiWO_4$ | photo-electrochemical | Prostate-specific antigens | 0.15 fg.$mL^{-1}$ | 1.2 fg.$mL^{-1}$ – 0.18 mg.$mL^{-1}$ | [194] |
| MXenes/Apt2/exosomes/Apt1/PNIPAM-AuNPs/GCE | Electro-generated chemiluminescence | MCF-7 Exosomes | 125 Particles/L | $5 \times 10^2$ –$5 \times 10^6$ Particles/L | [195] |
| MIP-MXene/$NH_2$-CNTs/GCE | Differential pulse voltammetry | Fisetin | 1 nM | 0.003–20.0 μM | [196] |
| Alk-$Ti_3C_2$/N-PC | Differential pulse voltammetry | Hydroquinone | 4.8 nM | 0.5–150 μM | [197] |
| | | Catechol | 3.1 nM | | |
| MXene/CNHs/β-CD-MOFs | Differential pulse voltammetry | Carbendazim pesticide | 1 nM | 3.0 nM – 10.0 μM | [198] |
| PB-MXene-Apt/Apt/PAMAM-Au NPs/GCE | Square-wave pulse voltammetry | Exosomes | 229 particles $\mu L^{-1}$ | $5 \times 10^2$ particles $\mu L^{-1} - 5 \times 10^5$ particles $\mu L^{-1}$ | [199] |
| $Ti_3C_2T_x$@FePcQDs hybrid | Electrochemical impedance spectroscopy | miRNA-155 | 4.3 aM | 0.01 fM – 10 pM | [200] |

MXenes also exhibit an excellent electrothermal conversion effect, which can rapidly increase the temperature by additional input voltage. The joule heating capability of MXenes was evaluated by measuring the change in temperature with time (Fig. 11(d)) [203]. According to Joule's law, the temperature increased gradually with the increase in input voltage, and it was almost proportional to the square of the input voltage. Figure 11(e) shows the durable and reproducible thermal response of the MXene specimen [203]. When a voltage of 3 V was cycled on and off for 20 cycles, the temperature of the MXene samples could be rapidly increased and decreased, and the maximum temperature value could be maintained at 45 °C. The excellent photothermal conversion and electrothermal conversion behaviors of MXenes indicate that they have a good temperature sensing function. Under different temperature environments, the relative resistance of MXenes shows significant responses (Fig. 11(f)) [204]. To improve the temperature resistance and flame resistance of MXenes, Wang et al. coated MXene NSs with carboxymethyl chitosan (CCS) and deposited it on cotton fabric (CF) to prepare a flame-resistant, temperature-sensitive sensing material, labeled as MXene/CCS@CF (Fig. 11(g)) [205]. The linear voltage-current curve (Fig. 11(h)) indicates the stability of the operating voltage and current, confirming the reliability of the MXene/CCS@CF heater. The temperature of the MXene/CCS@CF is controlled by switching the input voltage on and off, demonstrating the controllability of the joule heating performance (Fig. 11(i)) [205]. In a short period of time, the temperature of MXene/CCS@CF increases rapidly under the influence of the input voltage. Rapid heating of the MXene/CCS@CF was achieved in approximately 30 s with excellent repeatability (Fig. 11(j)) [205]. The sensitive photothermal and electrothermal conversion capabilities of MXenes and their modifications indicate that they are promising candidates for the development of temperature sensors.

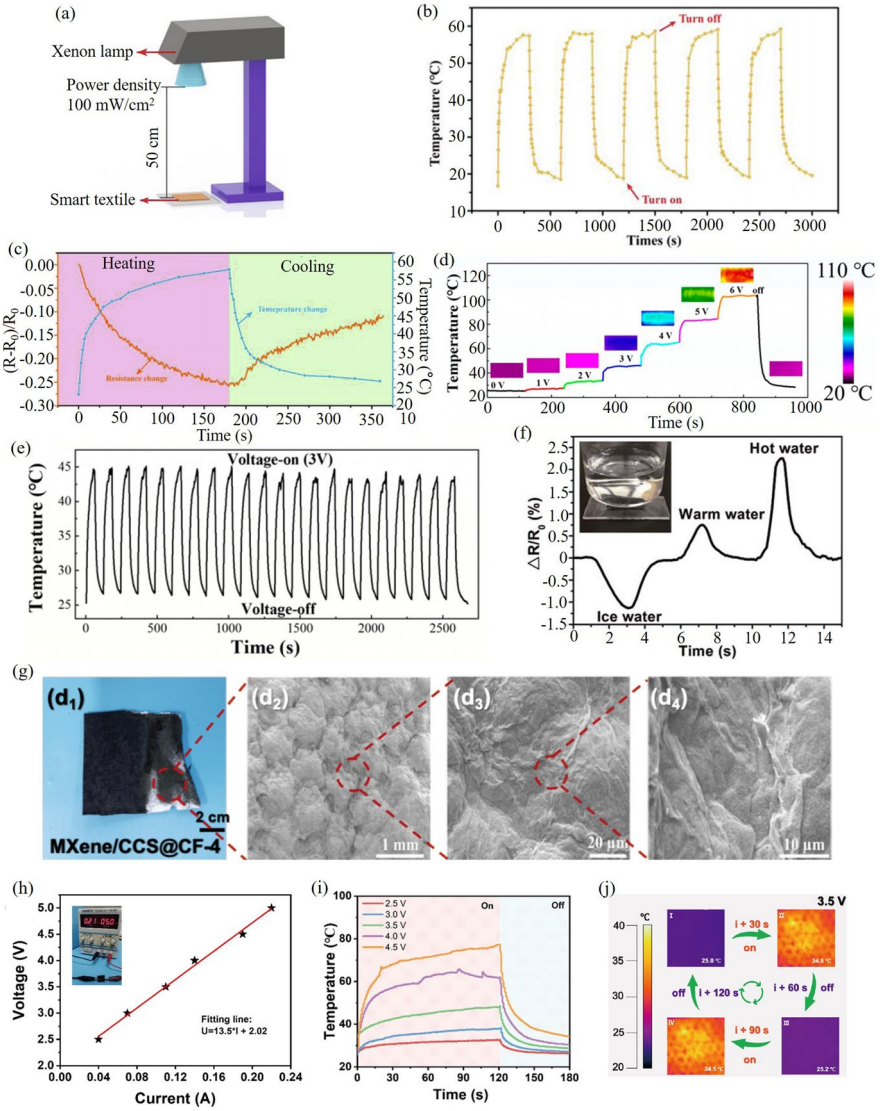


**Fig. 11** **a** Schematic diagram of photothermal testing of MXene sample under a xenon lamp [202]. **b** Temperature changes of MXene sample with the xenon lamp on and off (power density = 100 mW/cm$^2$) [202]. **c** Changes in temperature and relative resistance during heating and cooling of MXene sample [202]. Copyright 2021, Elsevier. **d** Real-time changes in temperature under different input voltages [203]. **e** Stable changes in temperature when the input voltage is repeatedly turned on and off [203]. Copyright 2020, American Chemical Society. **f** The relative resistance of MXene sample changes under different temperature environments [204]. Copyright 2019, Royal Society of Chemistry. **g** SEM images of the MXene/CCS@CF [205]. **h** Voltage-current curve of the MXene/CCS@CF [205]. **i** Real-time temperature changes of MXene/CCS@CF with different input voltages [205]. **j** Infrared camera images of MXene/CCS@CF after heating and cooling [205]. Copyright 2021, American Chemical Society

### Humidity sensors

Humidity is an important environmental parameter that is closely related to human production and life. Humidity sensors can rapidly and accurately sense the changes in humidity in the environment and then convert this information into electrical or optical signals that can be easier for humans to observe. To meet the needs of different application scenarios and measure humidity in different environments, different types of

humidity sensors are used that can be divided into resistive and capacitive types according to their outputs. As a hydrophilic material, MXene is rich in surface functional groups, which can interact with the moisture in the environment and realize effective humidity detection. Some oxygen groups (epoxy and hydroxyl functional groups) demonstrated by MXene NSs can trap or release water molecules with the aid of H bonds, as shown in Fig. 12(a) [206]. When a multilayer MXene absorbs a certain amount of water molecules, the surface properties are changed and the interlayer spacing is widened (Fig. 12(b)) [207]. These changes greatly affect the electronic properties of the MXene materials. Therefore, by monitoring the changes in the resistance signal of the MXene, the change of the environmental humidity can be intuitively observed (Fig. 12(c)) [207]. Wang et al. deposited MXene on a spring-like helical core-sheath polyester yarn to form a flexible sensing structure (Fig. 12(d)) [206]. This flexible sensor was extremely sensitive to the humidity of the environment and could effectively detect relative humidity (RH) from 30 to 100% with a sensitivity of 0.157 kΩ/RH% (Fig. 12(e)) [206]. The effects of humidification and drying on resistance are shown in Fig. 12(f) [206], which demonstrate the recoverability of the sensing performance and the reusability of the structure.

To enhance the sensitivity of the humidity sensor, some other MXene-derived novel materials have been synthesized with stronger absorption ability of water molecules, such as $Ti_3C_2T_x$ MXene/$K_2Ti_4O_9$ composites, urchin-like $Ti_3C_2T_x$/$TiO_2$ composites, and alkalized $Ti_3C_2T_x$. Wu et al. used KOH to treat sheet-like $Ti_3C_2T_x$ (S–$Ti_3C_2T_x$) for 48 h at 30 °C and then fabricated an S–$Ti_3C_2T_x$ MXene/$K_2Ti_4O_9$ composite (Fig. 12(g)) [208]. In the composite, $K_2Ti_4O_9$, a hydrophilic material that enhances water absorption, exhibited filament-like nanostructures with narrow widths of 10–50 nm and was wound on the surface of S–$Ti_3C_2T_x$ MXene. The enlargement of the interlayer distance of the S–$Ti_3C_2T_x$ caused by the intercalated $K^+$ increased the intake of water molecules. Owing to these two advantages, the S–$Ti_3C_2T_x$ MXene/$K_2Ti_4O_9$ composite-based sensor exhibited stronger humidity sensitivity (Fig. 12(h)) [208]. The RH response of the S–$Ti_3C_2T_x$ MXene/$K_2Ti_4O_9$ composite was more than 8 times higher than that of the accordion-like $Ti_3C_2T_x$ (Fig. 12(i)) [208]. Li et al. used varied reaction conditions of MXene in KOH to develop a novel $Ti_3C_2T_x$/$TiO_2$ composite. In the synthesis method, 100 mg of $Ti_3C_2T_x$ MXene was poured into 60 mL KOH (12 mol/L) and they were allowed at 50 °C for 10 h (Fig. 12(j)) [209]. The as-prepared $Ti_3C_2T_x$/$TiO_2$ composite had a strong humidity sensing ability, and it was used to develop a humidity sensor. The $Ti_3C_2T_x$/$TiO_2$ composite-based humidity sensor had high sensitivity (280 pF/%RH) in a low-RH environment (Fig. 12(k)) [209]. Instead of KOH, Yang et al. treated MXene with NaOH at room temperature for 2 h, and finally prepared the alkalized $Ti_3C_2T_x$ MXene [67]. The $Na^+$ insertion and increased surface terminal oxygen–fluorine ratio in $Ti_3C_2T_x$ MXene effectively enhanced the humidity sensing ability. Compared with the pristine $Ti_3C_2T_x$ MXene, the alkalized $Ti_3C_2T_x$ exhibited stronger resistance changes under different ambient humidity conditions (Fig. 12(l)) [67]. Figure 12(m) and (n) show the resistance responses ($R/R_{11\%}$) of pristine $Ti_3C_2T_x$ and alkalized $Ti_3C_2T_x$, respectively, to different humidity conditions [67]. The resistance response showed a trend of enhancement with the increase in RH, and the response value of alkalized $Ti_3C_2T_x$ was greatly improved. In general, MXene and its derivatives show excellent application potential in humidity sensing,

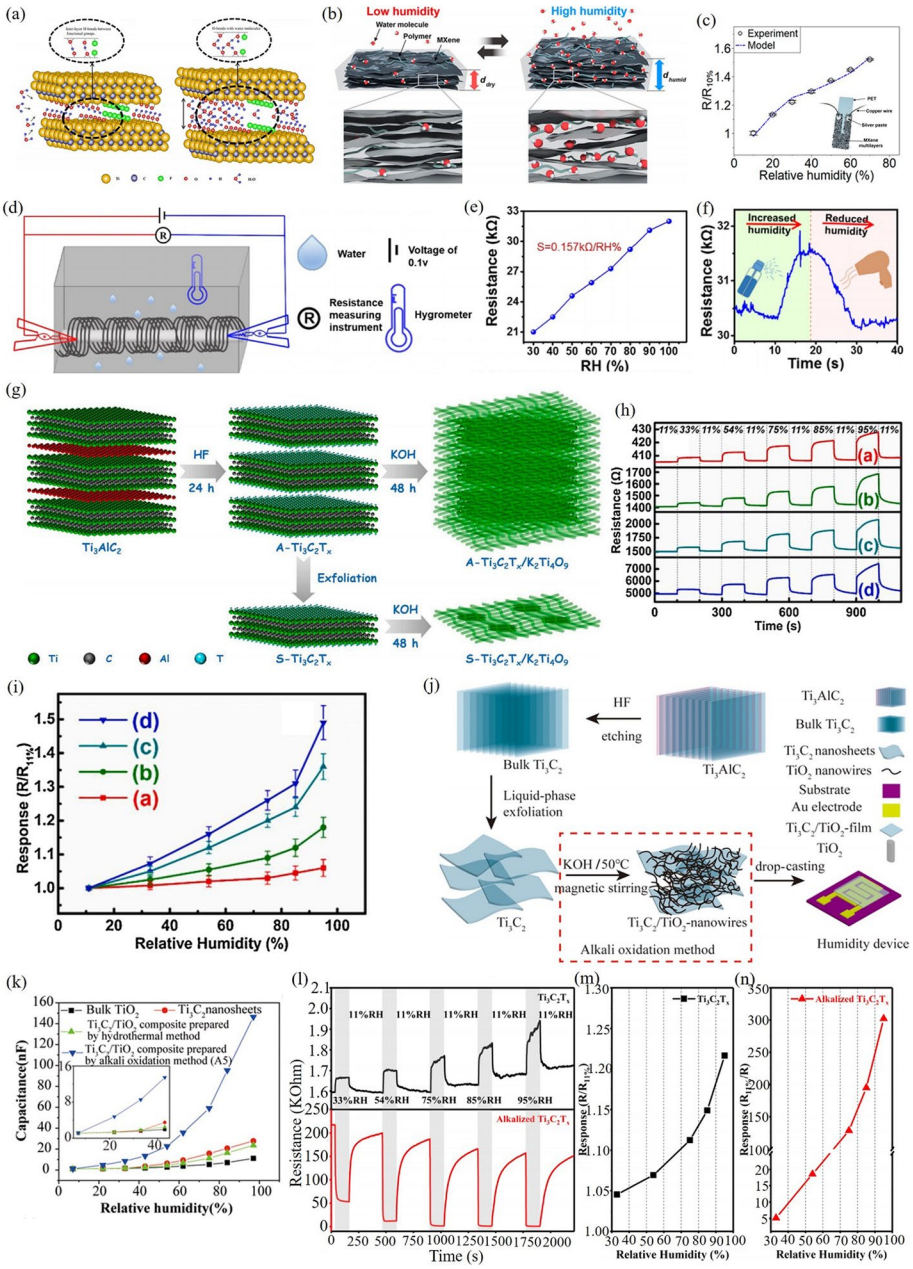


**Fig. 12** **a** Schematic diagram of atomic structure of multilayer MXene before and after water absorption [206]. Copyright 2020, Springer US. b Structural changes of MXene materials in low-humidity and high-humidity environments [207]. **c** Variation of resistance of MXene materials in different humidity environments [207]. Copyright 2019, American Chemical Society. **d** Spring-like helical core-sheath polyester yarn-based flexible MXene sensing structure [206]. **e** Variation of resistance with respect to the RH for the flexible MXene sensor [206]. **f** The effects of humidification and drying on resistance, which demonstrate the recoverability of the sensing performance and the reusability of the structure [206]. Copyright 2020, Springer US. **g** Schematic diagram of the synthesis of S- $Ti_3C_2T_x$ MXene $K_2Ti_4O_9$ composite [208]. **h** Variation of resistance with different RH [208]. **i** Response comparison of different humidity [208]. Copyright 2021, Elsevier. **j** The synthesis process of $Ti_3C_2T_x/TiO_2$ composite [209]. **k** Variation of capacitance of $Ti_3C_2T_x/TiO_2$ composite at different relative humidity [209]. Copyright 2021, Royal Society of Chemistry. **l** Dynamic response-recovery curve of resistance for the pristine $Ti_3C_2T_x$ and alkalized $Ti_3C_2T_x$ under different RH [67]. **m**, **n** Resistance responses (R/R11%) of pristine $Ti_3C_2T_x$ and alkalized $Ti_3C_2T_x$ under different RH [67]. Copyright 2019, American Chemical Society

indicating that they may be used in the development of intelligent devices and bionic technologies.

#### Pressure/strain sensors

Strain sensors are flexible electronic devices that can convert strain into electrical signals for easy collection and transmission, enabling accurate record-keeping of the deformations of the target in real time. High-performance flexible strain sensors should exhibit high sensitivity, stretchability, flexibility, durability, and low power consumption [210–213]. $Ti_{n+1}C_nT_x$ MXenes possess excellent electrical conductivity, good hydrophilicity, and outstanding mechanical properties, which can be developed as ideal conductive force-sensitive materials for flexible strain sensors [214–216]. In strain sensing, there are four main factors that cause strain, namely, pressure, tension, bending, and torsion. These strain modes can change the electrical properties of the force-sensitive material, converting the strain signal into an electrical signal. Therefore, effective detection of various strain forces can be realized by monitoring changes in electrical signals. Herein, we summarize and discuss the sensing detection of four strain forces by MXene materials.

$Ti_{n+1}C_nT_x$ is essentially a ceramic phase material and has some brittleness; therefore, the piezoresistive sensor assembled from pure MXene materials cannot withstand high pressure and thus easily breaks or collapses. Therefore, MXene materials should be compounded with some highly flexible materials to meet the mechanical strength requirements of pressure sensing. The internal structure of MXene-based sensing composites deforms when subjected to pressure, resulting in a fluctuation in carrier mobility, that is, the piezoresistive effect. The composition of piezoresistive sensors with MXenes as the sensitive material is shown in Fig. 13(a) [217]. First, the conductive MXene/CF hybrid material was fabricated using CF as the flexible carrier to support force-sensitive MXene materials. Second, the conductive fabric was covered on a polyimide (PI) substrate plated with interdigital electrodes. Finally, the polydimethylsiloxane (PDM) film was coated on the conductive fabric as an encapsulation layer, thus completing the fabrication of the MXene-based piezoresistive sensor. The resistance of the MXene-based piezoresistive sensor was measured, and the results demonstrated that the resistance decreased significantly from 1946 Ω to 168 Ω when the MXene concentration increased from 0.1 mg/mL to 0.4 mg/mL. With further increase in the concentration, the resistance of the pressure sensor stabilized at 134.2 Ω (Fig. 13(b)) [217]. Therefore, when MXene concentration exceeds a certain threshold, the resistance tends to be stable, avoiding the impact of concentration on the detection function of the sensor.

Figure 13(c) illustrates the strain process of the sensing structure under external pressure [218]. When an external force is applied to the piezoresistive sensor, the sensitive material deforms, increasing the effective contact area between the MXene composite and the electrode, thereby increasing the conductive path, which eventually increases the current (Fig. 13(d)) and decreases the resistance. The MXene-based piezoresistive sensor has a sensitivity of 164.93 $k{\cdot}Pa^{-1}$ in the range of 0–10 kPa and 403.46 $k{\cdot}Pa^{-1}$ in the range of 10–18 kPa (Fig. 13(e)) [218]. Recently, Shi et al. reported a method for the fabrication of soft polysiloxane crosslinked MXene aerogel, labeled as BBP–MX–AG [219]. The BBP–MX–AG has a retractable nanochannel structure with multi-level

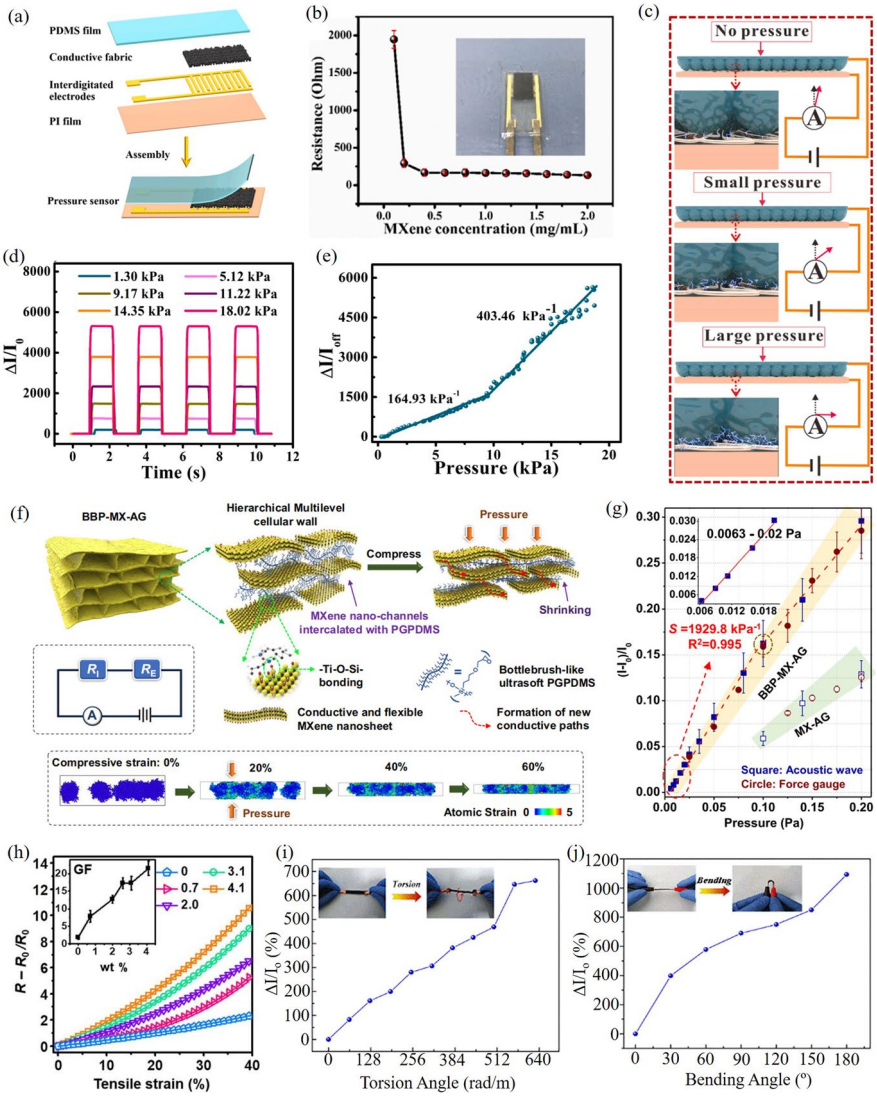


**Fig. 13** **a** Schematic illustrations of the MXene-based piezoresistive sensor [217]. **b** Variation of the resistance with respect to the concentration of the MXene [217]. Copyright 2021, Elsevier. **c** Schematic diagram of MXene-based sensing circuit [218]. **d** The current change of the piezoresistive sensor under different pressure [218]. **e** The sensitivity of the MXene-based piezoresistive sensor [218]. Copyright 2022, Elsevier. **f** Schematic illustration of BBP-MX-AG-based piezoresistive sensor [219]. **g** Pressure sensitivity of the piezoresistive sensor under different pressure stimuli [219]. Copyright 2022, Springer Nature. **h** Variation of relative resistance with respect to the tensile strain [220]. Copyright 2018, American Association for the Advancement of Science. **i** Variation of relative current with respect to the torsion angle [221]. **j** Variation of relative current with respect to the bending angle [221]. Copyright 2021, Elsevier

cellular walls inside (Fig. 13(f)). The synergistic effect of easily shrinkable nanopores and sensitive materials conferred a pressure-sensitive aerogel an ultra-low Young's modulus (140 Pa), rich conductive network, and mechanical stability. The fabricated BBP–MX–AG is an extremely sensitive piezoresistive sensor with extremely low detection limit (0.0063 Pa), fast response time (millisecond level), and high sensitivity (1929.8 k·Pa$^{-1}$) (Fig. 13(g)) [219]. This flexible strain sensor also exhibited excellent durability, and it could quickly return to its original shape after being subjected to external force without

undergoing physical damage, and the electrical stability was not affected. BBP–MX–AG-based sensor is one of the highly sensitive biosensors reported in contemporary literature, and it can be considered a leading achievement in piezoelectric sensors. In addition to being sensitive to pressure, MXene-based flexible strain sensors are also sensitive to other strain-generating factors, such as tension (Fig. 13(h)) [220], torsion (Fig. 13(i)) [221], and bending (Fig. 13(j)) [221]. Whether tension, torsion, or bending, the morphology of the MXene-based strain sensing film changes, resulting in changes in its electrical properties, and it can ultimately be used to sense various strain forces by monitoring changes in current or resistance. In the past few years, MXene-based strain sensors have been extensively studied, and various high-performance sensing structures have been reported. In Table 8, we list and summarize the main performance indicators of MXene-based strain sensors from the past two years, while earlier related reports have been well summarized in other reviews [222–224].

#### MXene-based sensing technology for wearable smart device

In recent years, with advances in flexible electronics, wearable smart devices have attracted extensive research attention. Wearable smart sensors can convert the strain, temperature, and humidity changes of the human body into electrical signals and output them on various devices. Weaving or assembling the wearable smart sensors on clothing or skin can enable monitoring of human physiological information in real time, such as movement status, skin temperature, humidity, and blood pressure. In the previous section, we summarized and discussed the application of $Ti_{n+1}C_nT_x$ materials in various sensors, which indicates that MXene and its composites are highly sensitive to changes in strain, temperature, and pressure, showing that MXenes are suitable for designing flexible wearable smart devices. However, MXenes are a ceramic phase material, and exhibiting some brittleness and poor self-straining ability; thus, high-performance and high-flexibility wearable devices should combine MXenes with textiles, hydrogels, aerogels, and so on. The fabrication methods include dip coating, spray drying, freeze–drying, electrospinning, wet spinning, and vacuum filtration [23, 201, 280–282].

The frequency of breathing is generally proportional to the heart rate. When the heart beats faster, the breathing rate increases. Therefore, by monitoring breathing, the health status of humans in terms of movement, disease, or weakness can be monitored. MXenes are a highly humidity-sensitive material that can be developed into a wearable device for respiratory monitoring [203, 283, 284]. Recently Xing et al. proposed a wearable breathing sensor based on a $Ti_3C_2T_x$ and MWCNTs (MXene/MWCNT) composite electronic fabric (Fig. 14(a)) [284]. The sensor had a 265% resistance response at 90% RH and a large stable response under deformation conditions. Furthermore, the humidity response change of the MXene/MWCNT fabric-based sensor under stretching is only 7%, which is a substantial improvement in stability compared with the pure MXene fabric sensor (35% humidity response change under stretching). Integrating the MXene/MWCNT fabric-based sensor into a mask leads to the formation of a wearable breathing monitor that can accurately identify different breathing states (Fig. 14(b)) [284]. MXene-based wearable sensors are sensitive to not only humidity but also temperature, and they can be used for smart thermotherapy and wound dressing (Fig. 14(c)) [203]. Zhao et al. deposited 2D $Ti_3C_2T_x$ NSs onto cellulose fiber nonwovens to fabricate a multifunctional

**Table 8** Performance summary of recently reported MXene-based pressure/strain sensors

| Materials | Pressure Sensitivity (S)/ Gauge factor (GF) | Linear range | Detection limit | Year | Refs |
|---|---|---|---|---|---|
| Soft polysiloxane crosslinked MXene aerogel | $S > 1900\ kPa^{-1}$ | 0.0063 – 0.1 Pa | 0.0063 Pa | 2022 | [219] |
| Hydrogel/Mxene | GF = 14.5 | 500 – 1000% | – | 2022 | [225] |
| MXene/bacterial cellulose film | $S = 51.14\ kPa^{-1}$ | 0 — 0.82 kPa | – | 2022 | [226] |
| $Ti_3C_2T_x$ MXene | $S = 62\ kPa^{-1}$ | 0 — 1.25 Pa | 0.1 Pa | 2022 | [227] |
| MXene–polydimethylsiloxane hybrid film | $S = 403.46\ kPa^{-1}$ | 10 – 18 kPa | 0.88 Pa | 2022 | [218] |
| PDMS/CNT@MXene sponge | GF = 1939 | 85 – 105% | – | 2022 | [228] |
| MXene-polyurethane/ polydimethylsiloxane | – | 0 – 90% | < 0.005% | 2022 | [229] |
| MXene@polydimethylsiloxane | $S = 2.6\ kPa^{-1}$ | 0 – 30 kPa | – | 2022 | [230] |
| MXene@polyester fabric | GF = 61.2 | 1 – 6% | – | 2022 | [231] |
| MXene/FeCo@C decorated carbon cloth | $S = 0.39\ kPa^{-1}$ | 20 – 50 kPa | – | 2022 | [232] |
| MXene/ZIF-67/polyacrylonitrile | $S = 62.8\ kPa^{-1}$ | 0 – 10 kPa | – | 2022 | [233] |
| Crumpled MXene film | S = 2.35 V/kPa | 0.3 – 1 kPa | – | 2022 | [234] |
| PAM/SA/MXene hydrogel | GF = 1.4 | 100 – 2000% | – | 2022 | [235] |
| MXene/spacer fabric | $S = 508.79\ kPa^{-1}$ | 1 – 5 kPa | – | 2022 | [236] |
| MXene-embedded nanocomposite hydrogels | $S = 100.4\ kPa^{-1}$ | 0 – 10 kPa | – | 2022 | [237] |
| Polyurethane/ polydopamine/ MXene conductive composite foam | GF = 2.36 | 2.5 – 20% | – | 2022 | [238] |
| $Ti_3C_2$/ CNCs/ WPU | GF = 868 | 0 – 5% | – | 2022 | [239] |
| Modified $Ti_3C_2T_x$-based organohydrogels | GF = 2.2 | 700 – 1000% | – | 2022 | [240] |
| MXene/polyvinyl alcohol | $S = 2320.9\ kPa^{-1}$ | 65.3 Pa – 6.53 kPa | 6 Pa | 2022 | [241] |
| polydopamine-modified MXene/CNT | GF = 9.25 | 60 – 100% | – | 2022 | [242] |
| Gluten/MXene composite organohydrogels | GF = 3.2 | 0 – 300% | – | 2022 | [243] |
| MXene/polyampholytes hydrogel | GF = 6.31 | 200 – 1000% | – | 2022 | [244] |
| PAA/PAM/MXene/TA hydrogel | GF = 10.536 | 150– 250% | – | 2022 | [245] |
| MXene/carbon nanotubes | GF = 9022 | 190 – 210% | – | 2022 | [246] |
| Mussel-Inspired Polynorepinephrine/MXene | GF = 16.9 | 0 – 0.2% | – | 2022 | [247] |
| SnS/ $Ti_3C_2T_x$ (MXene) nanohybrid | $S = 7.49\ kPa^{-1}$ and GF = 7.41 | 1.5 – 3.2 kPa and 5 – 25% | – | 2022 | [248] |
| Graphene/MXene Composite Aerogels reinforced by polyimide | GF = 3.249 | 0.2 — 4% | 0.2% | 2022 | [249] |
| 3D porous polyurethane sponge coated with MXene and carbon nanotubes composites | GF = — 4.43 | 6 – 17% | – | 2022 | [250] |
| MXene/TMD nanohybrid | $S = 14.959\ kPa^{-1}$ and GF = 14.108 | 1.477–3.456 kPa and 5–25% | – | 2022 | [251] |

**Table 8** (continued)

| Materials | Pressure Sensitivity (S)/ Gauge factor (GF) | Linear range | Detection limit | Year | Refs |
|---|---|---|---|---|---|
| MXene coated-paper and polyethylene | GF = 13.89 | -0.4 – 0% | – | 2022 | [252] |
| Ni/MXene decorated polyurethane sponge composite | GF = 13.13 | 0 – 40% | – | 2022 | [253] |
| GnP@MXene nanohybrid | GF = 400 | 100 – 350% | 0.25% | 2022 | [254] |
| Modified MXene-doped conductive organosilicon elastomer | GF = 3.9543 | 0 – 300% | – | 2022 | [255] |
| PNAGA/MXene hydrogel | GF = 2.05 | 0 – 125% | – | 2022 | [256] |
| MXene/ silver nanowire | GF = 32,122.4 | 87 – 96% | – | 2022 | [257] |
| Wrinkle-structured MXene film | S = 860 $kPa^{-1}$ | 0.5 Pa – 30 kPa | – | 2022 | [258] |
| MXene-reinforced durable cotton fabrics | S = 12.23 $kPa^{-1}$ | 0 – 13 kPa | – | 2021 | [221] |
| Superhydrophobic microcracked conductive $Ti_3C_2T_x$ MXene/paper | GF = 17.4 | 0 – 0.6% | 0.1% strain | 2021 | [214] |
| TPU/MWCNTs@MXene | GF = 363 | 80 — 101% | – | 2021 | [212] |
| Conductive MXene/cotton fabric | S = 5.30 $kPa^{-1}$ | 0 – 1.30 kPa | – | 2021 | [217] |
| $Ti_3C_2T_x$@PU foam | S = 34.24 $kPa^{-1}$ and GF = 323.59 | 1.477 – 3.185 kPa and 5 – 20% | – | 2021 | [259] |
| MXene–PU–PVA | S = 0.45% $deg^{-1}$ | 30 – 80 deg | – | 2021 | [260] |
| MXene quantum dot/ watermelon peel aerogels | S = 323 $kPa^{-1}$ | 0 – 0.4 kPa | 0.4 Pa | 2021 | [261] |
| $Ti_3C_2T_x$ MXene/Protein Nanocomposites | S = 298.4 $kPa^{-1}$ | 1.4 — 15.7 kPa | 7.1 Pa | 2021 | [21] |
| Carbon nanotube/ MXene/ polydimethylsiloxane | GF = 11.4 | 30 – 60.3% | – | 2021 | [262] |
| Polyacrylamide-co-acrylic acid/chitosan covalent-network@ $Ti_3C_2T_x$ MXene | GF = 3.93 | 0 – 10% | – | 2021 | [71] |
| Carbon nanotube/ $Ti_3C_2T_x$ MXene textiles | S = 0.245 $kPa^{-1}$ | 0.128 – 12.9 kPa | – | 2021 | [263] |
| Co@N-CNT/MXene | GF = 11.01 | 100–200% | – | 2021 | [264] |
| Wrinkled PDMS/MXene composite films | S = 0.18 V/Pa | 10–80 Pa | – | 2021 | [265] |
| PDA-MXene-PDMS decorated textile | GF = 18 | 3 – 30% | – | 2021 | [202] |
| MXene/single-wall carbon nanotube film | S = 116.15 $kPa^{-1}$ | 0 – 40 kPa | 33 Pa | 2021 | [266] |
| Polydimethylsiloxane (PDMS)/$Ti_3C_2T_x$ MXene | S = 66.3 nF $kPa^{-1}$ | 0 – 0.5 kPa | – | 2021 | [267] |
| Carbon nanotubes/ MXene composite | GF = 3.94 | 0 – 8% | – | 2021 | [268] |
| F-MXene@C-CNTs/CCS aerogel | S = 3.84 $kPa^{-1}$ | 0 – 12.4 kPa | – | 2021 | [269] |
| MXene/air-laid paper composite | GF = 1 – 2.58 | 10 – 90% | – | 2021 | [270] |
| SAA (SA/PAA)/ $Al^{3+}$/ MXene | S = 0.075 $kPa^{-1}$ and GF = 4.3 | 0 – 5 kPa and 130 – 200% | – | 2021 | [271] |
| MXene/ 3D network electrode | S = 10.2 $kPa^{-1}$ | 0 — 8.6 kPa | – | 2021 | [272] |

**Table 8** (continued)

| Materials | Pressure Sensitivity (S)/ Gauge factor (GF) | Linear range | Detection limit | Year | Refs |
|---|---|---|---|---|---|
| X-SF-MXene9-GO | $S = 14.23\ kPa^{-1}$ | 0 – 1.4 kPa | – | 2021 | [273] |
| PVA/SA/MXene dual-network conductive hydrogel | GF = 0.97 | 0 – 100% | 0.2% | 2021 | [274] |
| MXene@cotton fabric | GF = 4.11 | 0.3 – 15% | 0.3% | 2021 | [275] |
| Highly oriented MXene-based three dimensional conductive networks | $S = 0.38\ kPa^{-1}$ and GF = 18.15 | 0 – 3 kPa and 96 – 150% | – | 2021 | [276] |
| MXene/polyurethane/ polyacrylonitrile | GF = 9.69 | 0 – 80% | < 0.1% | 2021 | [277] |
| $Ti_3C_2T_x$@P(VDF-TrFE) | GF = 108.8 | 45 – 66% | – | 2021 | [278] |
| Microstructured MXene/ polyurethane fibrous membrane | GF = 1000 | 120 – 160% | 0.05% | 2021 | [279] |

MXene-based smart fabric with reliable flexibility, excellent breathability, and self-controllable electro-thermal effect [203]. Taking advantage of the multifunctional MXene-based smart fabric, they successfully applied it in the field of smart hyperthermia, which could effectively warm the body and relieve muscle spasms and joint damage under a low voltage supply. Furthermore, the smart fabric had a good joule heating effect, such that it was moderately bactericidal and could accelerate healing.

In terms of human motion status monitoring, wearable MXene textiles can be designed as bracelets or patches to obtain real-time motion feedback (Fig. 14 (d)). When people walk and run, the bending degree of the knee varies; hence, MXene textile sensors attached to the knees can be used to monitor the movement state of the human body in real time (Fig. 14 (e)) [65]. In addition, the movements of other human joints, such as fingers, arms, and ankles, can be monitored using MXene textile sensors (Fig. 14 (f–h)) [21, 260]. The wearable MXene sensor also has exciting application potential in physiological signal detection (Fig. 14(i)) [285]. According to the throat vibration, the electrical signal output acquired by the MXene sensor can be used to distinguish the tones of different words, which makes the development of a smart sound generator possible for the benefit of mute people [285]. Moreover, the use of MXene nanofibers is a novel method for fabricating wearable devices [286]. Wang et al. fabricated a conductive MXene@aramid fiber through wet spinning (Fig. 14(j, k)) [286]. The MXene@aramid fiber had a high conductivity (2515 S $m^{-1}$), which is suitable for designing smart wearable devices for monitoring human movements. In conclusion, both MXene-based textiles and fibers are important candidates for designing wearable smart sensing devices.

#### MXene-based sensing technology for bionic E-skin

The skin is one of the most important organs of human beings, and touch is the core function of the skin for sensing surroundings, such as the sensing of strain, temperature, and humidity. In recent years, MXenes have been used for developing bionic electronic skins (E-skins) because of their excellent strain, temperature, and humidity sensing capabilities [21, 217, 287, 288]. Figure 15(a) shows the spinous microstructure model of human skin [22]. The spinous microstructure typically provides highly concentrated

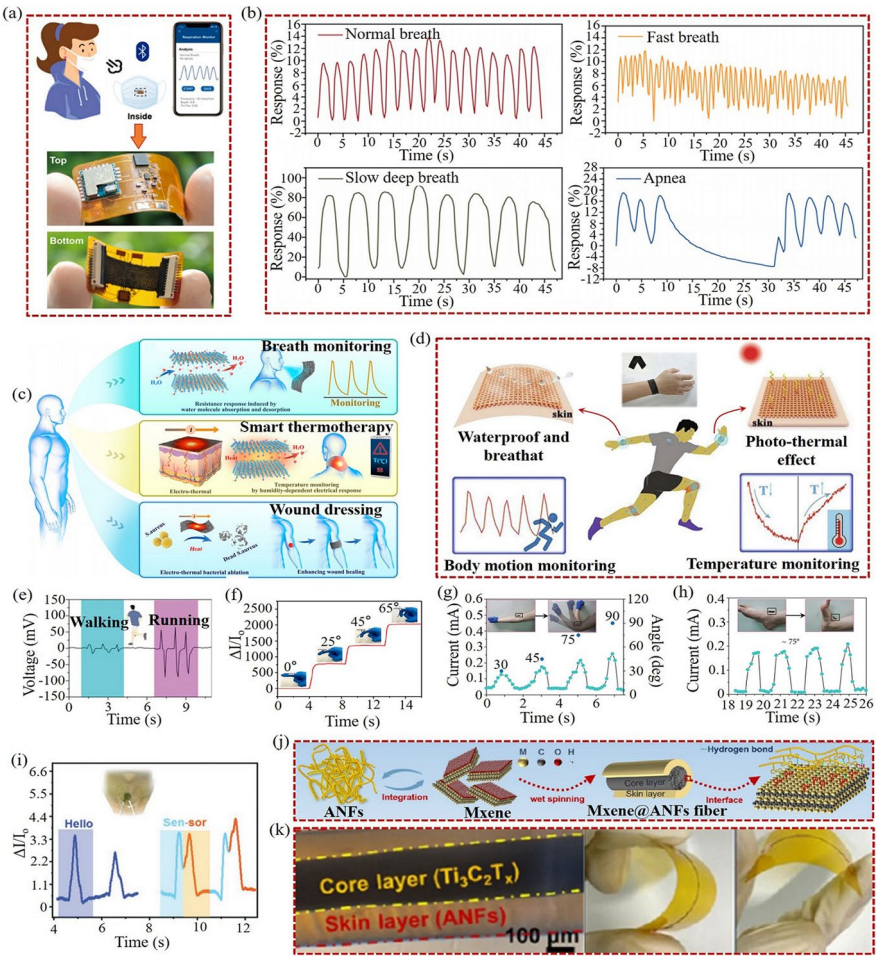


**Fig. 14** **a** Schematic diagram of the wireless data transmission and detection of the MXene-based breathing sensor [284]. **b** The response signals of the MXene-based smart sensor under different breathing states [284]. Copyright 2022, Elsevier. **c** The application of MXene-based smart sensor in breath monitoring, smart thermotherapy, and wound dressing [203]. Copyright 2020, American Chemical Society. **d** Model diagram of MXene-based wearable textile for human physiological information detection [202]. Copyright 2021, Elsevier. **e**–**h** Electrical responses of MXene-based wearable sensor under different joint movements of the human body [21, 65, 260]. Copyright 2021, American Chemical Society. Copyright 2021, American Association for the Advancement of Science. Copyright 2021, Springer Singapore. **i** Electrical responses of MXene-based wearable sensor for speaking "hello" and "sensor" [285]. Copyright 2020, Wiley–VCH. **j** Fabrication of conductive MXene@aramid fiber by the method of wet spinning [286]. **k** Morphology of MXene@aramid fiber and its fabricated wearable device [286]. Copyright 2021, American Chemical Society

localized stress in the contact area, improving the sensitivity and accuracy of skin to pressure. The sensing film prepared using microspinous $Ti_3C_2T_x$ MXene had a structure similar to that of human skin, and it possessed outstanding electrical conductivity, making it an ideal candidate for bionic E-skin. The sections and models of the microstructure of the MXene-based bionic E-skin in pristine, light-loaded, heavy-loaded, and recovered conditions are shown in Fig. 15(b) [22]. When E-skin was subjected to external extrusion, with the increase in pressure, the contact area between microspinous MXene and the interdigital electrodes gradually increased, thereby significantly increasing the conductive path and eventually causing changes in resistance or current. When the external force was withdrawn, the microspinous MXene-based E-skin quickly returned to its

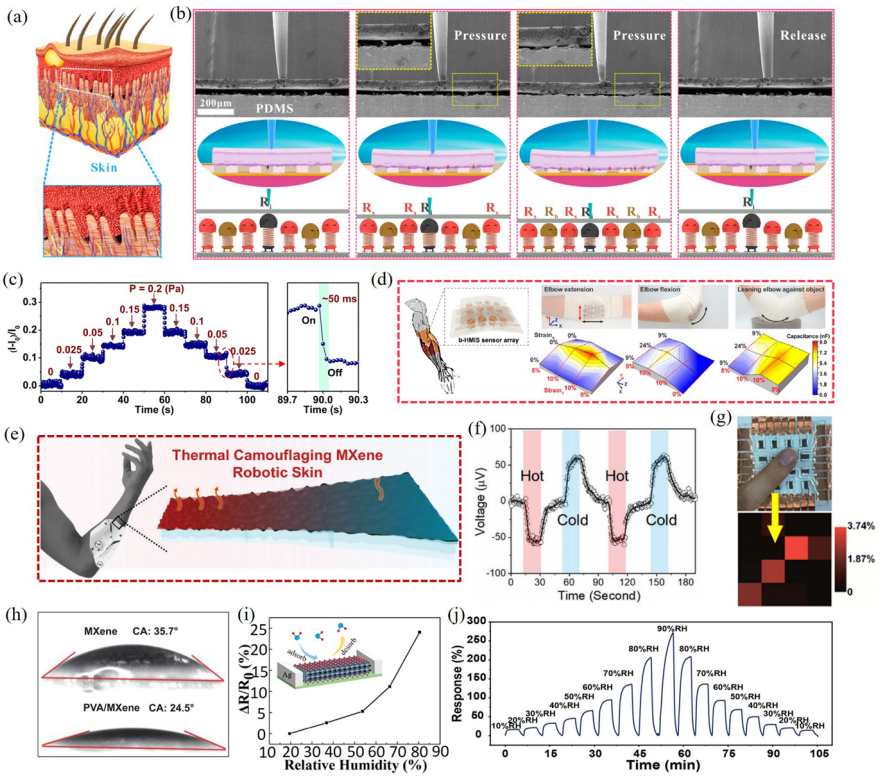


**Fig. 15** **a** The spinous microstructure model of human skin [22]. **b** The sections and models of the microstructure of the $Ti_3C_2T_x$ MXene-based bionic E-skin in pristine, light-loaded, heavy-loaded, and recovered conditions [22]. Copyright 2020, American Chemical Society. **c** Variation in relative current at different pressures [219]. Copyright 2022, Springer Nature. **d** Photographs of the elbow joint with MXene array sensing E-skin under different motion states and the corresponding mapping of the strain-induced capacitance distribution [267]. Copyright 2021, American Chemical Society. **e** Schematic diagram of thermal response of MXene bionic E-skin [288]. **f** Temperature sensitivity of $Ti_3C_2T_x$ MXene-based bionic E-skin [288]. Copyright 2022, Wiley–VCH. **g** $Ti_3C_2T_x$ MXene-based array unit, and its response to temperature [204]. Copyright 2019, Royal Society of Chemistry. **h** Hydrophilic characterization of MXene and its complex [65]. Copyright 2021, Springer Singapore. **i** Change in relative resistance of the MXene-based bionic E-skin with increasing humidity [203]. Copyright 2020, American Chemical Society. **j** The humidity response of the MXene-based bionic E-skin during humidification and drying [284]. Copyright 2022, Elsevier

original state, resulting in a reduction in the contact surface area. During the pressure application and withdrawal process, the relative current of the MXene-based E-skin showed a strict symmetrical relationship, indicating the good recoverability (Fig. 15(c)) [219]. When MXene materials are fabricated into arrays as bionic E-skins, their excellent electrical sensing properties enable sensitive detection of strain. MXene materials can be fabricated as array units, which are then attached to the robot body as bionic E-skin, such as at the elbow joint. When the elbow joint bends, or when a foreign object extrudes, the electrical properties of bionic E-skin are significantly affected, thereby realizing real-time response to external strain (Fig. 15(d)) [267].

MXene-based E-skin should also be sensitive to temperature (Fig. 15(e)) [288]. Temperature sensitivity is demonstrated in Fig. 15(f), which shows that the voltage exhibits stable and sensitive changes in response to repeated hot and cold stimuli. Even slight thermal changes in the environment can be sensed by the E-skin. As an example, MXene was fabricated into an array unit similar to skin, and a finger was used as

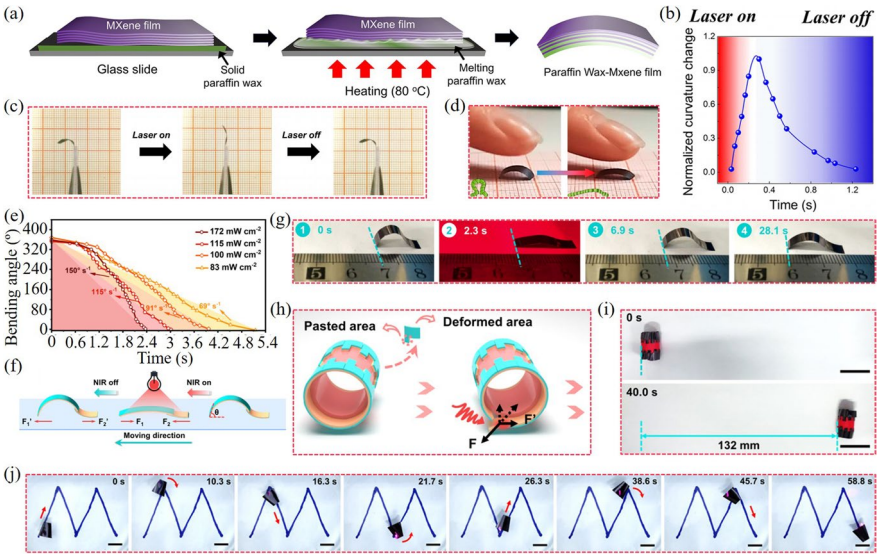


**Fig. 16** **a** Schematic diagram of the MX-PW-based soft robot fabrication [300]. **b** Transient response of the MX-PW film under light-driven [300]. **c** Changes in the morphology of the MX-PW film under laser radiation [300]. **d** The finger was used as a thermal source to drive the soft robot to wriggle [300]. Copyright 2021, American Chemical Society. **e** Actuation speed of the MXene/LDPE-based soft robot with different intensity [301]. **f** Schematic illustration of light-driven soft robot crawling [301]. **g** Crawling images of the soft robot driven by light [301]. **h** Construction of the MXene/LDPE-based rolling robot [301]. **i** Rolling images of the soft robot driven by light [301]. **j** Turning and sailing of the MXene/LDPE-based soft robot [301]. Copyright 2021, American Chemical Society

the weak heat source close to the top of the temperature sensor array (Fig. 15(g)) [204]. The $Ti_3C_2T_x$ MXene-based E-skin could accurately sense the position of the finger and respond through resistance changes in the sensor. Finally, MXene-based bionic E-skins are also extremely sensitive to humidity, which can be attributed to the abundant functional groups on the surface that enhance their hydrophilicity (Fig. 15(h)) [65]. Moisture changes in the environment can also be captured by the MXene-based bionic E-skin and converted into electrical signals for further processing (Fig. 15(i)) [203]. The humidity response exhibited good stability and recoverability during humidification and drying, which proves the feasibility for the design of E-skin (Fig. 15(j)) [284].

### MXene-based sensing technology for bionic soft robot

Bionic soft robots have been at the frontier of scientific research in recent years, and they present potentially critical application prospects in many fields, such as medical treatment, reconnaissance, and industrial production [289–292]. The design of bionic soft robots is inspired by animals, plants, and humans, and they feature excellent flexibility, adaptability, and versatility [293–296]. Functional nanomaterials with good flexibility and strong plasticity are important raw materials for soft robot fabrication [297]. As emerging nanomaterials, MXene and its composites present excellent light absorption, high photothermal/electrothermal response efficiency, high flexibility, low photo-triggering power, and fast response time, which make them outstanding candidates for the fabrication of soft robots [298–300]. Inspired by the crawling behavior of bugs, Xiao et al. fused $Ti_3C_2T_x$ MXene with paraffin wax into a composite material (MX–PW) of

soft robot (Fig. 16(a)) [300]. The MX–PW soft robot possessed thermal sensitivity and wavelength selectivity. Under laser radiation with a wavelength of 808 nm, the MX–PW actuator was driven and made a curvature change within a short time (Fig. 16(b)) because of its high thermal sensitivity (4.6 $m^{-1}$/°C). Figure 16(c) shows the deformation and recovery processes of the MX–PW film under light, indicating its excellent maneuverability. The MX–PW soft robot has the advantage of low trigger power. Although the thermal field energy generated with the finger is low, it can drive the robot to wriggle (Fig. 16(d)).

The actuation speed of the MXene-based soft robot is highly dependent on the radiation intensity; the higher the radiation intensity, the faster is the actuation speed. Luo et al. reported a soft robot based on MXene/low-density polyethylene (LDPE) bilayer films, which could perform crawling, rolling, and sailing commands through free-form cutting and programmable configuration [301]. The actuation speed of the reported MXene/LDPE-based soft robot reached 150° $s^{-1}$ under a radiation intensity of 172 mW $cm^{-2}$ (Fig. 16(e)). Driven by the repeated "on/off" of the near-infrared light, the bionic soft robot crawled forward in a rhythmic manner (Fig. 16(f, g)). Next, the MXene film was cut into gear-like structures and attached to the edge of the plastic circular tube, which were fabricated into a rolling robot. When the gear-shaped structure contacting the ground was partially irradiated by the laser, its structural unit deformed and bent, thereby generating a thrust on the ground. At this time, the rolling robot rolled forward under the action of the reverse thrust (Fig. 16(h, i)). Driven by light, the MXene/LDPE-based soft robot could steer and navigate (Fig. 16(j)) and finally, it could turn and sail (Fig. 16(j)). According to the Marangoni effect, when the MXene/LDPE robot material is driven by light, the temperature of the nearby water increases rapidly, and the surface tension of the water also increases, forming a surface tension gradient with other places with low surface tension. At this time, water with low surface tension flows to the water with high surface tension, thereby promoting the turning and sailing of the robot. As shown in Fig. 16(j), driving different parts of the robot with light can make the robot navigate with programmable routes.

#### MXene-based sensing technology for neural network coding and learning

MXene and its complexes are ideal candidates for mechanical sensing materials, and they are sensitive to the externally applied pressure or strain. With the mechanically sensitive advantage of MXene, it can be applied to the research on neural network coding and learning [24, 302, 303]. Inspired by the biological nervous system (Fig. 17(a)), Tan et al. reported an artificial nervous system based on MXene [24]. They imitated the working principle of subcutaneous afferent nerves and innovatively combined the MXene pressure sensor-based E-skin, analog-to-digital converter/light-emitting diode (ADC–LED) circuit, and synaptic photomemristor to realize the information transmission similar to that in a biological neural network. In the artificial nervous system, the pressure exerted on the E-skin can be converted into a voltage signal, and the ADC–LED circuit then processes the received voltage signal and uses the encoded pressure information to initiate light pulses. Finally, the light pulses are transmitted to an optoelectronic synapse and processed into a post-synaptic current signal to store the pressure information.

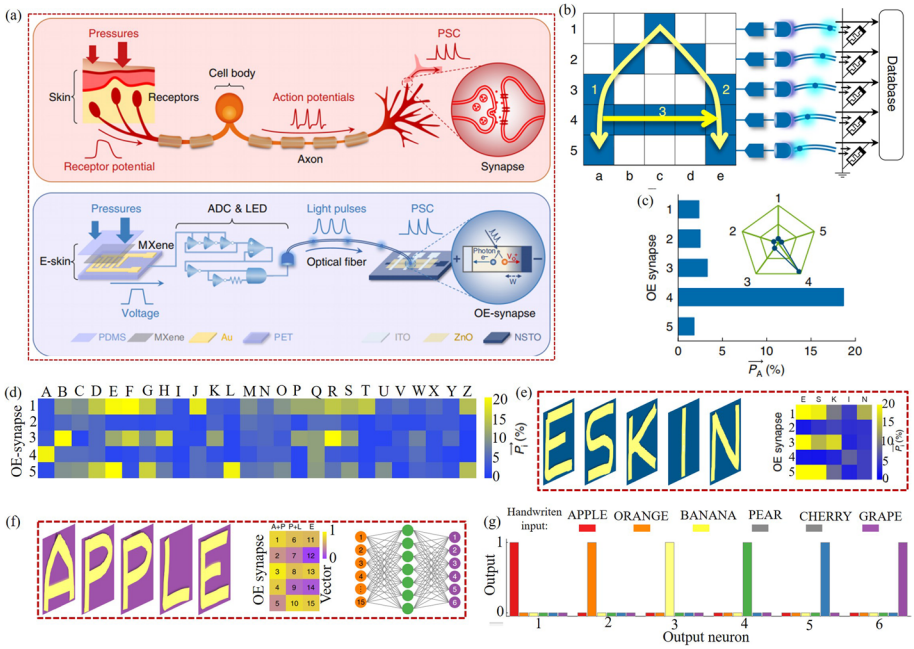


**Fig. 17** **a** Construction diagrams of biological and artificial neural networks. **b** Working principle of the MXene-based artificial neural network. **c** Characteristic information of letter 'A' extracted by optoelectronic synapse. **d** Feature dictionary of different letters. **e** Handwritten word 'ESKIN', and its feature dictionary. **f** Reduced vector dimensionality for learning and recognition of the handwritten word 'APPLE'. **g** Recognition of different handwritten words by artificial neural network after training [24]. Copyright 2020, Springer Nature

To highlight the ability of artificial neural network to process and store a large amount of sensory data, machine learning was used to extract and learn the features of the data. First, the MXene-based pressure sensing structure was fabricated into connected $5 \times 5$ array units (Fig. 17(b)). Next, the letter 'A' was written on the array unit, which was transmitted and recognized by the artificial neural network system. Although the output signals of 25 array units were not collected and analyzed, the spiking proportions of 5 synaptic photoelectric emitters were used as 5-dimensional features for subsequent recognition and learning through dimension reduction processing. Finally, for the input 'A' signal, the features extracted by the artificial neural network are shown in Fig. 17(c). For each of the letters, the spiking proportions received by the photoelectric synapse were different; in this manner, a dictionary of characteristic code letters (Fig. 17(d)) could be obtained. Through multiple training and learning, the recognition accuracy can be greatly improved, and finally, the feature learning and memory of handwritten input can be realized. A handwritten letter corresponds to 5-dimensional vectors; thus, for a complete word, the vector dimensions are multiplied. Taking the handwritten word 'ESKIN' as an example, 5 letters generate 25-dimensional vectors (Fig. 17(e)). Through the training and learning of the MXene-based artificial neural network, handwritten word 'ESKIN' can be accurately recognized and memorized. Furthermore, by combining two-letter vectors, dimensionality reduction for handwritten words can be further acquired. Taking the word 'APPLE' as an example, the letters 'AP' and 'PL' were formed into an independent set of 5-dimensional vectors, thereby reducing the 25-dimensional

vectors to the 15-dimensional vectors. Through training and learning, 'APPLE' can still be recognized and remembered (Fig. 17(f)). Similarly, feature extraction of other handwritten words can be successfully recognized using the artificial neural network systems (Fig. 17(g)).

#### MXene-based sensing technology for intelligent artificial eardrum

In Pressure/strain sensors section, MXene-based pressure/strain sensors with high sensitivity and durability are summarized. Under an external force, the MXene-based strain sensor deforms, converting the external force signal into useful electrical signals, such as resistance, current, and capacitance. Taking advantage of the outstanding strain capacity of MXene, it can also be developed as an acoustic sensor [226]. Recently, Gou et al. designed a microstructured substrate-based MXene acoustic sensor for sound detection and recognition by imitating the function of the human eardrum (Fig. 18(a)) [227]. They utilized the combination of $Ti_3C_2T_x$ MXene with large interlayer distances and microcone arrays (Fig. 18(b)) to achieve 2-stage amplification for pressure and acoustic sensing and obtained a high-performance artificial eardrum. In the MXene-based intelligent artificial eardrum, the total resistance ($R_{total}$) around the pyramid array mainly had three components, namely, resistance without the pyramid surface ($R_w$), resistance at the top of the pyramid ($R_t$), and resistance on the pyramid surface (Rs) (Fig. 18(c)). Under the stimulation of external sound waves, the MXene-based eardrum acts as a signal converter to generate vibrations, converting the acoustic signal into a change signal of $R_{total}$ to be effectively perceived. A comparison revealed that MXene has a stronger resistance response than graphene at the same sound pressure (Fig. 18(d)), which proves that MXene is more suitable for making intelligent artificial eardrums. The artificial eardrum made of $Ti_3C_2T_x$ MXene material has a highly sensitive detection function ($S = 62\ k{\cdot}Pa^{-1}$), with the detection limit of 0.1 Pa (Fig. 18(e)).

The MXene eardrum can convert different word pronunciations into distinguishable electrical resistance signals, thereby realizing the function of sound recognition and memory (Fig. 18(f)). To better realize the recognition and classification of different speech signals by the MXene eardrum, machine learning is introduced to extract the feature information of different speech signals. Machine learning method of *k*-means clustering algorithm is used to train, learn, and test the speech signals recorded by the MXene eardrum ((Fig. 18(g))). The accuracy rates for the training data set and the test data set were 96.4% and 95%, respectively. As shown in Fig. 18(h), 280 sets of sounds with similar characteristics can be visualized into a low-dimensional space using t-distributed stochastic neighbor embedding, forming 7 clusters of different colors, each point of which represents visualized speech information. These visualized speech information points with the same color are all clustered within a certain range, which indicates their good recognition and classification functions. Inconsistency between the speech prediction and test datasets is shown in Fig. 18(i), which are well matched, reflecting the high sensitivity and strong recognition ability of the MXene eardrum to speech signals.

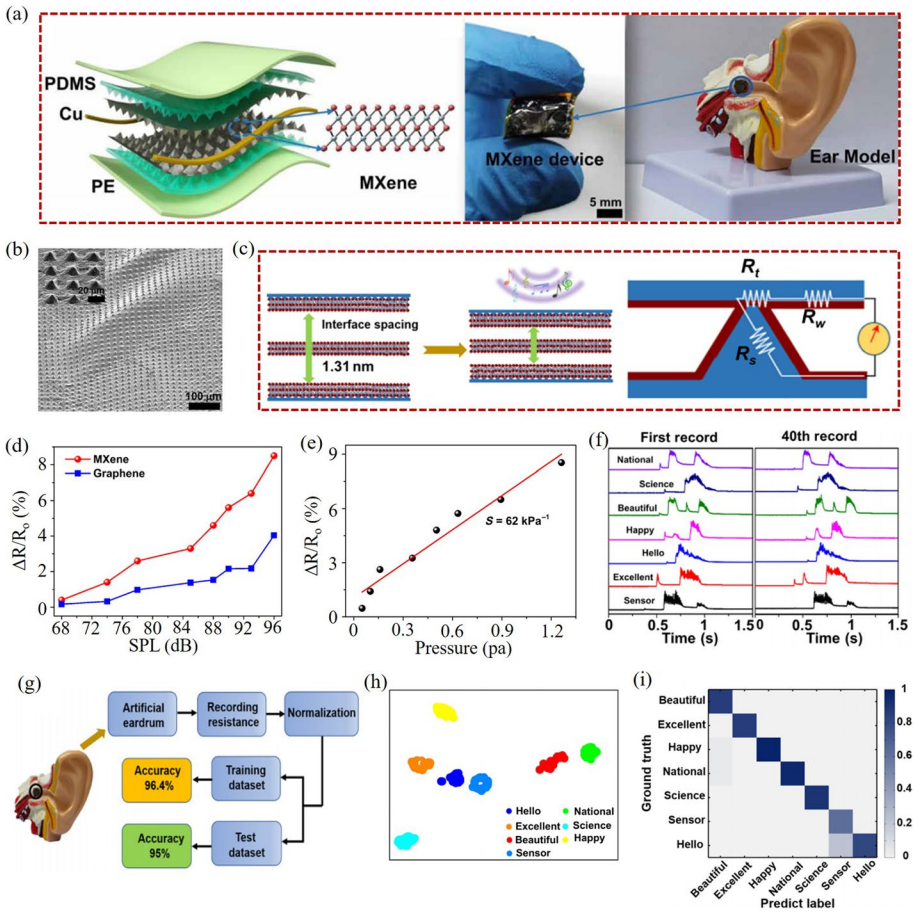


**Fig. 18** **a** Schematic illustration of the MXene-based intelligent artificial eardrum. **b** SEM image of the microcone arrays covered with MXene. **c** The change of the total resistance of the MXene eardrum under the action of external sound signals. **d** Comparison of resistance responses of MXene and graphene under the same sound pressure level. **e** Sensitivity of the MXene-based intelligent artificial eardrum. **f** Different speech signals recorded by the MXene eardrum. **g** Flowchart of machine learning. **h** Visualization results after dimensionality reduction of speech information. **i** Inconsistency results between the prediction dataset and the test dataset for speech information [227]. Copyright 2022, American Association for the Advancement of Science

## Conclusions and outlook

To date, $Ti_{n+1}C_nT_x$ MXenes, represented by $Ti_3C_2T_x$, have been widely reported and applied in sensing technology. They are considered ideal candidates for developing high-performance sensors due to their characteristics, such as abundant surface groups, good hydrophilicity, excellent biocompatibility, high electrical conductivity, and outstanding mechanical properties. This review summarizes nine classes of MXene sensors based on optical and electrical sensing signals, and discusses their applications in intelligent devices, such as neural network coding and learning, bionic soft robot, and intelligent artificial eardrum. In recent years, there has been extensive research on MXene-based sensing applications. Nonetheless, research on MXene materials in the field of sensing still needs to be further expanded. Challenges and prospects for the development of MXenes can be summarized as follows:

### Challenges of MXene materials in sensing technologies

First, the preparation process of MXene sensing materials should be further developed. Currently, MXenes are mainly synthesized by chemical etching, which leads to the uncontrollability of factors such as size, thickness, functional groups, and defects of the materials. These uncontrollable factors lead to inconsistencies in the performance of MXene-based sensors, making mass production impossible. Therefore, new and advanced fabrication methods for MXene material should be further explored to enable better control on the aforementioned factors. The durability of MXene sensing materials is also a concern. The application scenarios of sensors are often complex, which may include harsh environments conditions such as high temperature, humidity, salinity, acidity, and alkalinity, which adversely affects the durability and stability of sensing materials. Therefore, the development of modified MXenes with better durability and stability is an urgent need for developing high-performance MXene-based sensing applications.

Second, the abundant functional groups on the surface of MXene materials endow them with tunable optical and electrical properties, but also bring new challenges. The surface functional groups of MXene cannot exist stably under high temperature conditions and will be removed [304, 305]. Therefore, the development of new MXene materials with high temperature resistance and stable photoelectric performance is a new challenge to be solved urgently.

Finally, at present, most of the sensing research on MXene materials emphasizes the development of application fields, while ignoring the research and improvement of their essential optical and electrical properties. How to improve various essential properties of MXene materials, thereby improving sensing sensitivity, response time, stability, etc., is a key challenge for researchers.

### Prospects of MXene materials in sensing technologies

First, MXene-based sensors can be applied for the development of interactive human–machine interface. Human–machine interface refers to the exchange of information between people and machines, which includes direct contact, as well as long-distance information transmission and control. Through training and learning, different gesture commands issued by gloves equipped with MXene sensing devices can be accurately recognized [302]; however, further applications in human–machine interfaces should be developed [306]. MXenes show good mechanical sensitivity and are excellent potential candidates for human–machine interface development.

Second, intelligent MXene sensing detection based on machine learning should be developed. MXene and its modifications show excellent sensitivity and good selectivity in various sensors. To date, the data analysis of MXene sensing detection technology mainly relies on human processing, which is not conducive to the rapid detection of targets. Therefore, it is necessary to build a sensor data set in the future to realize intelligent selection, identification and quantitative analysis of targets through machine learning.

Third, MXene sensing for seismic wave or acoustic wave detection is also worth developing. The comb-like structure and abundant surface functional groups of MXene materials endow them with tunable optical and electrical properties. Moreover, the optoelectronic performance of MXene can be greatly optimized by combining other

materials to form heterojunctions, or intercalating ions to change the structure. The unique comb structure of MXene materials make them more sensitive to vibrational waves. Under the action of the vibration wave, the comb-like MXene will deform and change the resistance, thereby changing the electrical signal. At this time, the vibration wave can be effectively analyzed by detecting the change of the electrical signal. Furthermore, adding an electro-optic modulator to the output port of the electrical signal can convert the corresponding electrical signal into an optical signal, and finally realize the joint detection mode of electrical and optical to improve the detection accuracy.

Finally, high-entropy MXene should be developed for application in sensing technology. High-entropy MXene is a stable single phase comprising five or more atoms, and its element ratio can be adjusted. Compared with conventional MXenes, high-entropy MXenes have more transition metal species, which greatly optimizes the material properties, such as conductivity, hardness, chemical stability, and volume capacitance [307–309]. However, high-entropy MXene material with excellent performance should be developed in the field of sensing, and its future applications should be investigated in the future.

**Abbreviations**

| | |
|---|---|
| NSs | Nanosheets |
| QDs | Quantum dots |
| SPR | Surface plasmon resonance |
| SERS | Surface-enhanced Raman scattering |
| SEM | Scanning electron microscope |
| TEM | Transmission electron microscope |
| HRTEM | High-resolution transmission electron microscope |
| DFT | Density functional theory |
| HF | Hydrofluoric acid |
| DMSO | Dimethyl sulphoxide |
| PVA | Polyvinyl alcohol |
| 2D | Two-dimensional |
| RI | Refractive index |
| AuNPs | Au nanoparticles |
| SPA | Staphylococcal protein A |
| CEA | Carcinoembryonic antigen |
| $NH_3$ | Ammonia |
| rGO | Reduced graphene oxide |
| Exo III | Exonuclease III |
| N | Nitrogen |
| P | Phosphorus |
| PEI | Polyethyleneimine |
| AFB1 | Mycotoxin B1 |
| BPF | 1,2-Bis(4-pyridyl) ethylene |
| PAA | Poly(acrylic acid) |
| WE | Working electrode |
| CE | Counter electrode |
| RE | Reference electrode |
| MWCNTs | Multi-walled carbon nanotubes |
| S | Sensitivity |
| CCS | Carboxymethyl chitosan |
| CF | Cotton fabric |
| RH | Relative humidity |
| PI | Polyimide |
| PDM | Polydimethylsiloxane |
| BBP–MX–AG | Bottlebrush poly(3-glycidoxypropyldimethoxymethylsilane)–MXene–aerogel |
| E-skins | Electronic skins |
| MX–PW | MXene–paraffin wax |
| LDPE | Low-density polyethylene |
| ADC–LED | Analog-to-digital converter/light-emitting diode |
| $R_{total}$ | Total resistance |
| $R_w$ | Resistance without the pyramid surface |
| $R_t$ | Resistance at the top of the pyramid |
| $R_s$ | Resistance on the pyramid surface |

**Acknowledgements**
Leiming Wu, Xixi Yuan, and Yuxuan Tang contributed equally to this work, and the authors would like to thank Prof. S. Wageh, Omar A. Al-Hartomy, and Abdullah G. Al-Sehemi for their helpful discussions.

**Authors' contributions**
Methodology, Leiming Wu, Xixi Yuan, Yuwen Qin; writing-original draft preparation, Leiming Wu, Yuxuan Tang; writing-review and editing, Leiming Wu, JunYang, S. Wageh, Omar A. Al-Hartomy, Abdullah G. Al-Sehemi, Yuanjiang Xiang, Han Zhang, Yuwen Qin; supervision, Yuanjiang Xiang, Han Zhang, Yuwen Qin. The authors read and approved the final manuscript.

**Funding**
This work is partially supported by the National Key R&D Program of China (Grant No. 2018YFB1801001, and 2019YFB2203503), the National Natural Science Foundation of China (Grant No. 62105069, 61875133 and 11874269), the Guangdong Introducing Innovative and Enterpreneurial Teams of "The Pearl River Talent Recruitment Program" (Grant No. 2019ZT08X340), the Research and Development Plan in Key Areas of Guangdong Province (Grant No. 2018B010114002), the Guangdong Provincial Key Laboratory of Information Photonics Technology (Grant No. 2020B121201011), the Innovation Team Project of Department of Education of Guangdong Province (Grant No. 2018KCXTD026), the Science and Technology Innovation Leading Talents Program of Guangdong Province (Grant No. 2019TX05C343), and King Khalid University through Research Center for Advanced Materials Science (RCAMS) (RCAMS/KKU/006/21).

## Declarations

**Ethics approval and consent to participate**
Not applicable.

**Consent for publication**
Not applicable.

**Competing interests**
The authors declare no competing financial interests.

**Author details**
[1]Guangdong Provincial Key Laboratory of Information Photonics Technology, School of Information Engineering, Guangdong University of Technology, Guangzhou 510006, China. [2]Southern Marine Science and Engineering Guangdong Laboratory (Zhuhai), Zhuhai 519000, China. [3]College of Electronics and Information Engineering, Shenzhen University, Shenzhen 518061, China. [4]Guangdong Laboratory of Artificial Intelligence and Digital Economy (SZ), College of Physics and Optoelectronic Engineering, Shenzhen Key Laboratory of Micro-Nano Photonic Information Technology, Shenzhen University, Shenzhen 518060, China. [5]Department of Physics, Faculty of Science, King Abdulaziz University, Jeddah 21589, Saudi Arabia. [6]Research Center for Advanced Materials Science (RCAMS), King Khalid University, P.O. Box 9004, Abha 61413, Saudi Arabia. [7]School of Physics and Electronics, Hunan University, Changsha 410082, China.

Received: 16 August 2022 Revised: 11 March 2023 Accepted: 21 April 2023
Published online: 05 May 2023

**References**

1. He Y, Yang J. Polarization Estimation with a Single Vector Sensor for Radar Detection. Remote Sens Basel. 2022;14(5):1137.
2. Wu J, Ma D, Wang W, Han Z. Research on Sensor Placement for Disaster Prevention in Water Distribution Networks for Important Users. Sustainability. 2020;12(2):723.
3. Jiang L, Lv S, Tang W, et al. YSZ-based acetone sensor using a $Cd_2SnO_4$ sensing electrode for exhaled breath detection in medical diagnosis. Sensor Actuat B Chem. 2021;345:130321.
4. Verma G, Sharma V. A Novel RF Energy Harvester for Event-Based Environmental Monitoring in Wireless Sensor Networks. IEEE Internet Things J. 2022;9(5):3189–203.
5. Luo J, Yang Y, Wang Z, Chen Y. Localization Algorithm for Underwater Sensor Network: A Review. IEEE Internet Things J. 2021;8(17):13126–44.
6. She S, Liu Y, Zhang S, et al. Flexible Differential Butterfly-Shape Eddy Current Array Sensor for Defect Detection of Screw Thread. IEEE Sens J. 2021;21(18):20764–77.
7. Fathi F, Mohammadzadeh-Aghdash H, Sohrabi Y, Dehghan P, Ezzati Nazhad Dolatabadi J. Kinetic and thermodynamic studies of bovine serum albumin interaction with ascorbyl palmitate and ascorbyl stearate food additives using surface plasmon resonance. Food Chem. 2018;246:228–32.
8. Li K, Liang M, Wang H, et al. 3D MXene Architectures for Efficient Energy Storage and Conversion. Adv Funct Mater. 2020;30(47):2000842.
9. Naguib M, Mochalin VN, Barsoum MW, Gogotsi Y. 25th Anniversary Article: MXenes: A New Family of Two-Dimensional Materials. Adv Mater. 2014;26(7):992–1005.
10. Shi C, Beidaghi M, Naguib M, Mashtalir O, Gogotsi Y, Billinge SJL. Structure of Nanocrystalline $Ti_3C_2$ MXene Using Atomic Pair Distribution Function. Phys Rev Lett. 2014;112(12):125501.
11. Dillon AD, Ghidiu MJ, Krick AL, et al. Highly Conductive Optical Quality Solution-Processed Films of 2D Titanium Carbide. Adv Funct Mater. 2016;26(23):4162–8.

12. Lee E, VahidMohammadi A, Prorok BC, Yoon YS, Beidaghi M, Kim D-J. Room Temperature Gas Sensing of Two-Dimensional Titanium Carbide (MXene). ACS Appl Mater Interfaces. 2017;9(42):37184–90.
13. Naguib M, Kurtoglu M, Presser V, et al. Two-Dimensional Nanocrystals Produced by Exfoliation of $Ti_3AlC_2$. Adv Mater. 2011;23(37):4248–53.
14. Lei Y-J, Yan Z-C, Lai W-H, et al. Tailoring MXene-Based Materials for Sodium-Ion Storage: Synthesis, Mechanisms, and Applications. Electrochem Energy Rev. 2020;3(4):766–92.
15. Liu J, Jiang X, Zhang R, et al. MXene-Enabled Electrochemical Microfluidic Biosensor: Applications toward Multicomponent Continuous Monitoring in Whole Blood. Adv Funct Mater. 2019;29(6):1807326.
16. Mariano M, Mashtalir O, Antonio FQ, et al. Solution-processed titanium carbide MXene films examined as highly transparent conductors. Nanoscale. 2016;8(36):16371–8.
17. Shahzad F, Alhabeb M, Hatter Christine B, et al. Electromagnetic interference shielding with 2D transition metal carbides (MXenes). Science. 2016;353(6304):1137–40.
18. Liu L-X, Chen W, Zhang H-B, et al. Super-Tough and Environmentally Stable Aramid. Nanofiber@MXene Coaxial Fibers with Outstanding Electromagnetic Interference Shielding Efficiency. Nano-Micro Lett. 2022;14(1):111.
19. Shein IR, Ivanovskii AL. Graphene-like titanium carbides and nitrides $Ti_{n+1}C_n$, $Ti_{n+1}N_n$ (n=1, 2, and 3) from de-intercalated MAX phases: First-principles probing of their structural, electronic properties and relative stability. Comp Mater Sci. 2012;65:104–14.
20. Zhang C, Ma Y, Zhang X, et al. Two-Dimensional Transition Metal Carbides and Nitrides (MXenes): Synthesis, Properties, and Electrochemical Energy Storage Applications. Energy Environ Mater. 2020;3(1):29–55.
21. Chao M, He L, Gong M, et al. Breathable $Ti_3C_2T_x$ MXene/Protein Nanocomposites for Ultrasensitive Medical Pressure Sensor with Degradability in Solvents. ACS Nano. 2021;15(6):9746–58.
22. Cheng Y, Ma Y, Li L, et al. Bioinspired Microspines for a High-Performance Spray $Ti_3C_2T_x$ MXene-Based Piezoresistive Sensor. ACS Nano. 2020;14(2):2145–55.
23. Liu L-X, Chen W, Zhang H-B, Wang Q-W, Guan F, Yu Z-Z. Flexible and Multifunctional Silk Textiles with Biomimetic Leaf-Like MXene/Silver Nanowire Nanostructures for Electromagnetic Interference Shielding, Humidity Monitoring, and Self-Derived Hydrophobicity. Adv Funct Mater. 2019;29(44):1905197.
24. Tan H, Tao Q, Pande I, et al. Tactile sensory coding and learning with bio-inspired optoelectronic spiking afferent nerves. Nat Commun. 2020;11(1):1369.
25. Wang H, Cai L, Wang Y, Liu C, Fang G, Wang S. Covalent molecularly imprinted electrochemical sensor modulated by borate ester bonds for hygromycin B detection based on the synergistic signal amplification of Cu-MOF and MXene. Food Chem. 2022;383:132382.
26. Wu Q, Li N, Wang Y, et al. A 2D transition metal carbide MXene-based SPR biosensor for ultrasensitive carcinoembryonic antigen detection. Biosens Bioelectron. 2019;144:111697.
27. Lian P, Dong Y, Wu Z-S, et al. Alkalized $Ti_3C_2$ MXene nanoribbons with expanded interlayer spacing for high-capacity sodium and potassium ion batteries. Nano Energy. 2017;40:1–8.
28. Naguib M, Mashtalir O, Carle J, et al. Two-Dimensional Transition Metal Carbides. ACS Nano. 2012;6(2):1322–31.
29. Lee SH, Eom W, Shin H, et al. Room-Temperature, Highly Durable Ti3C2Tx MXene/Graphene Hybrid Fibers for NH3 Gas Sensing. ACS Appl Mater Interfaces. 2020;12(9):10434–42.
30. Shi L-N, Cui L-T, Ji Y-R, Xie Y, Zhu Y-R, Yi T-F. Towards high-performance electrocatalysts: Activity optimization strategy of 2D MXenes-based nanomaterials for water-splitting. Coordin Chem Rev. 2022;469:214668.
31. Jiang X, Liu S, Liang W, et al. Broadband Nonlinear Photonics in Few-Layer MXene $Ti_3C_2T_x$ (T = F, O, or OH). Laser Photonics Rev. 2018;12(2):1700229.
32. Wu L, Jiang X, Zhao J, et al. MXene-Based Nonlinear Optical Information Converter for All-Optical Modulator and Switcher. Laser Photonics Rev. 2018;12(12):1800215.
33. Huang K, Li C, Li H, et al. Photocatalytic Applications of Two-Dimensional Ti3C2 MXenes: A Review. ACS Appl Nano Mater. 2020;3(10):9581–603.
34. Feng A, Yu Y, Wang Y, et al. Two-dimensional MXene Ti3C2 produced by exfoliation of $Ti_3AlC_2$. Mater Design. 2017;114:161–6.
35. Ghidiu M, Lukatskaya MR, Zhao M-Q, Gogotsi Y, Barsoum MW. Conductive two-dimensional titanium carbide 'clay' with high volumetric capacitance. Nature. 2014;516(7529):78–81.
36. Lipatov A, Alhabeb M, Lukatskaya MR, Boson A, Gogotsi Y, Sinitskii A. Effect of Synthesis on Quality, Electronic Properties and Environmental Stability of Individual Monolayer $Ti_3C_2$ MXene Flakes. Adv Electron Mater. 2016;2(12):1600255.
37. Li T, Yao L, Liu Q, et al. Fluorine-Free Synthesis of High-Purity $Ti_3C_2T_x$ (T=OH, O) via Alkali Treatment. Angew Chem Int Edit. 2018;57(21):6115–9.
38. Xuan J, Wang Z, Chen Y, et al. Organic-base-driven intercalation and delamination for the production of functionalized titanium carbide nanosheets with superior photothermal therapeutic performance. Angew Chem. 2016;128(47):14789–94.
39. Yang S, Zhang P, Wang F, et al. Fluoride-free synthesis of two-dimensional titanium carbide (MXene) using a binary aqueous system. Angew Chem. 2018;130(47):15717–21.
40. Li M, Lu J, Luo K, et al. Element Replacement Approach by Reaction with Lewis Acidic Molten Salts to Synthesize Nanolaminated MAX Phases and MXenes. J of the Am Chem Soc. 2019;141(11):4730–7.
41. Li Y, Shao H, Lin Z, et al. A general Lewis acidic etching route for preparing MXenes with enhanced electrochemical performance in non-aqueous electrolyte. Nat Mater. 2020;19(8):894–9.
42. Mashtalir O, Lukatskaya MR, Zhao M-Q, Barsoum MW, Gogotsi Y. Amine-Assisted Delamination of $Nb_2C$ MXene for Li-Ion Energy Storage Devices. Adv Mater. 2015;27(23):3501–6.
43. Naguib M, Unocic RR, Armstrong BL, Nanda J. Large-scale delamination of multi-layers transition metal carbides and carbonitrides "MXenes." Dalton T. 2015;44(20):9353–8.
44. Mashtalir O, Naguib M, Mochalin VN, et al. Intercalation and delamination of layered carbides and carbonitrides. Nat Commun. 2013;4(1):1716.
45. Li X, Huang Z, Zhi C. Environmental Stability of MXenes as Energy Storage Materials. Front Mater. 2019;6:312.

46. Liu P, Ding W, Liu J, et al. Surface termination modification on high-conductivity MXene film for energy conversion. J Alloy Compd. 2020;829:154634.
47. Wei Y, Zhang P, Soomro RA, Zhu Q, Xu B. Advances in the Synthesis of 2D MXenes. Adv Mater. 2021;33(39):2103148.
48. Chen N, Duan Z, Cai W, et al. Supercritical etching method for the large-scale manufacturing of MXenes. Nano Energy. 2023;107:108147.
49. Berdiyorov GR. Optical properties of functionalized $Ti_3C_2T_2$ (T = F, O, OH) MXene: First-principles calculations. AIP Adv. 2016;6(5):055105.
50. Borysiuk VN, Mochalin VN, Gogotsi Y. Molecular dynamic study of the mechanical properties of two-dimensional titanium carbides $Ti_{n+1}C_n$ (MXenes). Nanotechnology. 2015;26(26):265705.
51. Li R, Sun W, Zhan C, Kent PRC, Jiang D-E. Interfacial and electronic properties of heterostructures of MXene and graphene. Physical Review B. 2019;99(8):085429.
52. Zhang C. Interfacial assembly of two-dimensional MXenes. J Energy Chem. 2021;60:417–34.
53. Zhang CJ, Pinilla S, McEvoy N, et al. Oxidation Stability of Colloidal Two-Dimensional Titanium Carbides (MXenes). Chem Mater. 2017;29(11):4848–56.
54. Anasori B, Lukatskaya MR, Gogotsi Y. 2D metal carbides and nitrides (MXenes) for energy storage. Nat Rev Mater. 2017;2(2):16098.
55. Wang K, Zhou Y, Xu W, Huang D, Wang Z, Hong M. Fabrication and thermal stability of two-dimensional carbide $Ti_3C_2$ nanosheets. Ceram Int. 2016;42(7):8419–24.
56. Li Z, Wang L, Sun D, et al. Synthesis and thermal stability of two-dimensional carbide MXene $Ti_3C_2$. Mater Sci Eng B. 2015;191:33–40.
57. Berdiyorov GR. Optical properties of functionalized Ti3C2T2 (T= F, O, OH) MXene: First-principles calculations. Aip Adv. 2016;6(5): 055105.
58. Ronchi RM, Arantes JT, Santos SF. Synthesis, structure, properties and applications of MXenes: Current status and perspectives. Ceram Int. 2019;45(15):18167–88.
59. Hantanasirisakul K, Zhao M-Q, Urbankowski P, et al. Fabrication of $Ti_3C_2T_x$ MXene Transparent Thin Films with Tunable Optoelectronic Properties. Adv Electron Mater. 2016;2(6):1600050.
60. Zhang C, Anasori B, Seral-Ascaso A, et al. Transparent, Flexible, and Conductive 2D Titanium Carbide (MXene) Films with High Volumetric Capacitance. Adv Mater. 2017;29(36):1702678.
61. Maleski K, Ren CE, Zhao M-Q, Anasori B, Gogotsi Y. Size-Dependent Physical and Electrochemical Properties of Two-Dimensional MXene Flakes. ACS Appl Mater Interfaces. 2018;10(29):24491–8.
62. Dong Y, Chertopalov S, Maleski K, et al. Saturable Absorption in 2D Ti3C2 MXene Thin Films for Passive Photonic Diodes. Adv Mater. 2018;30(10):1705714.
63. Wang C, Wang Y, Jiang X, et al. MXene $Ti_3C_2Tx$: A Promising Photothermal Conversion Material and Application in All-Optical Modulation and All-Optical Information Loading. Adv Opt Mater. 2019;7(12):1900060.
64. Wu Q, Huang W, Wang Y, et al. All-Optical Control of Microfiber Knot Resonator Based on 2D Ti2CTx MXene. Adv Opt Mater. 2020;8(7):1900977.
65. Wang D, Zhang D, Li P, Yang Z, Mi Q, Yu L. Electrospinning of Flexible Poly(vinyl alcohol)/MXene Nanofiber-Based Humidity Sensor Self-Powered by Monolayer Molybdenum Diselenide Piezoelectric Nanogenerator. Nano-Micro Lett. 2021;13(1):57.
66. Peng Q, Guo J, Zhang Q, et al. Unique Lead Adsorption Behavior of Activated Hydroxyl Group in Two-Dimensional Titanium Carbide. J Am Chem Soc. 2014;136(11):4113–6.
67. Yang Z, Liu A, Wang C, et al. Improvement of Gas and Humidity Sensing Properties of Organ-like MXene by Alkaline Treatment. ACS Sensors. 2019;4(5):1261–9.
68. Lashgari H, Abolhassani MR, Boochani A, Elahi SM, Khodadadi J. Electronic and optical properties of 2D graphene-like compounds titanium carbides and nitrides: DFT calculations. Solid State Commun. 2014;195:61–9.
69. Ling Z, Ren Chang E, Zhao M-Q, et al. Flexible and conductive MXene films and nanocomposites with high capacitance. P Natl Acad Sci USA. 2014;111(47):16676–81.
70. Kurtoglu M, Naguib M, Gogotsi Y, Barsoum MW. First principles study of two-dimensional early transition metal carbides. MRS Commun. 2012;2(4):133–7.
71. Li S-N, Yu Z-R, Guo B-F, et al. Environmentally stable, mechanically flexible, self-adhesive, and electrically conductive $Ti_3C_2T_x$ MXene hydrogels for wide-temperature strain sensing. Nano Energy. 2021;90:106502.
72. Li Y, Zhang X. Electrically Conductive, Optically Responsive, and Highly Orientated $Ti_3C_2T_x$ MXene Aerogel Fibers. Adv Funct Mater. 2022;32(4):2107767.
73. Park TH, Yu S, Koo M, et al. Shape-Adaptable 2D Titanium Carbide (MXene) Heater. ACS Nano. 2019;13(6):6835–44.
74. Wang Q-W, Zhang H-B, Liu J, et al. Multifunctional and Water-Resistant MXene-Decorated Polyester Textiles with Outstanding Electromagnetic Interference Shielding and Joule Heating Performances. Adv Funct Mater. 2019;29(7):1806819.
75. Zeng S, Baillargeat D, Ho H-P, Yong K-T. Nanomaterials enhanced surface plasmon resonance for biological and chemical sensing applications. Chem Soc Rev. 2014;43(10):3426–52.
76. Wu L, Guo J, Wang Q, et al. Sensitivity enhancement by using few-layer black phosphorus-graphene/TMDCs heterostructure in surface plasmon resonance biochemical sensor. Sensor Actuat B Chem. 2017;249:542–8.
77. Wu L, Jia Y, Jiang L, et al. Sensitivity Improved SPR Biosensor Based on the MoS2/Graphene–Aluminum Hybrid Structure. J Lightwave Technol. 2017;35(1):82–7.
78. Xue T, Liang W, Li Y, et al. Ultrasensitive detection of miRNA with an antimonene-based surface plasmon resonance sensor. Nat Commun. 2019;10(1):28.
79. Wu L, Chu HS, Koh WS, Li EP. Highly sensitive graphene biosensors based on surface plasmon resonance. Opt Express. 2010;18(14):14395–400.
80. Zeng S, Sreekanth KV, Shang J, et al. Graphene-Gold Metasurface Architectures for Ultrasensitive Plasmonic Biosensing. Adv Mater. 2015;27(40):6163–9.
81. Wu L, You Q, Shan Y, et al. Few-layer $Ti_3C_2T_x$ MXene: A promising surface plasmon resonance biosensing material to enhance the sensitivity. Sensor Actuat B Chem. 2018;277:210–5.

82. Xu Y, Ang YS, Wu L, Ang LK. High Sensitivity Surface Plasmon Resonance Sensor Based on Two-Dimensional MXene and Transition Metal Dichalcogenide: A Theoretical Study. Nanomaterials. 2019;9(2):165.
83. Chen Y, Ge Y, Huang W, et al. Refractive Index Sensors Based on $Ti_3C_2T_x$ MXene Fibers. ACS Appl Nano Mater. 2020;3(1):303–11.
84. Aaryashree, Shinde PV, Kumar A, Late DJ, Rout CS. Recent advances in 2D black phosphorus based materials for gas sensing applications. J Mater Chem C 2021; 9(11):3773–94.
85. Gao Y, Wang J, Feng Y, et al. Carbon-Iron Electron Transport Channels in Porphyrin-Graphene Complex for ppb-Level Room Temperature NO Gas Sensing. Small. 2022;18(11):2103259.
86. Gogotsi Y, Anasori B. The Rise of MXenes. ACS Nano. 2019;13(8):8491–4.
87. Kim SJ, Koh H-J, Ren CE, et al. Metallic $Ti_3C_2T_x$ MXene Gas Sensors with Ultrahigh Signal-to-Noise Ratio. ACS Nano. 2018;12(2):986–93.
88. Chen WY, Jiang X, Lai S-N, Peroulis D, Stanciu L. Nanohybrids of a MXene and transition metal dichalcogenide for selective detection of volatile organic compounds. Nat Commun. 2020;11(1):1302.
89. Zhao L, Wang K, Wei W, Wang L, Han W. High-performance flexible sensing devices based on polyaniline/MXene nanocomposites. InfoMat. 2019;1(3):407–16.
90. Zhou Y, Wang Y, Wang Y, et al. MXene $Ti_3C_2T_x$-Derived Nitrogen-Functionalized Heterophase $TiO_2$ Homojunctions for Room-Temperature Trace Ammonia Gas Sensing. ACS Appl Mater Interfaces. 2021;13(47):56485–97.
91. Zhi H, Zhang X, Wang F, Wan P, Feng L. Flexible Ti3C2Tx MXene/PANI/Bacterial Cellulose Aerogel for e-Skins and Gas Sensing. ACS Appl Mater Interfaces. 2021;13(38):45987–94.
92. Wang J, Yang Y, Xia Y. Mesoporous MXene/ZnO nanorod hybrids of high surface area for UV-activated $NO_2$ gas sensing in ppb-level. Sensor Actuat B Chem. 2022;353:131087.
93. Yuan W, Yang K, Peng H, Li F, Yin F. A flexible VOCs sensor based on a 3D Mxene framework with a high sensing performance. J Mater Chem A. 2018;6(37):18116–24.
94. Shuck CE, Han M, Maleski K, et al. Effect of $Ti_3AlC_2$ MAX Phase on Structure and Properties of Resultant Ti3C2Tx MXene. ACS Appl Nano Mater. 2019;2(6):3368–76.
95. Jin L, Wu C, Wei K, et al. Polymeric $Ti_3C_2T_x$ MXene Composites for Room Temperature Ammonia Sensing. ACS Appl Nano Mater. 2020;3(12):12071–9.
96. Tai H, Duan Z, He Z, et al. Enhanced ammonia response of Ti3C2Tx nanosheets supported by $TiO_2$ nanoparticles at room temperature. Sensor Actuat B Chem. 2019;298:126874.
97. Wu M, He M, Hu Q, et al. $Ti_3C_2$ MXene-Based Sensors with High Selectivity for NH3 Detection at Room Temperature. ACS Sensors. 2019;4(10):2763–70.
98. Sun S, Wang M, Chang X, et al. $W_{18}O_{49}$/$Ti_3C_2$Tx Mxene nanocomposites for highly sensitive acetone gas sensor with low detection limit. Sensor Actuat B Chem. 2020;304:127274.
99. Choi J, Kim Y-J, Cho S-Y, et al. In Situ Formation of Multiple Schottky Barriers in a Ti3C2 MXene Film and its Application in Highly Sensitive Gas Sensors. Adv Funct Mater. 2020;30(40):2003998.
100. Sun Q, Wang J, Wang X, et al. Treatment-dependent surface chemistry and gas sensing behavior of the thinnest member of titanium carbide MXenes. Nanoscale. 2020;12(32):16987–94.
101. Chen WY, Lai S-N, Yen C-C, Jiang X, Peroulis D, Stanciu LA. Surface Functionalization of Ti3C2Tx MXene with Highly Reliable Superhydrophobic Protection for Volatile Organic Compounds Sensing. ACS Nano. 2020;14(9):11490–501.
102. Wang J, Xu R, Xia Y, Komarneni S. $Ti_2CT_x$ MXene: A novel p-type sensing material for visible light-enhanced room temperature methane detection. Ceram Int. 2021;47(24):34437–42.
103. Xia Y, He S, Wang J, Zhou L, Wang J, Komarneni S. MXene/WS2 hybrids for visible-light-activated $NO_2$ sensing at room temperature. Chem Commun. 2021;57(72):9136–9.
104. Zhang D, Mi Q, Wang D, Li T. MXene/$Co_3O_4$ composite based formaldehyde sensor driven by ZnO/MXene nanowire arrays piezoelectric nanogenerator. Sensor Actuat B Chem. 2021;339:129923.
105. Yang Z, Jiang L, Wang J, et al. Flexible resistive $NO_2$ gas sensor of three-dimensional crumpled MXene $Ti_3C_2T_x$/ZnO spheres for room temperature application. Sensor Actuat B Chem. 2021;326:128828.
106. Peng X, Zhang Y, Lu D, Guo Y, Guo S. Ultrathin $Ti_3C_2$ nanosheets based "off-on" fluorescent nanoprobe for rapid and sensitive detection of HPV infection. Sensor Actuat B Chem. 2019;286:222–9.
107. Wang Z, Xuan J, Zhao Z, Li Q, Geng F. Versatile Cutting Method for Producing Fluorescent Ultrasmall MXene Sheets. ACS Nano. 2017;11(11):11559–65.
108. Desai ML, Basu H, Singhal RK, Saha S, Kailasa SK. Ultra-small two dimensional MXene nanosheets for selective and sensitive fluorescence detection of $Ag^+$ and $Mn^{2+}$ ions. Colloid Surface A. 2019;565:70–7.
109. Chen X, Sun X, Xu W, et al. Ratiometric photoluminescence sensing based on $Ti_3C_2$ MXene quantum dots as an intracellular pH sensor. Nanoscale. 2018;10(3):1111–8.
110. Guan Q, Ma J, Yang W, et al. Highly fluorescent $Ti_3C_2$ MXene quantum dots for macrophage labeling and $Cu^{2+}$ ion sensing. Nanoscale. 2019;11(30):14123–33.
111. Xue Q, Zhang H, Zhu M, et al. Photoluminescent Ti3C2 MXene Quantum Dots for Multicolor Cellular Imaging. Adv Mater. 2017;29(15):1604847.
112. Bhardwaj SK, Singh H, Khatri M, Kim K-H, Bhardwaj N. Advances in MXenes-based optical biosensors: A review. Biosens Bioelectron. 2022;202:113995.
113. Zhu X, Fan L, Wang S, et al. Phospholipid-Tailored Titanium Carbide Nanosheets as a Novel Fluorescent Nanoprobe for Activity Assay and Imaging of Phospholipase D. Anal Chem. 2018;90(11):6742–8.
114. Pandey P, Sengupta A, Parmar S, et al. $CsPbBr_3$–$Ti_3C_2T_x$ MXene QD/QD Heterojunction: Photoluminescence Quenching, Charge Transfer, and Cd Ion Sensing Application. ACS Appl Nano Mater. 2020;3(4):3305–14.
115. Liu M, He Y, Zhou J, Ge Y, Zhou J, Song G. A "naked-eye" colorimetric and ratiometric fluorescence probe for uric acid based on $Ti_3C_2$ MXene quantum dots. Anal Chim Acta. 2020;1103:134–42.
116. Luo W, Liu H, Liu X, Liu L, Zhao W. Biocompatibility nanoprobe of MXene N-$Ti_3C_2$ quantum dot/$Fe^{3+}$ for detection and fluorescence imaging of glutathione in living cells. Colloid Surface B. 2021;201:111631.
117. Wang S, Wei S, Wang S, et al. Chimeric DNA-Functionalized Titanium Carbide MXenes for Simultaneous Mapping of Dual Cancer Biomarkers in Living Cells. Anal Chem. 2019;91(2):1651–8.

118. Zhu X, Pang X, Zhang Y, Yao S. Titanium carbide MXenes combined with red-emitting carbon dots as a unique turn-on fluorescent nanosensor for label-free determination of glucose. J Mater Chem B. 2019;7(48):7729–35.
119. Zhang Q, Wang F, Zhang H, Zhang Y, Liu M, Liu Y. Universal $Ti_3C_2$ MXenes Based Self-Standard Ratiometric Fluorescence Resonance Energy Transfer Platform for Highly Sensitive Detection of Exosomes. Anal Chem. 2018;90(21):12737–44.
120. Chen F, Lu Q, Zhang Y, Yao S. Strand displacement dual amplification miRNAs strategy with FRET between NaYF4:Yb, Tm/Er upconversion nanoparticles and Ti3C2 nanosheets. Sensor Actuat B Chem. 2019;297:126751.
121. Shi Y-E, Han F, Xie L, et al. A MXene of type $Ti_3C_2T_x$ functionalized with copper nanoclusters for the fluorometric determination of glutathione. Microchim Acta. 2019;187(1):38.
122. Wang S, Song W, Wei S, et al. Functional Titanium Carbide MXenes-Loaded Entropy-Driven RNA Explorer for Long Noncoding RNA PCA3 Imaging in Live Cells. Anal Chem. 2019;91(13):8622–9.
123. Wang S, Zeng P, Zhu X, Lei C, Huang Y, Nie Z. Chimeric Peptides Self-Assembling on Titanium Carbide MXenes as Biosensing Interfaces for Activity Assay of Post-translational Modification Enzymes. Anal Chem. 2020;92(13):8819–26.
124. Hong J, Wang W, Wang J, et al. A turn-on–type fluorescence resonance energy transfer aptasensor for vibrio detection using aptamer-modified polyhedral oligomeric silsesquioxane-perovskite quantum dots/$Ti_3C_2$ MXenes composite probes. Microchim Acta. 2021;188(2):45.
125. Lu L, Han X, Lin J, et al. Ultrasensitive fluorometric biosensor based on $Ti_3C_2$ MXenes with $Hg^{2+}$-triggered exonuclease III-assisted recycling amplification. Analyst. 2021;146(8):2664–9.
126. Cui H, Fu X, Yang L, Xing S, Wang X-F. 2D titanium carbide nanosheets based fluorescent aptasensor for sensitive detection of thrombin. Talanta. 2021;228:122219.
127. Xu G, Niu Y, Yang X, et al. Preparation of $Ti_3C_2T_x$ MXene-Derived Quantum Dots with White/Blue-Emitting Photoluminescence and Electrochemiluminescence. Adv Opt Mater. 2018;6(24):1800951.
128. Guo Z, Zhu X, Wang S, et al. Fluorescent $Ti_3C_2$ MXene quantum dots for an alkaline phosphatase assay and embryonic stem cell identification based on the inner filter effect. Nanoscale. 2018;10(41):19579–85.
129. Liu M, Zhou J, He Y, et al. ε-Poly-L-lysine-protected $Ti_3C_2$ MXene quantum dots with high quantum yield for fluorometric determination of cytochrome c and trypsin. Microchim Acta. 2019;186(12):770.
130. Lu Q, Wang J, Li B, et al. Dual-Emission Reverse Change Ratio Photoluminescence Sensor Based on a Probe of Nitrogen-Doped $Ti_3C_2$ Quantum Dots@DAP to Detect H2O2 and Xanthine. Anal Chem. 2020;92(11):7770–7.
131. Liu M, Bai Y, He Y, et al. Facile microwave-assisted synthesis of $Ti_3C_2$ MXene quantum dots for ratiometric fluorescence detection of hypochlorite. Microchim Acta. 2021;188(1):15.
132. Wang X, Zhang X, Cao H, Huang Y. A facile and rapid approach to synthesize uric acid-capped $Ti_3C_2$ MXene quantum dots for the sensitive determination of 2,4,6-trinitrophenol both on surfaces and in solution. J Mater Chem B. 2020;8(47):10837–44.
133. Zhang Q, Sun Y, Liu M, Liu Y. Selective detection of $Fe^{3+}$ ions based on fluorescence MXene quantum dots via a mechanism integrating electron transfer and inner filter effect. Nanoscale. 2020;12(3):1826–32.
134. Feng Y, Zhou F, Deng Q, Peng C. Solvothermal synthesis of in situ nitrogen-doped $Ti_3C_2$ MXene fluorescent quantum dots for selective Cu2+ detection. Ceram Int. 2020;46(6):8320–7.
135. Bai Y, He Y, Wang M, Song G. Microwave-assisted synthesis of nitrogen, phosphorus-doped $Ti_3C_2$ MXene quantum dots for colorimetric/fluorometric dual-modal nitrite assay with a portable smartphone platform. Sensor Actuat B Chem. 2022;357:131410.
136. Cong S, Wang Z, Gong W, et al. Electrochromic semiconductors as colorimetric SERS substrates with high reproducibility and renewability. Nat Commun. 2019;10(1):678.
137. Zhang X, Zhang X, Luo C, et al. Volume-Enhanced Raman Scattering Detection of Viruses. Small. 2019;15(11):1805516.
138. Lee HG, Choi W, Yang SY, et al. PCR-coupled Paper-based Surface-enhanced Raman Scattering (SERS) Sensor for Rapid and Sensitive Detection of Respiratory Bacterial DNA. Sensor Actuat B Chem. 2021;326:128802.
139. Yang E, Li D, Yin P, et al. A novel surface-enhanced Raman scattering (SERS) strategy for ultrasensitive detection of bacteria based on three-dimensional (3D) DNA walker. Biosens Bioelectron. 2021;172:112758.
140. Wang T, Wang S, Cheng Z, et al. Emerging core–shell nanostructures for surface-enhanced Raman scattering (SERS) detection of pesticide residues. Chem Eng J. 2021;424:130323.
141. Yu H, Wang M, Cao J, et al. Determination of Dichlorvos in Pears by Surface-Enhanced Raman Scattering (SERS) with Catalysis by Platinum Coated Gold Nanoparticles. Anal Lett. 2022;55(3):427–37.
142. Chen C, Wang X, Waterhouse GIN, Qiao X, Xu Z. A surface-imprinted surface-enhanced Raman scattering sensor for histamine detection based on dual semiconductors and Ag nanoparticles. Food Chem. 2022;369:130971.
143. Zhang D, Pu H, Huang L, Sun D-W. Advances in flexible surface-enhanced Raman scattering (SERS) substrates for nondestructive food detection: Fundamentals and recent applications. Trends Food Sci Tech. 2021;109:690–701.
144. Dong J-C, Zhang X-G, Briega-Martos V, et al. In situ Raman spectroscopic evidence for oxygen reduction reaction intermediates at platinum single-crystal surfaces. Nat Energy. 2019;4(1):60–7.
145. Zheng F, Ke W, Shi L, Liu H, Zhao Y. Plasmonic Au–Ag Janus Nanoparticle Engineered Ratiometric Surface-Enhanced Raman Scattering Aptasensor for Ochratoxin A Detection. Anal Chem. 2019;91(18):11812–20.
146. Karthick Kannan P, Shankar P, Blackman C, Chung C-H. Recent Advances in 2D Inorganic Nanomaterials for SERS Sensing. Adv Mater. 2019;31(34):1803432.
147. Wu Z, Sun D-W, Pu H, Wei Q, Lin X. Ti3C2Tx MXenes loaded with Au nanoparticle dimers as a surface-enhanced Raman scattering aptasensor for AFB1 detection. Food Chem. 2022;372:131293.
148. Medetalibeyoglu H, Kotan G, Atar N, Yola ML. A novel sandwich-type SERS immunosensor for selective and sensitive carcinoembryonic antigen (CEA) detection. Anal Chim Acta. 2020;1139:100–10.
149. Liu R, Jiang L, Yu Z, et al. MXene ($Ti_3C_2T_x$)-Ag nanocomplex as efficient and quantitative SERS biosensor platform by in-situ PDDA electrostatic self-assembly synthesis strategy. Sensor Actuat B Chem. 2021;333:129581.
150. Xie X, Zhu Y, Li F, Zhou X, Xue T. Preparation and characterization of $Ti_3C_2T_x$ with SERS properties. Sci China Technol Sci. 2019;62(7):1202–9.

151. Wang Y, Wang S, Dong N, Kang W, Li K, Nie Z. Titanium Carbide MXenes Mediated In Situ Reduction Allows Label-Free and Visualized Nanoplasmonic Sensing of Silver Ions. Anal Chem. 2020;92(6):4623–9.
152. Tao Y, Yi K, Wang H, et al. CRISPR-Cas12a-regulated DNA adsorption and metallization on MXenes as enhanced enzyme mimics for sensitive colorimetric detection of hepatitis B virus DNA. J Colloid Inter Sci. 2022;613:406–14.
153. Li M, Peng X, Han Y, Fan L, Liu Z, Guo Y. $Ti_3C_2$ MXenes with intrinsic peroxidase-like activity for label-free and colorimetric sensing of proteins. Microchem J. 2021;166:106238.
154. Chen Z, Liu C, Cao F, Ren J, Qu X. DNA metallization: principles, methods, structures, and applications. Chem Soc Rev. 2018;47(11):4017–72.
155. Wang Y, Counihan MJ, Lin JW, Rodríguez-López J, Yang H, Lu Y. Quantitative Analysis of DNA-Mediated Formation of Metal Nanocrystals. J Am Chem Soc. 2020;142(48):20368–79.
156. Xu F, Qing T, Qing Z. DNA-coded metal nano-fluorophores: Preparation, properties and applications in biosensing and bioimaging. Nano Today. 2021;36:101021.
157. Li H, Wen Y, Zhu X, Wang J, Zhang L, Sun B. Novel Heterostructure of a MXene@NiFe-LDH Nanohybrid with Superior Peroxidase-Like Activity for Sensitive Colorimetric Detection of Glutathione. ACS Sustainable Chem Eng. 2020;8(1):520–6.
158. Liu J, Lu W, Lu X, Zhang L, Dong H, Li Y. Versatile $Ti_3C_2T_x$ MXene for free-radical scavenging. Nano Res. 2022;15(3):2558–66.
159. Li Y, Kang Z, Kong L, et al. MXene- $Ti_3C_2$/CuS nanocomposites: Enhanced peroxidase-like activity and sensitive colorimetric cholesterol detection. Mater Sci Eng C. 2019;104:110000.
160. He Y, Zhou X, Zhou L, et al. Self-Reducing Prussian Blue on $Ti_3C_2T_x$ MXene Nanosheets as a Dual-Functional Nanohybrid for Hydrogen Peroxide and Pesticide Sensing. Ind Eng Chem Res. 2020;59(35):15556–64.
161. Li X, Lu Y, Liu Q. Electrochemical and optical biosensors based on multifunctional MXene nanoplatforms: Progress and prospects. Talanta. 2021;235:122726.
162. Rhouati A, Berkani M, Vasseghian Y, Golzadeh N. MXene-based electrochemical sensors for detection of environmental pollutants: A comprehensive review. Chemosphere. 2022;291:132921.
163. Kumar S, Lei Y, Alshareef NH, Quevedo-Lopez MA, Salama KN. Biofunctionalized two-dimensional $Ti_3C_2$ MXenes for ultrasensitive detection of cancer biomarker. Biosens Bioelectron. 2018;121:243–9.
164. Shahzad F, Iqbal A, Zaidi SA, Hwang S-W, Koo CM. Nafion-stabilized two-dimensional transition metal carbide ($Ti_3C_2T_x$ MXene) as a high-performance electrochemical sensor for neurotransmitter. J Ind Eng Chem. 2019;79:338–44.
165. Shankar SS, Shereema RM, Rakhi RB. Electrochemical Determination of Adrenaline Using MXene/Graphite Composite Paste Electrodes. ACS Appl Mater Interfaces. 2018;10(50):43343–51.
166. Cheng J, Hu K, Liu Q, Liu Y, Yang H, Kong J. Electrochemical ultrasensitive detection of CYFRA21-1 using $Ti_3C_2T_x$-MXene as enhancer and covalent organic frameworks as labels. Anal Bioanal Chem. 2021;413(9):2543–51.
167. Liu L, Wei Y, Jiao S, Zhu S, Liu X. A novel label-free strategy for the ultrasensitive miRNA-182 detection based on $MoS_2$/$Ti_3C_2$ nanohybrids. Biosens Bioelectron. 2019;137:45–51.
168. Rasheed PA, Pandey RP, Jabbar KA, Ponraj J, Mahmoud KA. Sensitive electrochemical detection of l-cysteine based on a highly stable Pd@ $Ti_3C_2T_x$ (MXene) nanocomposite modified glassy carbon electrode. Anal Methods. 2019;11(30):3851–6.
169. Zhang R, Liu J, Li Y. MXene with Great Adsorption Ability toward Organic Dye: An Excellent Material for Constructing a Ratiometric Electrochemical Sensing Platform. ACS Sensors. 2019;4(8):2058–64.
170. Zhu X, Liu B, Hou H, et al. Alkaline intercalation of $Ti_3C_2$ MXene for simultaneous electrochemical detection of Cd(II), Pb(II), Cu(II) and Hg(II). Electrochim Acta. 2017;248:46–57.
171. Xia Y, Ma Y, Wu Y, Yi Y, Lin H, Zhu G. Free-electrodeposited anodic stripping voltammetry sensing of Cu(II) based on $Ti_3C_2T_x$ MXene/carbon black. Microchim Acta. 2021;188(11):377.
172. Ni M, Chen J, Wang C, et al. A high-sensitive dopamine electrochemical sensor based on multilayer $Ti_3C_2$ MXene, graphitized multi-walled carbon nanotubes and ZnO nanospheres. Microchem J. 2022;178:107410.
173. Laochai T, Yukird J, Promphet N, Qin J, Chailapakul O, Rodthongkum N. Non-invasive electrochemical immunosensor for sweat cortisol based on L-cys/AuNPs/ MXene modified thread electrode. Biosens Bioelectron. 2022;203:114039.
174. Zhang Y, Jiang X, Zhang J, Zhang H, Li Y. Simultaneous voltammetric determination of acetaminophen and isoniazid using MXene modified screen-printed electrode. Biosens Bioelectron. 2019;130:315–21.
175. Parihar A, Singhal A, Kumar N, Khan R, Khan MA, Srivastava AK. Next-Generation Intelligent MXene-Based Electrochemical Aptasensors for Point-of-Care Cancer Diagnostics. Nano-Micro Lett. 2022;14(1):100.
176. Rasheed PA, Pandey RP, Jabbar KA, Mahmoud KA. Platinum nanoparticles/Ti3C2Tx (MXene) composite for the effectual electrochemical sensing of Bisphenol A in aqueous media. J Electroanal Chem. 2021;880:114934.
177. Wang Y, Zeng Z, Qiao J, Dong S, Liang Q, Shao S. Ultrasensitive determination of nitrite based on electrochemical platform of AuNPs deposited on PDDA-modified MXene nanosheets. Talanta. 2021;221:121605.
178. Cao M, Liu S, Liu S, Tong Z, Wang X, Xu X. Preparation of ZnO/ $Ti_3C_2T_x$/Nafion/Au electrode. Microchem J. 2022;175:107068.
179. Rasheed PA, Pandey RP, Rasool K, Mahmoud KA. Ultra-sensitive electrocatalytic detection of bromate in drinking water based on Nafion/Ti3C2Tx (MXene) modified glassy carbon electrode. Sensor Actuat B Chem. 2018;265:652–9.
180. Zhu X, Lin L, Wu R, et al. Portable wireless intelligent sensing of ultra-trace phytoregulator α-naphthalene acetic acid using self-assembled phosphorene/Ti3C2-MXene nanohybrid with high ambient stability on laser induced porous graphene as nanozyme flexible electrode. Biosens Bioelectron. 2021;179:113062.
181. Huang R, Chen S, Yu J, Jiang X. Self-assembled $Ti_3C_2$/MWCNTs nanocomposites modified glassy carbon electrode for electrochemical simultaneous detection of hydroquinone and catechol. Ecotox Environ Safe. 2019;184:109619.
182. He Y, Ma L, Zhou L, Liu G, Jiang Y, Gao J. Preparation and Application of Bismuth/MXene Nano-Composite as Electrochemical Sensor for Heavy Metal Ions Detection. Nanomaterials. 2020;10(5):866.

183. Chia HL, Mayorga-Martinez CC, Antonatos N, et al. MXene Titanium Carbide-based Biosensor: Strong Dependence of Exfoliation Method on Performance. Anal Chem. 2020;92(3):2452–9.
184. Lorencova L, Bertok T, Filip J, et al. Highly stable $Ti_3C_2T_x$ (MXene)/Pt nanoparticles-modified glassy carbon electrode for $H_2O_2$ and small molecules sensing applications. Sensor Actuat B Chem. 2018;263:360–8.
185. Nagarajan RD, Sundaramurthy A, Sundramoorthy AK. Synthesis and characterization of MXene ($Ti_3C_2T_x$)/Iron oxide composite for ultrasensitive electrochemical detection of hydrogen peroxide. Chemosphere. 2022;286:131478.
186. Feng X, Han G, Cai J, Wang X. Au@Carbon quantum Dots-MXene nanocomposite as an electrochemical sensor for sensitive detection of nitrite. J Coll Int Sci. 2022;607:1313–22.
187. Murugan P, Annamalai J, Atchudan R, et al. Electrochemical Sensing of Glucose Using Glucose Oxidase/PEDOT:4-Sulfocalix [4]arene/MXene Composite Modified Electrode. Micromachines. 2022;13(2):304.
188. Huang H, Xie S, Deng L, Yuan J, Yue R, Xu J. Fabrication of rGO/MXene-Pd/rGO hierarchical framework as high-performance electrochemical sensing platform for luteolin detection. Microchim Acta. 2022;189(2):59.
189. Chen Y, Li S, Zhang L, et al. Facile and fast synthesis of three-dimensional Ce-MOF/ $Ti_3C_2T_x$ MXene composite for high performance electrochemical sensing of L-Tryptophan. J Solid State Chem. 2022;308:122919.
190. Liao D, Liu Z, Huang R, Yu J, Jiang X. In-situ construction of porous carbon on embedded N-doped MXene nanosheets composite for simultaneous determination of 4-aminophenol and Acetaminophen. Microchem J. 2022;175:107067.
191. Xia Y, Hu X, Liu Y, Zhao F, Zeng B. Molecularly imprinted ratiometric electrochemical sensor based on carbon nanotubes/cuprous oxide nanoparticles/titanium carbide MXene composite for diethylstilbestrol detection. Microchim Acta. 2022;189(4):137.
192. Kumar J, Soomro RA, Neiber RR, et al. Ni Nanoparticles Embedded $Ti_3C_2T_x$-MXene Nanoarchitectures for Electrochemical Sensing of Methylmalonic Acid. Biosensors. 2022;12(4):231.
193. Wang X, Li M, Yang S, Bai X, Shan J. Self-assembled $Ti_3C_2T_x$ MXene/graphene composite for the electrochemical reduction and detection of p-nitrophenol. Microchem J. 2022;179:107473.
194. Soomro RA, Jawaid S, Zhang P, et al. NiWO4-induced partial oxidation of MXene for photo-electrochemical detection of prostate-specific antigen. Sensor Actuat B Chem. 2021;328:129074.
195. Zhang H, Wang Z, Zhang Q, Wang F, Liu Y. $Ti_3C_2$ MXenes nanosheets catalyzed highly efficient electrogenerated chemiluminescence biosensor for the detection of exosomes. Biosens Bioelectron. 2019;124–125:184–90.
196. Ma X, Tu X, Gao F, et al. Hierarchical porous MXene/amino carbon nanotubes-based molecular imprinting sensor for highly sensitive and selective sensing of fisetin. Sensor Actuat B Chem. 2020;309:127815.
197. Huang R, Liao D, Chen S, Yu J, Jiang X. A strategy for effective electrochemical detection of hydroquinone and catechol: Decoration of alkalization-intercalated $Ti_3C_2$ with MOF-derived N-doped porous carbon. Sensor Actuat B Chem. 2020;320:128386.
198. Tu X, Gao F, Ma X, et al. Mxene/carbon nanohorn/β-cyclodextrin-Metal-organic frameworks as high-performance electrochemical sensing platform for sensitive detection of carbendazim pesticide. J Hazard Mater. 2020;396:122776.
199. Zhang H, Wang Z, Wang F, Zhang Y, Wang H, Liu Y. $Ti_3C_2$ MXene mediated Prussian blue in situ hybridization and electrochemical signal amplification for the detection of exosomes. Talanta. 2021;224:121879.
200. Duan F, Guo C, Hu M, et al. Construction of the 0D/2D heterojunction of $Ti_3C_2T_x$ MXene nanosheets and iron phthalocyanine quantum dots for the impedimetric aptasensing of microRNA-155. Sensor Actuat B Chem. 2020;310:127844.
201. Seyedin S, Uzun S, Levitt A, et al. MXene Composite and Coaxial Fibers with High Stretchability and Conductivity for Wearable Strain Sensing Textiles. Adv Funct Mater. 2020;30(12):1910504.
202. Luo J, Gao S, Luo H, et al. Superhydrophobic and breathable smart MXene-based textile for multifunctional wearable sensing electronics. Chem Eng J. 2021;406:126898.
203. Zhao X, Wang L-Y, Tang C-Y, et al. Smart $Ti_3C_2T_x$ MXene Fabric with Fast Humidity Response and Joule Heating for Healthcare and Medical Therapy Applications. ACS Nano. 2020;14(7):8793–805.
204. Cao Z, Yang Y, Zheng Y, et al. Highly flexible and sensitive temperature sensors based on $Ti_3C_2T_x$ (MXene) for electronic skin. J Mater Chem A. 2019;7(44):25314–23.
205. Wang B, Lai X, Li H, Jiang C, Gao J, Zeng X. Multifunctional MXene/Chitosan-Coated Cotton Fabric for Intelligent Fire Protection. ACS Appl Mater Interfaces. 2021;13(19):23020–9.
206. Wang L, Tian M, Zhang Y, et al. Helical core-sheath elastic yarn-based dual strain/humidity sensors with MXene sensing layer. J Mater Sci. 2020;55(14):6187–94.
207. An H, Habib T, Shah S, et al. Water Sorption in MXene/Polyelectrolyte Multilayers for Ultrafast Humidity Sensing. ACS Appl Nano Mater. 2019;2(2):948–55.
208. Wu J, Lu P, Dai J, et al. High performance humidity sensing property of Ti3C2Tx MXene-derived Ti3C2Tx/K2Ti4O9 composites. Sensor Actuat B Chem. 2021;326:128969.
209. Li N, Jiang Y, Zhou C, et al. High-Performance Humidity Sensor Based on Urchin-Like Composite of $Ti_3C_2$ MXene-Derived TiO2 Nanowires. ACS Appl Mater Interfaces. 2019;11(41):38116–25.
210. Li H, Chen J, Chang X, et al. A highly stretchable strain sensor with both an ultralow detection limit and an ultrawide sensing range. J Mater Chem A. 2021;9(3):1795–802.
211. Schwartz G, Tee BCK, Mei J, et al. Flexible polymer transistors with high pressure sensitivity for application in electronic skin and health monitoring. Nat Commun. 2013;4(1):1859.
212. Wang H, Zhou R, Li D, et al. High-Performance Foam-Shaped Strain Sensor Based on Carbon Nanotubes and $Ti_3C_2T_x$ MXene for the Monitoring of Human Activities. ACS Nano. 2021;15(6):9690–700.
213. Wang X, Liu X, Schubert DW. Highly Sensitive Ultrathin Flexible Thermoplastic Polyurethane/Carbon Black Fibrous Film Strain Sensor with Adjustable Scaffold Networks. Nano-Micro Lett. 2021;13(1):64.
214. Bu Y, Shen T, Yang W, et al. Ultrasensitive strain sensor based on superhydrophobic microcracked conductive $Ti_3C_2T_x$ MXene/paper for human-motion monitoring and E-skin. Sci Bull. 2021;66(18):1849–57.
215. Yang Y, Shi L, Cao Z, Wang R, Sun J. Strain Sensors with a High Sensitivity and a Wide Sensing Range Based on a $Ti_3C_2T_x$ (MXene) Nanoparticle-Nanosheet Hybrid Network. Adv Funct Mater. 2019;29(14):1807882.

216. Zeng Y, Wu W. Synthesis of 2D $Ti_3C_2T_x$ MXene and MXene-based composites for flexible strain and pressure sensors. Nanoscale Horiz. 2021;6(11):893–906.
217. Zheng Y, Yin R, Zhao Y, et al. Conductive MXene/cotton fabric based pressure sensor with both high sensitivity and wide sensing range for human motion detection and E-skin. Chem Eng J. 2021;420:127720.
218. Yan J, Ma Y, Jia G, et al. Bionic MXene based hybrid film design for an ultrasensitive piezoresistive pressure sensor. Chem Eng J. 2022;431:133458.
219. Shi X, Fan X, Zhu Y, et al. Pushing detectability and sensitivity for subtle force to new limits with shrinkable nanochannel structured aerogel. Nat Commun. 2022;13(1):1119.
220. Zhang Y-Z, Lee Kang H, Anjum Dalaver H, et al. MXenes stretch hydrogel sensor performance to new limits. Sci Adv. 2018;4(6):eaat0098.
221. Wang S, Du X, Luo Y, et al. Hierarchical design of waterproof, highly sensitive, and wearable sensing electronics based on MXene-reinforced durable cotton fabrics. Chem Eng J. 2021;408:127363.
222. Ho DH, Choi YY, Jo SB, Myoung J-M, Cho JH. Sensing with MXenes: Progress and Prospects. Adv Mater. 2021;33(47):2005846.
223. Vijayababu M, Chintagumpala K. Review of MXene-based Resistance Pressure Sensors for Vital Signs Monitor. J Electron Mater. 2022;51(4):1443–72.
224. Wang Y, Yue Y, Cheng F, et al. Ti3C2Tx MXene-Based Flexible Piezoresistive Physical Sensors. ACS Nano. 2022;16(2):1734–58.
225. Wang Z, Zhou H, Liu D, et al. A Structural Gel Composite Enabled Robust Underwater Mechanosensing Strategy with High Sensitivity. Adv Funct Mater. 2022;32(25):2201396.
226. Su T, Liu N, Lei D, et al. Flexible MXene/Bacterial Cellulose Film Sound Detector Based on Piezoresistive Sensing Mechanism. ACS Nano. 2022;16(5):8461–71.
227. Gou G-Y, Li X-S, Jian J-M, et al. Two-stage amplification of an ultrasensitive MXene-based intelligent artificial eardrum. Sci Adv. 2022;8(13):eabn2156.
228. Xu B, Ye F, Chen R, Luo X, Chang G, Li R. A wide sensing range and high sensitivity flexible strain sensor based on carbon nanotubes and MXene. Ceram Int. 2022;48(7):10220–6.
229. Zhang Z, Weng L, Guo K, Guan L, Wang X, Wu Z. Durable and highly sensitive flexible sensors for wearable electronic devices with PDMS-MXene/TPU composite films. Ceram Int. 2022;48(4):4977–85.
230. Chen B, Zhang L, Li H, Lai X, Zeng X. Skin-inspired flexible and high-performance MXene@polydimethylsiloxane piezoresistive pressure sensor for human motion detection. J Colloid Interf Sci. 2022;617:478–88.
231. Lu W, Mustafa B, Wang Z, Lian F, Yu G. PDMS-Encapsulated MXene@Polyester Fabric Strain Sensor for Multifunctional Sensing Applications. Nanomaterials. 2022;12(5):871.
232. Wang S, Li D, Jiang L, Fang D. Flexible and mechanically strong MXene/FeCo@C decorated carbon cloth: A multifunctional electromagnetic interference shielding material. Compos Sci Technol. 2022;221:109337.
233. Fu X, Li J, Li D, et al. MXene/ZIF-67/PAN Nanofiber Film for Ultra-sensitive Pressure Sensors. ACS Appl Mater Interfaces. 2022;14(10):12367–74.
234. Cao Y, Guo Y, Chen Z, et al. Highly sensitive self-powered pressure and strain sensor based on crumpled MXene film for wireless human motion detection. Nano Energy. 2022;92:106689.
235. Luan H, Zhang D, Xu Z, Zhao W, Yang C, Chen X. MXene-based composite double-network multifunctional hydrogels as highly sensitive strain sensors. J Mater Chem C. 2022;10(19):7604–13.
236. Li H, Cao J, Chen J, Li Y, Liu J, Du Z. MXene-containing pressure sensor based on nanofiber film and spacer fabric with ultrahigh sensitivity and Joule heating effect. Text Res J. 2022;92(11–12):1999–2009.
237. Wang H, Xiang J, Wen X, et al. Multifunctional skin-inspired resilient MXene-embedded nanocomposite hydrogels for wireless wearable electronics. Compos Part A Appl S. 2022;155:106835.
238. Chen Q, Gao Q, Wang X, Schubert DW, Liu X. Flexible, conductive, and anisotropic thermoplastic polyurethane/polydopamine /MXene foam for piezoresistive sensors and motion monitoring. Compos Part A Appl S. 2022;155:106838.
239. Wu L, Xu C, Fan M, et al. Lotus root structure-inspired Ti3C2-MXene-Based flexible and wearable strain sensor with ultra-high sensitivity and wide sensing range. Compos Part A Appl S. 2022;152:106702.
240. Wang J, Dai T, Zhou Y, Mohamed A, Yuan G, Jia H. Adhesive and high-sensitivity modified $Ti_3C_2T_x$ (MXene)-based organohydrogels with wide work temperature range for wearable sensors. J Colloid Interf Sci. 2022;613:94–102.
241. Qin R, Li X, Hu M, Shan G, Seeram R, Yin M. Preparation of high-performance MXene/PVA-based flexible pressure sensors with adjustable sensitivity and sensing range. Sensor Actuat A Phys. 2022;338:113458.
242. Chen Y, Jiang Y, Feng W, Wang W, Yu D. Construction of sensitive strain sensing nanofibrous membrane with polydopamine-modified MXene/CNT dual conductive network. Colloid Surface A. 2022;635:128055.
243. Xu H, Jiang X, Yang K, et al. Conductive and eco-friendly gluten/MXene composite organohydrogels for flexible, adhesive, and low-temperature tolerant epidermal strain sensors. Colloid Surface A. 2022;636:128182.
244. Chen K, Hu Y, Wang F, et al. Ultra-stretchable, adhesive, and self-healing MXene/polyampholytes hydrogel as flexible and wearable epidermal sensors. Colloid Surface A. 2022;645:128897.
245. Qin M, Yuan W, Zhang X, et al. Preparation of PAA/PAM/MXene/TA hydrogel with antioxidant, healable ability as strain sensor. Colloid Surface B. 2022;214:112482.
246. Zhang D, Yin R, Zheng Y, et al. Multifunctional MXene/CNTs based flexible electronic textile with excellent strain sensing, electromagnetic interference shielding and Joule heating performances. Chem Eng J. 2022;438:135587.
247. Ganguly S, Das P, Saha A, Noked M, Gedanken A, Margel S. Mussel-Inspired Polynorepinephrine/MXene-Based Magnetic Nanohybrid for Electromagnetic Interference Shielding in X-Band and Strain-Sensing Performance. Langmuir. 2022;38(12):3936–50.
248. Adepu V, Kunchur A, Tathacharya M, Mattela V, Sahatiya P. SnS/$Ti_3C_2T_x$ (MXene) Nanohybrid-Based Wearable Electromechanical Sensors for Sign-to-Text Translation and Sitting Posture Analysis. ACS Appl Electron Mater. 2022;4(4):1756–68.
249. Yang G, Yang Y, Chen T, Wang J, Ma L, Yang S. Graphene/MXene Composite Aerogels Reinforced by Polyimide for Pressure Sensing. ACS Appl Nano Mater. 2022;5(1):1068–77.

250. Wen L, Nie M, Wang C, Zhao Y-N, Yin K, Sun L. Multifunctional, Light-Weight Wearable Sensor Based on 3D Porous Polyurethane Sponge Coated with MXene and Carbon Nanotubes Composites. Adv Mater Interfaces. 2022;9(5):2101592.
251. Adepu V, Kamath K, Siddhartha S, Mattela V, Sahatiya P. MXene/TMD Nanohybrid for the Development of Smart Electronic Textiles Based on Physical Electromechanical Sensors. Adv Mater Interfaces. 2022;9(4):2101687.
252. Zhao T, Liu H, Yuan L, et al. A Multi-Responsive MXene-Based Actuator with Integrated Sensing Function. Adv Mater Interfaces. 2022;9(10):2101948.
253. Bai Y, Qin F, Lu Y. Flexible and Lightweight Ni/MXene Decorated Polyurethane Sponge Composite with Sensitive Strain Sensing Performance for Ultrahigh Terahertz Absorption. Adv Opt Mater. 2022;10(4):2101868.
254. Mohseni Taromsari S, Shi HH, Saadatnia Z, Park CB, Naguib HE. Design and development of ultra-sensitive, dynamically stable, multi-modal GnP@MXene nanohybrid electrospun strain sensors. Chem Eng J. 2022;442:136138.
255. Wang Z, Zhang K, Liu Y, Zhao H, Gao C, Wu Y. Modified MXene-doped conductive organosilicon elastomer with high-stretchable, toughness, and self-healable for strain sensors. Compos Struct. 2022;282:115071.
256. Zeng Z, Yu S, Guo C, Lu D, Geng Z, Pei D. Mxene Reinforced Supramolecular Hydrogels with High Strength, Stretchability, and Reliable Conductivity for Sensitive Strain Sensors. Macromol Rapid Comm. 2022;43(15):2200103.
257. Zhang L, Zhang X, Zhang H, et al. Semi-embedded robust MXene/AgNW sensor with self-healing, high sensitivity and a wide range for motion detection. Chem Eng J. 2022;434:134751.
258. Lv Y, Min L, Niu F, et al. Wrinkle-structured MXene film assists flexible pressure sensors with superhigh sensitivity and ultrawide detection range. Nanocomposites. 2022;8(1):81–94.
259. Adepu V, Mattela V, Sahatiya P. A remarkably ultra-sensitive large area matrix of MXene based multifunctional physical sensors (pressure, strain, and temperature) for mimicking human skin. J Mater Chem B. 2021;9(22):4523–34.
260. Duan S, Lin Y, Wang Z, et al. Conductive porous MXene for bionic, wearable, and precise gesture motion sensors. Research. 2021;2021:9861467.
261. Sun J, Du H, Chen Z, Wang L, Shen G. MXene quantum dot within natural 3D watermelon peel matrix for biocompatible flexible sensing platform. Nano Res. 2022;15(4):3653–9.
262. Xu X, Chen Y, He P, et al. Wearable CNT/Ti3C2Tx MXene/PDMS composite strain sensor with enhanced stability for real-time human healthcare monitoring. Nano Res. 2021;14(8):2875–83.
263. Zheng X, Hu Q, Wang Z, Nie W, Wang P, Li C. Roll-to-roll layer-by-layer assembly bark-shaped carbon nanotube/Ti3C2Tx MXene textiles for wearable electronics. J Colloid Interf Sci. 2021;602:680–8.
264. Wang Q, Liu J, Tian G, Zhang D. Co@N-CNT/MXenes in situ grown on carbon nanotube film for multifunctional sensors and flexible supercapacitors. Nanoscale. 2021;13(34):14460–8.
265. Cai Y-W, Zhang X-N, Wang G-G, et al. A flexible ultra-sensitive triboelectric tactile sensor of wrinkled PDMS/MXene composite films for E-skin. Nano Energy. 2021;81:105663.
266. Fan Z, Zhang L, Tan Q, et al. Wearable pressure sensor based on MXene/single-wall carbon nanotube film with crumpled structure for broad-range measurements. Smart Mater Struct. 2021;30(3):035024.
267. Chen W, Liu L-X, Zhang H-B, Yu Z-Z. Kirigami-Inspired Highly Stretchable, Conductive, and Hierarchical $Ti_3C_2T_x$ MXene Films for Efficient Electromagnetic Interference Shielding and Pressure Sensing. ACS Nano. 2021;15(4):7668–81.
268. Wang Z-x, Han X-s, Zhou Z-j, et al. Lightweight and elastic wood-derived composites for pressure sensing and electromagnetic interference shielding. Compos Sci Technol. 2021;213:108931.
269. Yang Z, Li H, Zhang S, Lai X, Zeng X. Superhydrophobic MXene@carboxylated carbon nanotubes/carboxymethyl chitosan aerogel for piezoresistive pressure sensor. Chem Eng J. 2021;425:130462.
270. Lin C, Luo S, Meng F, et al. MXene/air-laid paper composite sensors for both tensile and torsional deformations detection. Compos Commun. 2021;25:100768.
271. Fan C, Wang D, Huang J, Ke H, Wei Q. A highly sensitive epidermal sensor based on triple-bonded hydrogels for strain/pressure sensing. Compos Commun. 2021;28:100951.
272. Zhang L, Zhang S, Wang C, Zhou Q, Zhang H, Pan G-B. Highly Sensitive Capacitive Flexible Pressure Sensor Based on a High-Permittivity MXene Nanocomposite and 3D Network Electrode for Wearable Electronics. ACS Sensors. 2021;6(7):2630–41.
273. Bandar Abadi M, Weissing R, Wilhelm M, et al. Nacre-Mimetic, Mechanically Flexible, and Electrically Conductive Silk Fibroin-MXene Composite Foams as Piezoresistive Pressure Sensors. ACS Appl Mater Interfaces. 2021;13(29):34996–5007.
274. Wang T, Wang J, Li Z, et al. PVA/SA/MXene dual-network conductive hydrogel for wearable sensor to monitor human motions. J Appl Polym Sci. 2022;139(7):51627.
275. Liu L, Wang L, Liu X, et al. High-Performance Wearable Strain Sensor Based on MXene@Cotton Fabric with Network Structure. Nanomaterials. 2021;11(4):889.
276. Yuan W, Qu X, Lu Y, et al. MXene-composited highly stretchable, sensitive and durable hydrogel for flexible strain sensors. Chinese Chem Lett. 2021;32(6):2021–6.
277. Jia Z, Li Z, Ma S, et al. Constructing conductive titanium carbide nanosheet (MXene) network on polyurethane/polyacrylonitrile fibre framework for flexible strain sensor. J Colloid Interf Sci. 2021;584:1–10.
278. Fu X, Li L, Chen S, et al. Knitted Ti3C2Tx MXene based fiber strain sensor for human–computer interaction. J Colloid Interf Sci. 2021;604:643–9.
279. Li X, Yang J, Yuan W, et al. Microstructured MXene/polyurethane fibrous membrane for highly sensitive strain sensing with ultra-wide and tunable sensing range. Compos Commun. 2021;23:100586.
280. Cheng W, Zhang Y, Tian W, et al. Highly Efficient MXene-Coated Flame Retardant Cotton Fabric for Electromagnetic Interference Shielding. Ind Eng Chem Res. 2020;59(31):14025–36.
281. Guo L, Zhang Z, Li M, et al. Extremely high thermal conductivity of carbon fiber/epoxy with synergistic effect of MXenes by freeze-drying. Compos Commun. 2020;19:134–41.
282. Liu X, Jin X, Li L, et al. Air-permeable, multifunctional, dual-energy-driven MXene-decorated polymeric textile-based wearable heaters with exceptional electrothermal and photothermal conversion performance. J Mater Chem A. 2020;8(25):12526–37.
283. Jia G, Zheng A, Wang X, et al. Flexible, biocompatible and highly conductive MXene-graphene oxide film for smart actuator and humidity sensor. Sensor Actuat B Chem. 2021;346:130507.

284. Xing H, Li X, Lu Y, et al. MXene/MWCNT electronic fabric with enhanced mechanical robustness on humidity sensing for real-time respiration monitoring. Sensor Actuat B Chem. 2022;361:131704.
285. Gao Y, Yan C, Huang H, et al. Microchannel-Confined MXene Based Flexible Piezoresistive Multifunctional Micro-Force Sensor. Adv Funct Mater. 2020;30(11):1909603.
286. Wang L, Zhang M, Yang B, Tan J. Lightweight, Robust, Conductive Composite Fibers Based on MXene@Aramid Nanofibers as Sensors for Smart Fabrics. ACS Appl Mater Interfaces. 2021;13(35):41933–45.
287. Chen Y, Deng Z, Ouyang R, et al. 3D printed stretchable smart fibers and textiles for self-powered e-skin. Nano Energy. 2021;84:105866.
288. Li K, Li Z, Xiong Z, et al. Thermal Camouflaging MXene Robotic Skin with Bio-Inspired Stimulus Sensation and Wireless Communication. Adv Funct Mater. 2022;32(23):2110534.
289. Clement RGE, Bugler KE, Oliver CW. Bionic prosthetic hands: A review of present technology and future aspirations. The Surgeon. 2011;9(6):336–40.
290. Jin G, Sun Y, Geng J, et al. Bioinspired soft caterpillar robot with ultra-stretchable bionic sensors based on functional liquid metal. Nano Energy. 2021;84:105896.
291. Sitti M. Miniature soft robots-road to the clinic. Nat Rev Mater. 2018;3(6):74–5.
292. Wang J, Gao D, Lee PS. Recent Progress in Artificial Muscles for Interactive Soft Robotics. Adv Mater. 2021;33(19):2003088.
293. Chen D, Liu Q, Han Z, et al. 4D Printing Strain Self-Sensing and Temperature Self-Sensing Integrated Sensor-Actuator with Bioinspired Gradient Gaps. Adv Sci. 2020;7(13):2000584.
294. Kim H, Lee H, Ha I, et al. Biomimetic Color Changing Anisotropic Soft Actuators with Integrated Metal Nanowire Percolation Network Transparent Heaters for Soft Robotics. Adv Funct Mater. 2018;28(32):1801847.
295. Liu Y-Q, Chen Z-D, Han D-D, et al. Bioinspired Soft Robots Based on the Moisture-Responsive Graphene Oxide. Adv Sci. 2021;8(10):2002464.
296. Wang Y, Huang X, Zhang X. Ultrarobust, tough and highly stretchable self-healing materials based on cartilage-inspired noncovalent assembly nanostructure. Nat Commun. 2021;12(1):1291.
297. Jing L, Li K, Yang H, Chen P-Y. Recent advances in integration of 2D materials with soft matter for multifunctional robotic materials. Mater Horiz. 2020;7(1):54–70.
298. Li Y, Yang H, Zhang T, et al. Stretchable Zn-Ion Hybrid Battery with Reconfigurable $V_2CT_x$ and $Ti_3C_2T_x$ MXene Electrodes as a Magnetically Actuated Soft Robot. Adv Energy Mater. 2021;11(45):2101862.
299. Tang Z-H, Zhu W-B, Mao Y-Q, et al. Multiresponsive $Ti_3C_2T_x$ MXene-Based Actuators Enabled by Dual-Mechanism Synergism for Soft Robotics. ACS Appl Mater Interfaces. 2022;14(18):21474–85.
300. Xiao X, Ma H, Zhang X. Flexible Photodriven Actuator Based on Gradient–Paraffin-Wax-Filled $Ti_3C_2T_x$ MXene Film for Bionic Robots. ACS Nano. 2021;15(8):12826–35.
301. Luo X-J, Li L, Zhang H-B, et al. Multifunctional $Ti_3C_2T_x$ MXene/Low-Density Polyethylene Soft Robots with Programmable Configuration for Amphibious Motions. ACS Appl Mater Interfaces. 2021;13(38):45833–42.
302. Duan S, Lin Y, Zhang C, et al. Machine-learned, waterproof MXene fiber-based glove platform for underwater interactivities. Nano Energy. 2022;91:106650.
303. Wang K, Jia Y, Yan X. A biomimetic afferent nervous system based on the flexible artificial synapse. Nano Energy. 2022;100:107486.
304. Persson I, Näslund L-Å, Halim J, et al. On the organization and thermal behavior of functional groups on Ti3C2 MXene surfaces in vacuum. 2D Mater. 2018;5(1):015002.
305. Xie Y, Naguib M, Mochalin VN, et al. Role of Surface Structure on Li-Ion Energy Storage Capacity of Two-Dimensional Transition-Metal Carbides. J Am Chem Soc. 2014;136(17):6385–94.
306. Tao K, Chen Z, Yu J, et al. Ultra-Sensitive, Deformable, and Transparent Triboelectric Tactile Sensor Based on Micro-Pyramid Patterned Ionic Hydrogel for Interactive Human-Machine Interfaces. Adv Sci. 2022;9(10):2104168.
307. Cui Y, Zhang Y, Cao Z, et al. A perspective on high-entropy two-dimensional materials. SusMat. 2022;2(1):65–75.
308. Ma W, Wang M, Yi Q, et al. A new $Ti_2V0_{.9}Cr_{0.1}C_2T_x$ MXene with ultrahigh gravimetric capacitance. Nano Energy. 2022;96:107129.
309. Pinto D, Anasori B, Avireddy H, et al. Synthesis and electrochemical properties of 2D molybdenum vanadium carbides-solid solution MXenes. J Mater Chem A. 2020;8(18):8957–68.


## Publisher's Note